Doctoral Thesis

Development of climate zones for passive cooling techniques and typical meteorological years based on quality control of datasets in Indonesia

I Dewa Gede Arya Putra

Student ID 2721550050

Graduate School of Science and Engineering

Kagoshima University

2024

List of Content

List of Pictures

List of Table

List of Equation

Nomenclature

CC	total cloud cover (oktas)
CCP	climatic cooling potential
CDD	cooling degree days
CDF	cumulative distribution function
DHI	diffuse horizontal irradiance (W/m^2)
DNI	direct normal irradiance (W/m^2)
FS	Finkelstein-Shaffer
GHI	global horizontal irradiance (W/m^2)
LT	long-term average
MAE	mean absolute error
MixR	mixing ratio
MSE	mean squared error
θz	solar zenith angle (◦)
PC	principal component
PCA	principal component analysis
Pr	precipitation (mm)
Pres	atmospheric pressure (mb)
RH	relative humidity (%)
RHb	indoor relative humidity (%)
RHWS	relative humidity and wind speed
RMSE	root mean squared error
T	air temperature (◦C)
Tb	indoor air temperature (◦C)
Td	dew point temperature (◦C)
TMM	typical meteorological month
TMY	typical meteorological year
TWS	air temperature and wind speed
WS	wind speed (m/s)
WSb	indoor wind speed (m/s)

Abstract

This study aims to develop climate zones and typical meteorological years (TMYs) in Indonesia. Hourly time series data from all sites of various climate elements such as solar radiation, temperature, relative humidity, wind speed, and others are considered for deeper analysis. In the first stage, the new climate zones developed in this study differed from those of the previous Koppen climate zoning and obtained more detailed and optimum results based on spatial and temporal distribution. This is because the integrated climate zoning in this study considered topographic data and more climate elements, including air temperature, wind speed, relative humidity, atmospheric pressure, total cloud cover, mixing ratio, global solar irradiance, and precipitation data. The availability of information on climate classification in this study was divided into eight new integrated climate zones, namely, climate zone 1A (equatorial), climate zone 1B (sub equatorial), climate zone 2A (highland tropical), climate zone 2B (very highland tropical), climate zone 3A (monsoon), climate zone 3B (sub monsoon), climate zone 4A (savanna), and climate zone 4B (sub savanna), in the territory of Indonesia. In the passive method, by taking the lower probability limit of 50 %, the monsoon, savanna, and sub savanna climate zones are suitable for the comfort ventilation method. Meanwhile, the sub equatorial climate zone is suitable for applying passive methods by combining night ventilation and comfort ventilation. In the second stage, we develop TMY at all sites in different climate zones throughout Indonesia. The Sandia method based on the modified FS statistical weighting for climate elements has been applied to develop the TMY 106 sites, which are in eight different climate zones in Indonesia. The results of the TMY selection show that the year selection for TMMs varies significantly in Indonesia, and the local climatic conditions have a major influence on the variation in the resulting TMY. Additionally, the resulting TMY accurately captures the long-term distribution pattern, particularly for global horizontal irradiance and temperature. The above result was found based on a high correlation value between TMY and LT, particularly an average of 0.96 for global horizontal irradiance and 0.86 for temperature. The resulting climate zones and TMY will be useful for various applications, such as thermal comfort assessment, renewable energy potential assessment, climate-responsive architectural design, and many more.

Keywords: climate zones, passive methods, typical meteorological years.

Chapter 1. Introduction

1.1 General research background

Indonesia is an archipelagic country that stretches from 6°N – 11°S and 95°E – 141°E, located between the continents of Asia and the Australian continent, as well as between the Indian Ocean and the Pacific Ocean with complex climatic characteristics due to global, regional and local phenomena [1]. Indonesia is also called the Indonesian maritime continent because this region consists of many islands surrounded by warm sea water which is considered to induce very intense convection activity playing a role as the main heat source that drives atmospheric circulation [2]. Atmospheric-ocean interactions around Indonesia form Interannual interactions of global climate variations such as the El Nino–Southern Oscillation (ENSO) [3] [4] and the Indian Ocean Dipole Mode (IOD)[5][6], Intra-seasonal variations such as the Intertropical Convergence Zone (ITCZ) [7][8][9], Madden–Julian Oscillation (MJO) [10][11][12][13][14] which affect climate conditions in Indonesia. As one of the unique tropical regions, its atmospheric dynamics are influenced by the presence of trade winds [3], monsoons [2][15][16][17][18][19] and the influence of various local conditions such as sea breezes [20] then the weather and climate in Indonesia have complex and dynamic physical characteristics [21].

To study the regional climatic conditions of an area, climate zoning is needed. Climate zoning, namely classifying regional climates according to one or a combination of several climate variables, is considered a rational method for understanding regional climate characteristics that are influenced by geographical and topographical conditions based on characteristics of almost similar climate values [22]. Climate zoning information is useful for various purposes, one of the most important purposes is to use it for the development of appropriate pre-design strategies for energy-efficient buildings and to determine certain energy-saving standards by implementing passive designs and thermal comfort objectives [23]. Cluster analysis applied to meteorological variables is a suitable approach for redefining climate divisions, and its use is becoming increasingly common in atmospheric research [24]. Netzel and Stepinski [25] used a clustering approach for global climate classification. Cluster analysis helps group variables into clusters based on high similarity of features, such as geographic, physical, statistical, or stochastic properties. Cluster analysis is a general approach in which clusters of variables are formed sequentially, where each cluster represents the smallest variance (or smallest inequality) of the

variables [22]. There have been many previous researchers using cluster analysis with the ward method in making climate zoning based on its stability [26][27][28][29][30][31][32] [33][34]. Several methods have been developed over the years to identify climate zones, the most common of which is to use principal component analysis to reduce data dimensions and continue with cluster analysis [35][36][37]. For example: Unal et al. [28] used cluster analysis and divided the turkey region into seven climate zones. Lam et al. [38] have undertaken the development of passive design zones for different climates in China for the potential use of passive design strategies such as solar heating, natural ventilation, thermal mass with or without night ventilation, and evaporative cooling assessed. Rakoto et al. [39] divided the island of Madagascar into six climate zones, which is extremely useful for building design for thermal comfort objectives. Arroyo et al. [40] used partitional and hierarchical clustering techniques and presented analyses of the main climatic zones in Spain. Wang et al. [41] conducted research on the impact of spatial clustering of urban land cover on soil surface temperatures across the Koppen climate zone in the contiguous United States. Praene et al. [42] conducted research on a GIS-based approach to identify climate zoning hierarchical groupings in principal component analysis. Hao et al. [43] established new climatic zones for major marine islands in China defined using a two-stage zoning method and clustering analysis. Shi and Wang [44] simulated climate zone changes in China based on high resolution regional climate projections under the RCP4.5 scenario.

Research on climate zoning in Indonesia was started in 2002 by Hamada et al. [45] based on observations from meteorological stations, Indonesia has been divided into 5 seasons depending upon whether the annual (C1) or semi-annual (C2) component has the larger amplitude, and also into types A and B depending upon whether the maximum rainfall of 'smoothed' pentad-mean rainfall amount appears during September–February or during March–August. Hendon [46] studied the characteristics of the dry season and rainy season and their interaction with sea surface temperatures around Indonesia. Aldrian and Dwi Susanto [47] divided Indonesia into three rainfall zones with an equatorial pattern around the equator with two peaks of rainfall seasons in a year, monsoonal patterns in parts of Sumatra, parts of Kalimantan, parts of Sulawesi, Java and the islands of Nusa Tenggara with one peak of the rainy season in a year and local patterns around the island of Maluku with the opposite pattern of the monsoonal pattern. Kuswanto et al. [48] divided Indonesia into three regions of rainfall patterns with monsoonal type, anti-monsoon type and semi-monsoonal type using TRMM data. According to the updated Koppen world climate zone map by

Beck et al. [49], there are 3 types of climate in Indonesia, namely (Af type) Tropical rainforest climate which stretches around the equator, (Am type) Monsoon climate which stretches over the islands of Java, South Sulawesi and South Papua, and (Aw type) Savanna climate that stretches across the islands of Nusa Tenggara. Several countries have published energy standards or policies for the design and construction of buildings according to climate zones to achieve energy conservation or reduction of carbon emissions from buildings. This study aims to obtain an accurate understanding of climate characteristics in the Indonesian region through the spatial distribution of climate zones, diurnal cycles, seasonal cycles and annual cycles, studies of the relationship between climate variables and studies of the phenomena that influence them. We will analyze detailed weather data and classify the country of Indonesia into several regions with similar climate patterns. this will provide specific benefits, namely, to increase understanding of climatic conditions in Indonesia and to provide suitable guidance for architects and engineers to implement energy-efficient building designs according to different climatic characteristics. This research also aims to develop a new climate zoning for the purpose of the first Indonesian national standard of climate regionalization for the application of passive cooling design techniques in Indonesia. This is also preliminary work to establish building regulations for Indonesia's future energy efficiency. In general, the results of this study can also be used for various other public sectors.

The energy consumption levels of Heating Ventilation and Air Conditioning Systems (HVAC) systems of residential and commercial buildings have increased over the last decade due to the growing demand for a better indoor thermal environment. This is related to the climatic conditions in a particular area that affect the energy consumption level of the building [50]. In the tropics, energy consumption for cooling particularly increases due to active air conditioning, which constitutes a major concern due to the relatively hot climatic conditions year-round [51]. The energy performance of a building is largely determined by how well the building design is adapted to the local climate. Therefore, it is very important for the developer and design team to gain a clear understanding of the local climate, including daily and seasonal variations, and the impact of the building design on the energy efficiency potential [52].

Koppen climate zoning maps are available for the whole world [25][49][53], and it has been used in various research areas including the building fields. However, the Koppen classification contains weaknesses, namely only based on vegetation patterns, air temperature, and rainfall.

Meanwhile, heating/cooling degree days/hours are commonly used in energy-saving standards for buildings as criteria in various countries because the HVAC is usually the main contributor of the building energy use as mentioned before. For the above purpose, most countries developed their own climate zoning maps simply based on the heating/cooling degree days/hours, which is basically attributed to the air temperature variations of the areas [54].

2.2 Purpose and contribution of research

In this thesis, we have divided it into seven chapters. Chapter 1 outlines the general background and research objectives. Chapter 2 describes one of the limited attempts to develop a comprehensive climate zone classification contributing to passive design. Through a case study of Indonesia, this thesis essentially examines the creation of new climate zones according to actual climatic conditions resulting in several regions with similar climate patterns based on a detailed analysis of long-term hourly weather data pertaining to major cities across Indonesia. Chapter 3 describes the assessment of passive cooling methods in each climate zone. Passive cooling techniques, namely, night ventilation, comfort ventilation, and evaporative cooling, were assessed in different climate zones using the climatic cooling potential (CCP) formula. The potential climate zoning map for several passive cooling techniques, is proposed to eventually establish building regulations for passive design buildings to ensure Indonesia's future energy efficiency. Chapter 4 describes the study of vertical solar irradiance in Tangerang and Jembrana-Bali, Indonesia. This study uses historical solar radiation data from global horizontal irradiance and solar radiation from the vertical component including north vertical surface irradiance, south vertical surface irradiance, west vertical surface irradiance, and east vertical surface irradiance. Each component of horizontal and vertical solar radiation is analyzed sub-diurnal and seasonally.

TMY studies require complete hourly time series data with long-term periods. If there is missing data, proper data treatment, such as interpolation, is needed. Chapter 5 describes the quality control of datasets for TMY calculation input. The reanalysis data has been corrected for bias to cover missing data. The gap-filling technique for the temperature parameter and the other parameters is based on ERA5 data. Quantile mapping can improve the distribution of ERA5 temperature values to be close to the distribution of observed values. The same procedure was employed to fill in the missing observational data on relative humidity and wind speed at 106 sites

in Indonesia. Indonesia has not yet created national standard TMY datasets. Chapter 6 describes the development of TMY and its verification. TMY can reduce the complicated computational effort in simulating and handling weather data using a one-year dataset. The calculation of TMY in this study used the Sandia method with modifications in the weighted factor for each climate element. The Sandia method, an empirical approach, involves selecting specific months of the year that differ from the recorded period. the resulting TMY with 12 TMMs at 106 sites. The generated TMY will be highly beneficial for various of applications, such as energy-efficient building designs, assessment of renewable energy potentials, and climate-responsive architectural designs, in the future. In Chapter 7, the results of this study are summarized.

Chapter 2. Development of climate zones in hot and humid climate of Indonesia

2.1 Introduction

Passive design strategies are considered to be one of the energy efficiency measures for buildings. While reducing the energy demand of buildings, it can reduce the dependence on fossil energy and utilize renewable energy [55]. Passive cooling techniques, in particular, provide the potential to maintain indoor temperatures within the comfortable range while reducing building cooling loads [56]. Passive cooling techniques have been studied in various climate zones. For example, a numerical study of a residential house in the city of Kerman showed that four passive techniques, namely green roof, roof pond, wind catcher and underground house, positively affect the reduction and compensation of energy loss through convection, conduction, and air penetration in semi-arid regions of Iran [57]. Fernandes et al. [58] have investigated the passive strategy of vernacular buildings, one of which is the use of high thermal inertia, namely rammed-earth walls and vaulted ceilings, in hot and dry summer climate zones. Dharmasastha et al. [59] have studied an energy-efficient thermally activated building system integrated with glass fiber reinforced gypsum located in a tropical wet and dry climate zone. Diaz-López et al. [60] identified and compared passive cooling strategies used for the Mediterranean climates, the most commonly used passive cooling strategies in hot dry summer (Csa) and cool dry summer (Csb) climate zones are natural ventilation, green roofs, low thermal transmittance windows, and solar shading. Widera [61] has investigated the basis for a sustainable, bioclimatic, and affordable housing model for western sub-Saharan Africa and determined the optimal ventilation rates. Osman and Sevinc [62] have investigated the use of indirect and direct cooling techniques to cool the air, which has been suitable for all seasons in the hot arid desert zone region of Khartoum Sudan.

The definition of adequate climatic zones is complex task due to the interaction of several independent variables [54]. At the moment, there is no scientific method widely accepted for developing the climatic zone although several methods have been developed over the last few decades. According to Walsh et al. (2017)[54], around 80% of the previous relevant studies used only up to three techniques or parameters to define their climate zoning. Among several methods, the most commonly used method includes a principal component analysis to reduce data [36][37], followed by a hierarchical cluster analysis [22][33]. Then, a spatial interpolation is often followed

[26][42]. The cluster analysis makes possible the use of large range of climatic and geographical variables which may influence building thermal conditions as well as energy performance [54]. However, hierarchical cluster analysis has weaknesses, namely the chaining problem and its difficulty of determining the optimal number of clusters. In [24], after careful consideration, the Ward method was chosen to redefine the climate zones in Turkey with more homogeneous seasonal characteristics. Similarly, several previous studies applied cluster analysis using the Ward method based on the homogeneity of climate elements due to its stability [30] [32]. The development of climate zones in research will contribute to identifying different climate conditions on a macro scale in Indonesia.

2.2 Methodology

2.2.1 Climate data

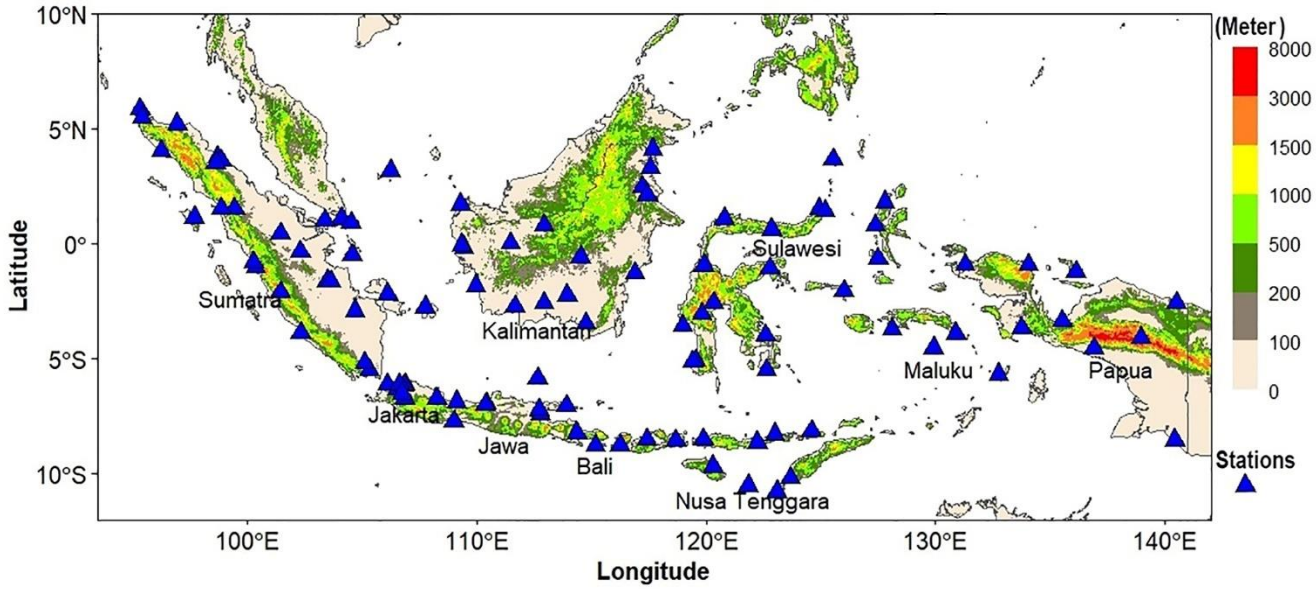

Figure 1. The locations of the 106 sites considered with elevation

This study considers hourly historical data of eight outdoor climate factors, including air temperature (T), wind speed (WS), relative humidity (RH), atmospheric pressure (Pres), total cloud cover (CC), and mixing ratio (MixR), acquired from the meteorological stations of the Indonesian Agency for Meteorology, Climatology and Geophysics (BMKG) from January 2014 to December 2020. Global horizontal irradiance (GHI) and precipitation (Pr) data were extracted from the ERA5 reanalysis data [63] to the coordinates of all the station locations[64]. The ETOPO1 model (1 arc-minute global relief model) of the National Oceanic and Atmospheric Administration

(NOAA) National Geophysical Data Center was retrieved and utilized as earth surface elevation data (Figure 1). The selection of these factors ensured that groups with similar climatic conditions could be identified considering their spatial and temporal (diurnal and seasonal) variations in local climatic conditions and elevation. Then, the collected climate data were subjected to a data quality check by investigating the available period, the percentage of missing data, and the historical trend. In this quality control process, stations with more than 30 % missing values were not included in further analysis. After a data quality check, 106 stations were found to be suitable for further in-depth analysis. The observation time, which was originally in universal time coordinated (UTC) format, was converted into a local time (LT) format according to the three Indonesian time zones namely, western Indonesian time, central Indonesian time, and eastern Indonesian time.

2.2.2 Analysis process

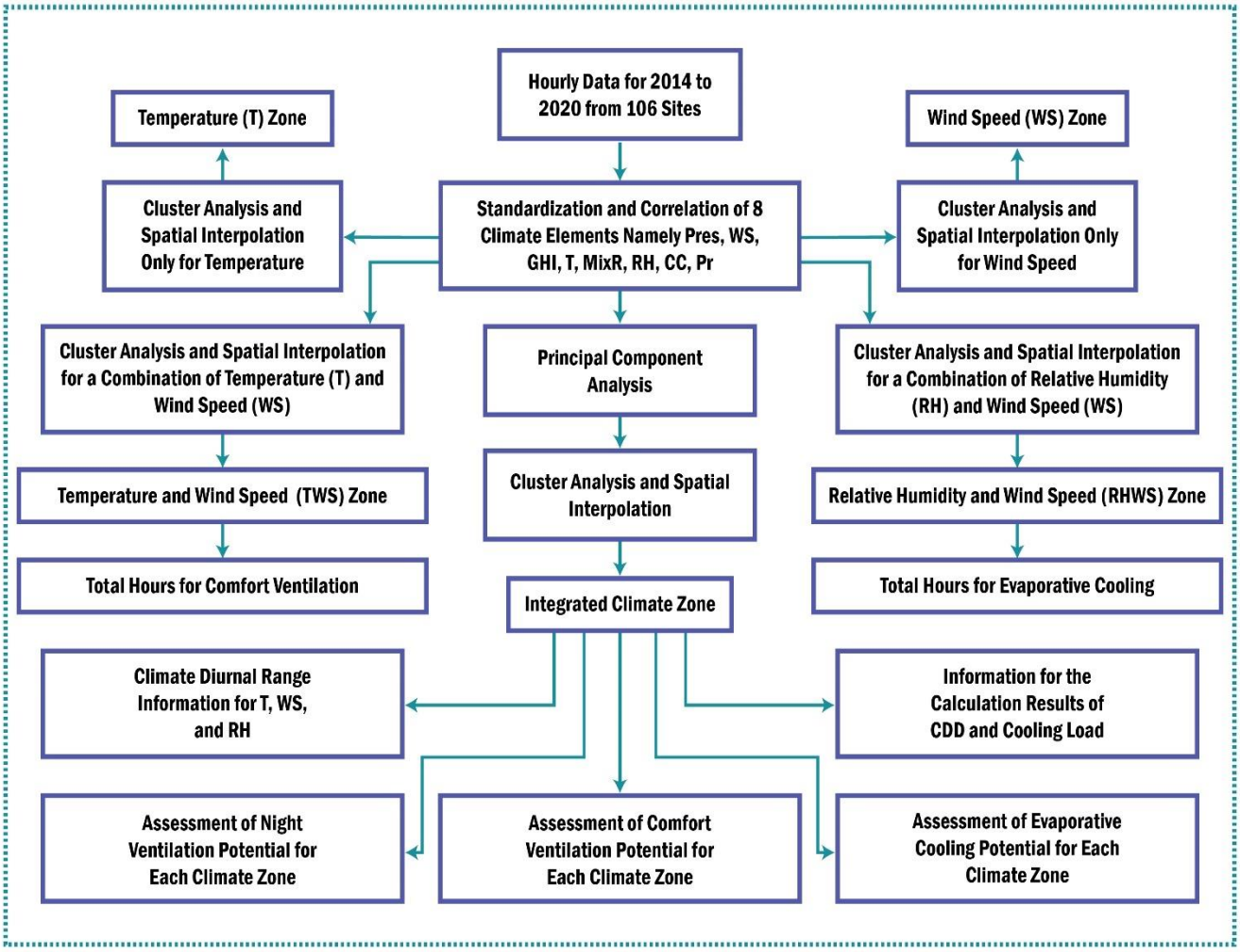

Figure 2. Data processing flow

Figure 2 illustrates the flow of data processing in this study. As shown, the acquired hourly data on all climate factors were standardized and correlated to determine the relationships among all the climate factors. The heatmap analysis containing diurnal and seasonal information (24 hours x 12 months) was conducted based on the hourly and monthly average values to visualize temporal variations of air temperature factor in temperature zones and windspeed factor in windspeed zones. Then, a cluster analysis for the combination of air temperature and wind speed was carried out to assess the potential for comfort ventilation. In this assessment, i.e., comfort ventilation, indoor temperatures above 29ºC are considered uncomfortable [65] and the total potential hours for comfort ventilation were determined based on a combination of air temperatures below 29ºC and wind speeds exceeding 1.8 m/s. Moreover, a cluster analysis for the combination of relative humidity and wind speed was carried out to assess the potential for evaporative cooling. The evaluation of evaporative cooling potential was based on the Givoni's bioclimatic charts that consider relative humidity [66]. In this study, the evaporative cooling potential was determined based on a combination of relative humidity below 70% and wind speed above 1.8 m/s. The threshold for relative humidity is also in accordance with the research of Manzano-Agugliaro et al. [67] where thermal comfort was achieved when the relative humidity was between 20% and 70%. As shown in Figure 2, a principal component analysis was carried out to reduce the data dimensions that consists of various combinations of the above-mentioned eight climate factors. The results of cluster analysis were spatially mapped through the spatial interpolation method using modified inverse distance weights [42] by overlaying topographic data. While constructing the integrated climate zones, we also calculated the cooling degree days per year and the cooling load from the total number of observation data per hour. Then, we assessed the potentials of passive cooling techniques in percentages, namely night ventilation, comfort ventilation, and evaporative cooling, in each integrated climate zone.

2.2.3 Principal component analysis

Principal component analysis (PCA) can be used to identify dominant features and a small set of factors, that account for a large proportion of the total variance in the original factors [36,48,49]. PCA is practical for extracting important factors, measuring their frequencies, reproducing circulation types, and determining periods of dominant climate factors [68]. The input data applied in PCA was the hourly average time series of the eight climate factors obtained from

106 sites, which resulted in the information on the combination of diurnal and seasonal cycles. Then, the eight climate factors were standardized to a mean value of 0 and a standard deviation of 1 to confirm that all factors attained the same weight in PCA. The principal components (PCs) can be calculated using Equation 1.

$$PC_i = W_1X_1 + W_2X_2 + \cdots + W_nX_n \quad \text{(Eq. 1)}$$

where X_n and W_n are the original factor and the weight component, respectively. The weight of the PC can be defined as a measure of the correlation between the factors and the PC. The largest or the first PC is oriented along the direction of the highest variation in the original factor and passes through the data center. The second-largest PC occurs along the direction of the next highest variation, passing through the data center and orthogonal to the first PC. The third-largest PC is oriented along the direction of the next highest variation, passes through the data center and is orthogonal to the first and second PCs. Classical PCA is based on covariance matrix decomposition or correlation involving eigenvalue decomposition or singular value decomposition of real data matrices. Eigenvalues or singular values indicate the variation among the observed factors [69].

2.2.4 Cluster analysis

Cluster analysis is an effective statistical method to classify a set of measured factors into several different groups. This technique can be used to obtain homogeneous climate zones based on the observed climate factors. In this study, Ward's algorithm was performed in terms of the retained component of the previous PCA score [31]. This technique obtains clusters by selecting areas with the lowest possible internal variance. Hierarchical agglomeration clustering relies on the Ward method, which combines cluster pairs with the smallest intercluster Euclidean distance. The Euclidean distance can be calculated using Equation 2. The number of initial clusters in this method is obtained from a dendrogram, a graphical tree diagram in which each object is arranged on one axis, and the other axis describes the steps in the hierarchical procedure. At the initial stage, each object is described as a separate cluster. The dendrogram graphically shows how the clusters are joined at each step of the procedure until all objects are contained in one cluster. The measure employed in the Ward method is the sum square error [34] of each observation in regard to the average of the cluster in which the observation is located. Cluster analysis classifies a set of objects into groups or clusters based on a specific similarity measure [53].

$$d_{ij} = \frac{N}{M}\sum_{k=1}^{M}\left(x_{ik} - x_{jk}\right)^2 \quad \text{(Eq. 2)}$$

where d_{ij} is the Euclidean distance between x_i and x_j over the M available data points. N is the number of data points in the full data period [28]. The clustering Ward algorithm will classify the 106 sites into several climate zones based on the homogeneity of climate characteristics. The zoning results of all the climate factors will be mapped spatially. The spatial mapping was performed using the inverse distance-weighted method [42], which is modified and overlaid with topography data for all the cluster analysis outputs to determine detailed climate characteristics over Indonesia.

2.3 Result and discussion

2.3.1 Relationship between the climate factors

Based on the above correlation matrix (Figure 3) of the factors, the wind speed, global horizontal irradiance, temperature, and mixing ratio exhibited a mutually positive relationship, with a correlation value above 0.65. This indicates that the temperature, mixing ratio, and wind speed increase with the rising intensity of global horizontal irradiance. The rising intensity of global horizontal irradiance increases the air temperature during the day. When the air temperature on land increases, this generates air circulation that is, followed by wind speed intensification. The relative humidity attained the best relationship with wind speed, global horizontal irradiance, air temperature, and mixing ratio. This relationship was indicated by a negative correlation of 0.8, implying that relative humidity decreases as global horizontal irradiance increases. These findings contradict to the research of Sadiq [70], where there was a positive correlation between relative humidity and air temperature. The air pressure, total cloud cover, and precipitation had the lowest correlation values with the other factors. The correlation between the air pressure and temperature was positive at 0.41 because the tropics have low diurnal variations in the air pressure and the air temperature. The correlation between cloud cover and precipitation reached 0.37. A high total cloud cover usually relates to enhanced rain potential. However, the observation of total cloud cover included the coverage of low, medium, and high clouds type. Rain is more likely to occur from low clouds type, such as shallow convective and stratiform clouds. This explains the relatively low correlation value between total cloud cover and precipitation. A high total cloud

cover generally results in a decline in global horizontal irradiance intensity. This condition was indicated by a negative correlation value, even though the correlation value was very small. The other climate factors attained low correlations, namely, precipitation with atmospheric pressure, cloud cover with air temperature, global horizontal irradiance with atmospheric pressure, and relative humidity with atmospheric pressure, at values below 0.1. These correlations were reflected by irregular distributions in the scatter plots.

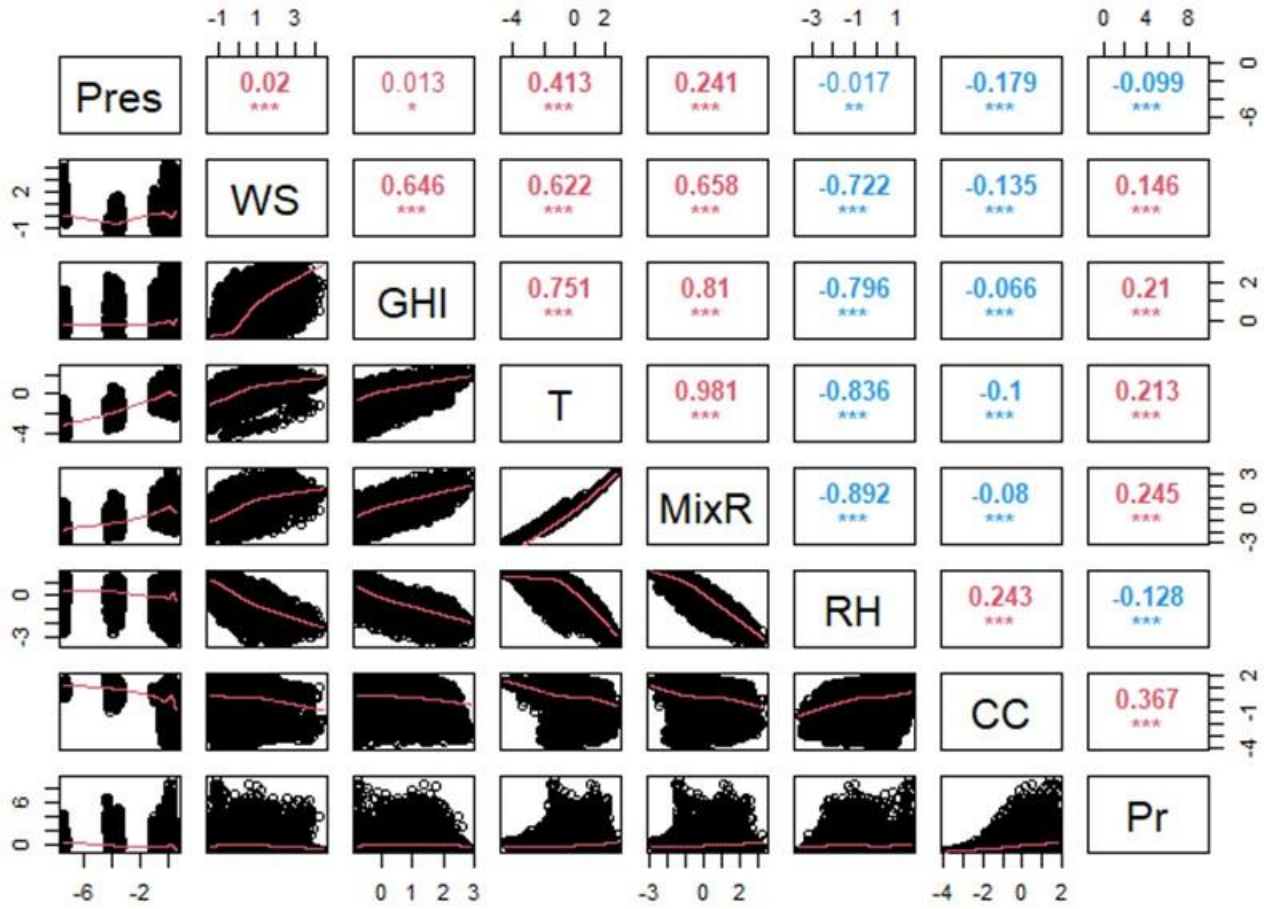

Figure 3. Scatter plot of the correlation matrix of the climate factors

2.3.2 PCA Analysis

PCA results show that grouping observation plots based on eight climate elements is sufficient to use four main PCs, namely PC1 to PC4. The eigenvalues indicate that there are four main components that are statistically significant because only the first four PCs have eigenvalues with criteria greater than one [71] which account for about 91% of the total variance in the data. Other main factors are not used in the classification because they have a fairly low ability to explain the total variation or lower than the average contribution of each variable to the total variance [72].

Four variables have a significant effect on the new variable. The four variables can be formulated in terms of three main factors which have a close correlation with the variables analyzed and can be considered to reflect phenomena related to climate characteristics in Indonesia. The results of PC1 represent about 53% of the data diversity with the main characteristic variables, namely mixing ratio (factor loadings value of 0.47), temperature (factor loadings value of 0.46), and relative humidity with factor loadings value of -0.45 (See table 1. factor loading). However, the relative humidity variable has a negative correlation, where increasing the temperature on the other hand can decrease the relative humidity. As previously explained, several factors can affect temperature, namely the intensity of solar radiation. duration. The higher the radiation intensity, the higher the temperature. PC2 represents about 18% of the data diversity. The characterizing variables are cloud cover with a factor loadings value of -0.65 and precipitation with a factor loadings value of -0.62. This shows a unidirectional relationship, namely when low cloud cover results in less rainfall. PC3 represents about 13% of the data diversity. The characteristic variable is air pressure with a factor loading value of -0.80. PC4 represents about 7% of the data diversity. The characterizing variable is precipitation with a factor loading value of 0.72.

Table 1. Rotated PC Loadings and Communalities (varimax rotation).

Climate Variables	**PC1**	**PC2**	**PC3**	**PC4**	**PC5**	**PC6**	**PC7**	**PC8**
Cloud Cover	-0.08	-0.65	-0.29	-0.67	0.10	-0.06	0.15	0.00
Temperature	0.46	0.05	-0.25	-0.08	-0.15	-0.24	-0.36	0.71
Wind Speed	0.38	-0.02	0.24	-0.02	0.89	0.03	-0.09	-0.01
Relative Humidity	-0.45	-0.04	-0.22	0.01	0.16	0.35	-0.77	-0.01
Pressure	0.10	0.41	-0.80	0.01	0.21	0.19	0.28	-0.13
Solar Radiation	0.43	-0.10	0.15	-0.13	-0.25	0.84	0.04	0.03
Precipitation	0.12	-0.62	-0.26	0.72	0.03	0.03	0.06	0.00
Mixing Ratio	0.47	-0.02	-0.11	-0.08	-0.22	-0.26	-0.40	-0.69

2.3.3 Analysis of the temperature and wind speed

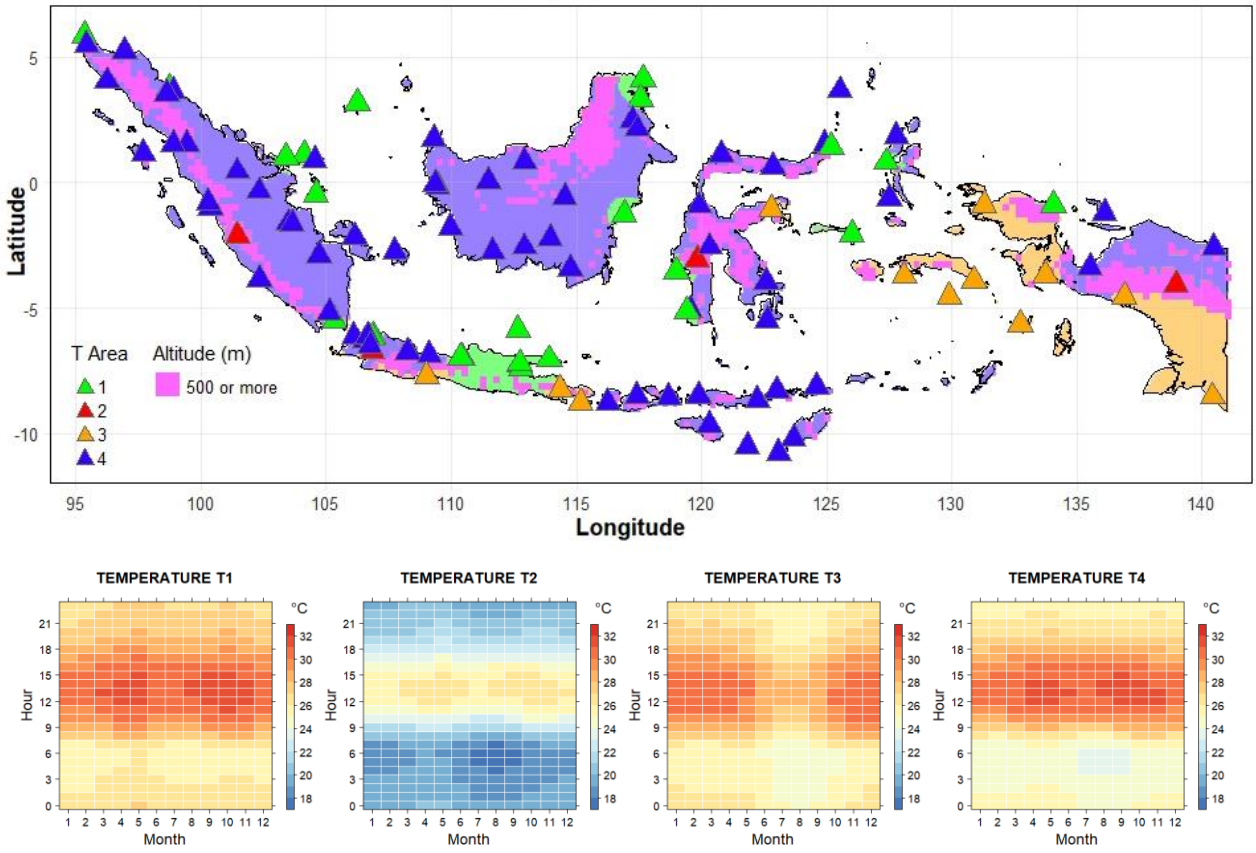

Figure 4. Temperature (T) zones in Indonesia

The clustering algorithm applied to only the temperature factor resulted in four temperature zones, and it was observed that the temperature in the territory of Indonesia varied slightly in regard to the seasonal and diurnal cycles in the T1, T2, T3, and T4 zones (Figure 4). This is primarily because Indonesia is an archipelagic country geographically surrounded by oceans and located in the tropics, where the diurnal temperature changes are negligible due to the thermal moderation throughout the day by large water mass of the ocean [73]. Heatmaps show that Indonesia experiences high-temperature conditions throughout the year with diurnal and seasonal cycles. The temperature is normally ranges from 23.3 °C to 31.6 °C in flat areas with a low topography (refer to Table 2), except for the T2 zone that is located in highlands regions. The T2 zone includes the Kerinci area of Jambi Province, Citeko of West Java Province, Tana Toraja of South Sulawesi Province, and Wamena of Papua Province, which exhibit relatively low temperatures [74].

The daily and seasonal temperature variabilities follow the apparent motion of the sun,

affecting the intensity of global horizontal irradiance. The temperature reaches its maximum seasonal temperature peak from March to April and from September to October under equinox conditions (the sun is located above the equator) [75]. The regional factor, southeast monsoon steaming air masses from Australia to Indonesia impacts the temperature variability in the T4 zone which includes almost all regions of Indonesia including Sumatra, Kalimantan, Sulawesi, the islands of Nusa Tenggara, and North Papua[75]. The temperature decreases in the early evening hours from June to September (JJAS) in these regions. The T3 zone is located in southern Java and southern Papua, with the seasonal temperature cycle decreasing during the day and night in JJAS. This pattern is influenced by the southeast monsoon and the sea surface temperature that decrease during JJAS near southern Java and the Arafura Sea [63,64]. Meanwhile, the temperature remains relatively high throughout the year and does not reveal a clear seasonal cycle in the T1 zone, which covers the East Java to Bawean Island, the Riau Islands, the west coast of South Sulawesi, east coast of East Kalimantan and the North Maluku Islands. This attributes to the low topography and local scale effects of ocean conditions.

Table 2. Average diurnal and seasonal temperature ranges for each T zone

T	**Temperature**			
zone	**minimum**	**maximum**	**median**	**mean**
1	23.3°C	31.6°C	27.7°C	28.1°C
2	17.6°C	27.0°C	20.8°C	21.6°C
3	24.2°C	30.9°C	26.8°C	27.2°C
4	23.5°C	31.5°C	26.6°C	27.2°C

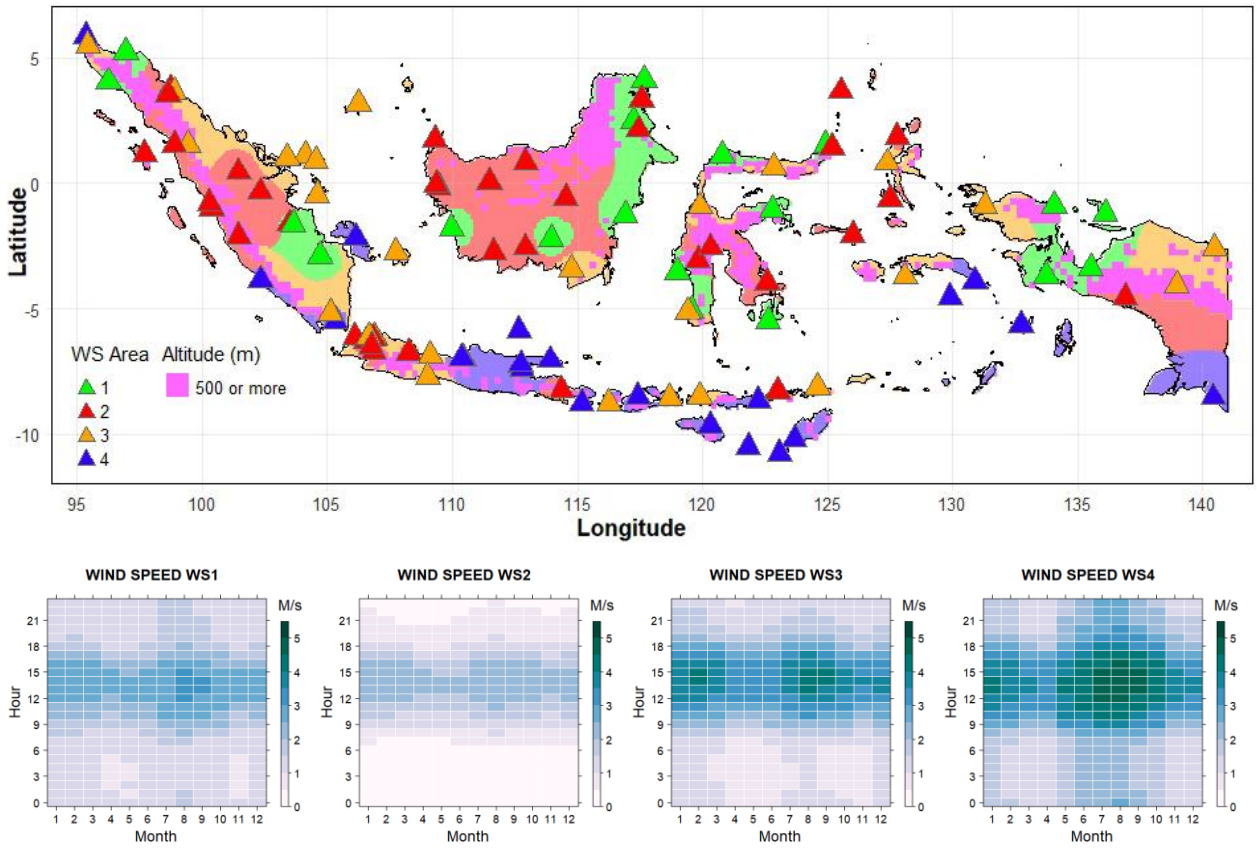

Figure 5. Wind speed (WS) zones in Indonesia

Based on the clustering algorithm applied to only the wind speed factor, in general, the wind speed pattern in Indonesia was revealed to have a clear diurnal cycle in the four WS zones. As an archipelagic country, microscale land-sea breezes and valley breezes affect the wind diurnal cycle in almost all Indonesian areas. Figure 5 illustrates that wind speed generally increases during the day and decreases at night. This pattern reflects the influence of strong local land-sea circulation. Regarding the seasonal cycle of wind speed, the wind speed in Indonesia is dominated by regional circulation forced by the apparent movement of the sun. During June to September (JJAS) season, the sun moves toward the Northern Hemisphere forming centers of low atmospheric pressure areas in the north and high atmospheric pressure areas in the south of Indonesia. This condition generates a relatively strong southerly winds over Indonesia. During December to February (DJF) season, the sun migrates toward the Southern Hemisphere, generating a relatively weaker northerly wind [76].

The wind speed exhibited diurnal, seasonal, annual, and interannual cycles that relate to global climate indices such as the southern oscillation index and Indian Ocean Dipole. These

climate indices affect wind variability in different areas of the world [76]. Based on Figure 5, the WS4 zone covers the area of Nusa Tenggara, East Java, South Sumatra, and South Papua. The WS3 zone covers the part of Nusa Tenggara, the part of Java, Sulawesi, and North Papua. The WS4 and WS3 zones experience relatively strong winds during the day in JJAS and DJF seasons. The WS1 zone covering South Sumatra, Aceh, southern Kalimantan, Sulawesi, and North Papua, oppositely experience relatively weak winds. The influence of wind originating from the north and south weakens because the WS1 zone is mostly located near the equator [21]. The WS2 zone covers the central part of Sumatra, Kalimantan, West Java, Central Sulawesi, and North Maluku, and is the area with the lowest wind speed values due to its location being mostly located on islands close to the equator. The land use dominated by dense forestlands may reduce the surface wind speed in those areas. The average daily and seasonal wind speed ranges for each region are provided in Table 3.

Table 3. Average diurnal and seasonal wind speed ranges for each WS zone

WS	**Wind speed**			
zone	**maximum**	**minimum**	**median**	**mean**
1	3.2 m/s	0.9 m/s	1.4 m/s	1.7 m/s
2	2.4 m/s	0.2 m/s	0.7 m/s	1.0 m/s
3	4.2 m/s	0.7 m/s	1.6 m/s	2.0 m/s
4	4.8 m/s	1.1 m/s	2.3 m/s	2.5 m/s

2.3.4 Integrated climate zones

Indonesia is an archipelagic country located along the equator that exhibits a varied topography and different land uses. Various complex climatic phenomena at global, regional, and local scales ranging from surface and upper air circulations to atmospheric interactions with the ocean have shaped the distinct climate characteristics of each region. In this study, eight integrated climate zones are defined according to the possible implementation of passive design strategies in Indonesia. Figure 6 shows the eight integrated climate zones classified by considering the outputs of PCA, cluster analysis, and spatial interpolation and by using a combination of eight climate factors. Based on the formed zones, three geographical factors (longitude, latitude, and altitude) affect the spatial and temporal characteristics of climate zones [53,54]. This study found that

Indonesia's territory can be divided into eight integrated climate zones, namely, equatorial, sub-equatorial, highland tropical, very highland tropical, monsoonal, sub-monsoonal, savanna and sub-savanna climate zones. This zonation is more detailed and optimal than Köppen's climate classification [49], which divides Indonesia into only three climate zones, namely the equatorial climate (Af), the monsoon climate (Am), and the tropical savanna climate (Aw).

The integrated climate zone 1A (equatorial) is distributed on large islands, including Sumatra, Kalimantan, Sulawesi, and Papua which are mostly located near the equator. Zone 1A is a warm region with a high cloud cover and high rainfall conditions throughout the year. The diurnal and seasonal air temperatures in zone 1A range from 22.6 to 33.1 °C, with wind speed values ranging from 0.0 to 4.8 m/s. Integrated climate zone 1B (sub-equatorial) is distributed on small islands located near the equator, covering the islands of North Maluku to South Maluku, the Bangka Belitung Islands, and the Riau Islands. The difference between zone 1B and zone 1A is that zone 1B is affected by monsoon impacting the seasonal cycle of the air temperature and wind speed with a small magnitude. The diurnal and seasonal air temperatures in zone 1B range from 22.6 to 32.9 °C, with wind speed values in the range of 0.1 - 6.7 m/s.

The integrated climate zone 2A (highland tropical) is located at an altitude above 700 meters in the Kerinci region of Jambi Province, Citeko, West Java Province, and Tana Toraja, South Sulawesi Province. Thus, this zone experiences a highland climate characterized by low air temperatures, humid conditions, and high rainfall levels due to orographic effects. The diurnal and seasonal air temperatures in zone 2A range from 17.8 to 29.0 °C, with wind speed values ranging from 0.0 to 3.6 m/s. Zone 2B (very highland tropical) is found at Wamena on Papua Island at an altitude of 1660 m, which makes this area the coldest, moistest, windiest, and wettest area with high rainfall levels. The diurnal and seasonal air temperatures in zone 2B range from 15.1 to 25.7 °C, with wind speed values ranging from 0.8 to 6.8 m/s.

Zones 3A (monsoonal) and 3B (sub-monsoonal) occur in most of Java, South Kalimantan, South Sulawesi, and North Sulawesi. These two zones exhibit a clear seasonal cycle of each climate factor, the rainy season with high cloud cover and high relative humidity levels during the DJF period and a dry season with low cloud cover and low relative humidity levels during JJAS. The diurnal and seasonal temperatures in zone 3A range from 21.7 to 33.7 °C, with wind speeds ranging from 0.1 to 6.3 m/s. Zone 3B differs from zone 3A and exhibits weaker wind and lower seasonal air temperatures. The diurnal and seasonal air temperatures in zone 3B range from 22.2

to 34.5 °C, with wind speed ranging from 0.0 to 4.1 m/s.

Zone 4A (savanna) occurs across the Nusa Tenggara archipelago, which is an area with a long dry season, strong winds, and high global horizontal irradiance intensity during the JJAS period. Zone 4A is predominantly influenced by the southeast monsoon. The air temperature in this area decreases at night during JJAS. The diurnal and seasonal air temperatures in zone 4A range from 21.2 to 34.3 °C, with wind speed values ranging from 0.0 to 7 m/s. Zone 4B (sub-savanna) is found on the island of Madura. Zone 4B has a smaller range of air temperature variability between the seasonal and daily cycles than that found in zone 4A. The diurnal and seasonal temperatures in zone 4B range from 24.4 to 34.4 °C, with wind speed ranging from 0.0 to 5.8 m/s. Figure 7 shows the detailed variations for each climate factor in each integrated climate zone.

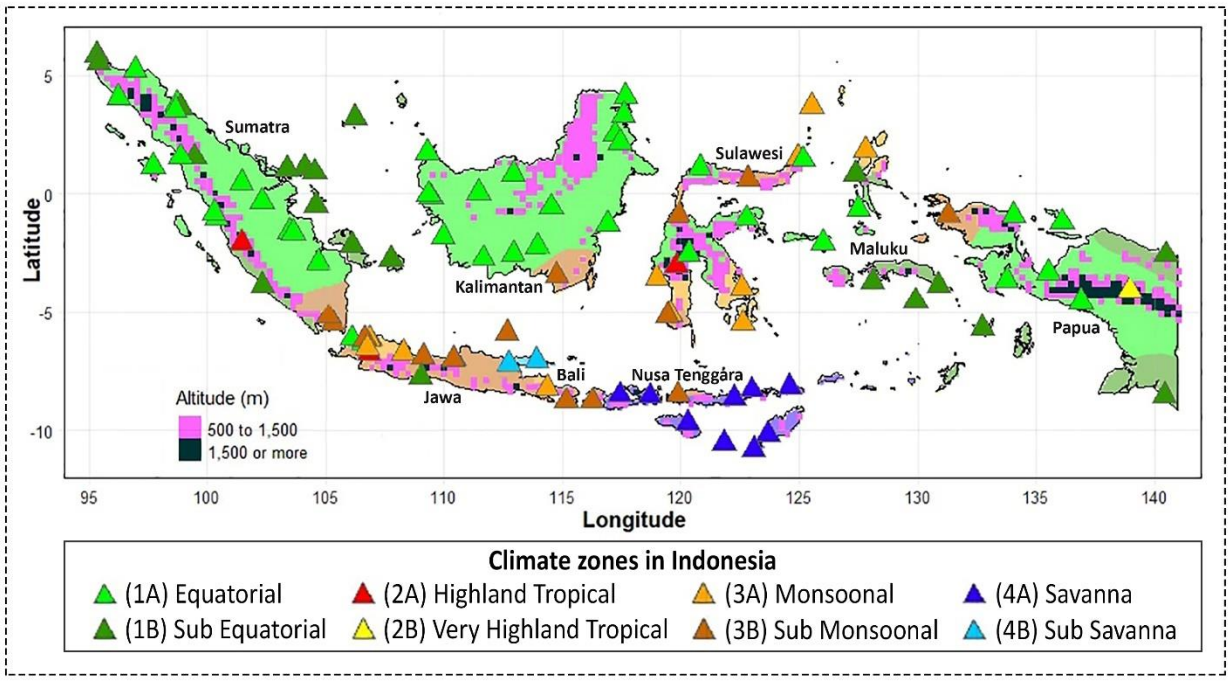

Figure 6. Integrated climate zones in Indonesia

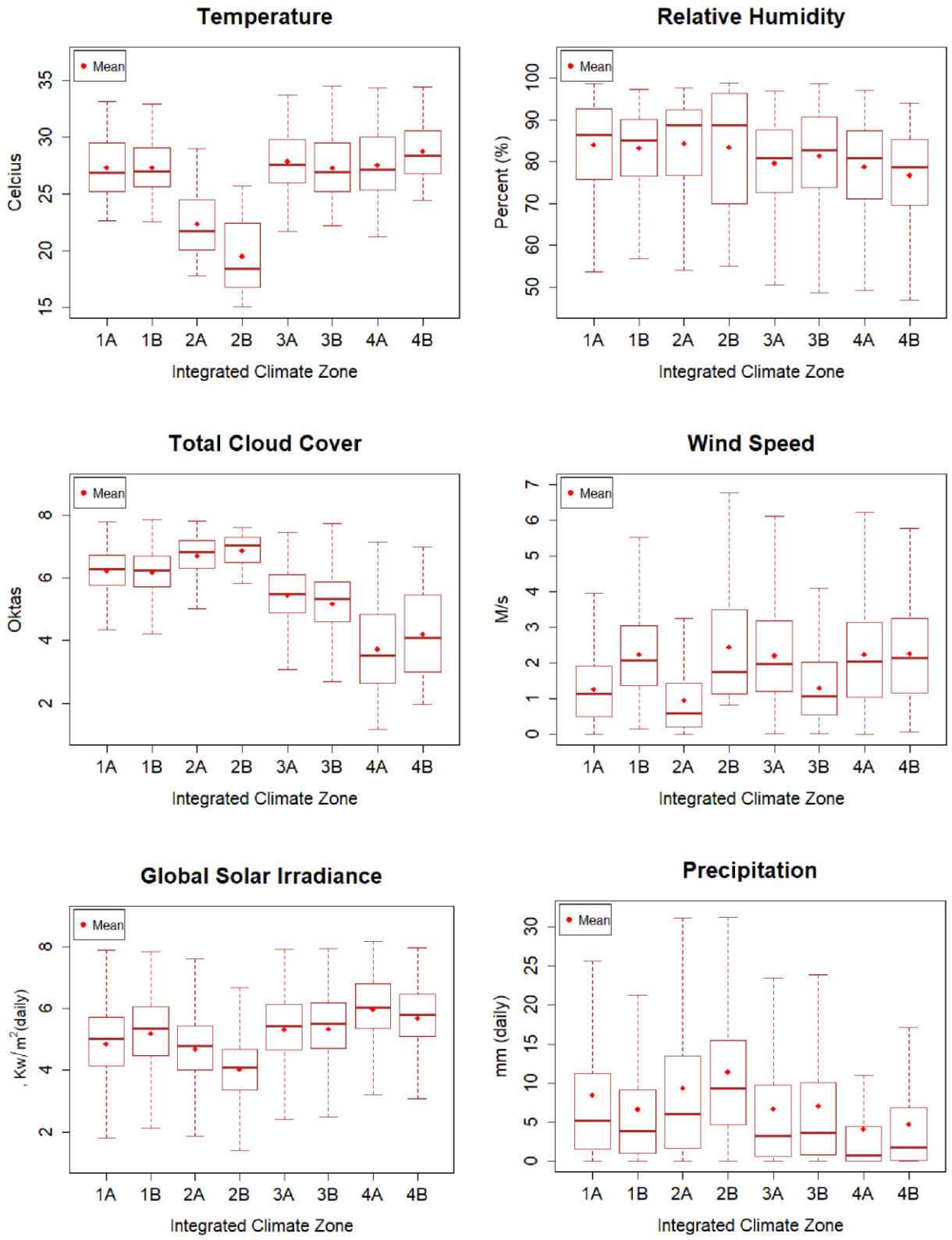

Figure 7. The variations of six climate factors in each integrated climate zones

Chapter 3. Assessment of passive cooling techniques in each climate zone

3.1 Introduction

Passive cooling techniques have been defined in various ways, e.g., in naturally ventilated buildings, comfort can be increased or indoor temperatures can be lowered through daytime ventilation when indoor temperatures in enclosed buildings are very high [77]. Comfort ventilation can be determined by calculating the period during which outside air flowing into a given building can be employed to dissipate excessive internal heat [78] [79]. Night ventilation is a passive cooling technique that removes heat from a building at night through the intake of cold outdoor air and reduces the rate of increase of the internal temperature during the day [80] [81]. Radiative cooling involves nocturnal longwave radiation heat loss to the sky [82] [83]. Direct evaporative cooling can be accomplished by lowering the temperature while increasing the humidity of ventilation air through water evaporation [73]. Indirect evaporative cooling via primary cooling results from evaporation, but the building is indirectly cooled without increasing the humidity in rooms, and soil is cooled for utilization as a cooling source for the building [65]. The evaporative cooling potential is based on a feasibility index, which is the wet-bulb temperature minus the difference between the dry- and wet-bulb temperatures. This index decreases with an increasing difference between the dry- and wet-bulb temperatures, i.e., with the decreasing relative humidity of the air. This indicates that the lower the feasibility index (the lower the relative humidity) is, the more efficient the evaporative cooling [84]. To study possible passive design strategies, the local conditions in which the house will be located should be evaluated in detail. While potentials of energy-saving in buildings are often determined based on the heating/cooling degree days alone as mentioned before, a wide range of climatic parameters should be considered in evaluation of the potentials of passive design strategies. Furthermore, to apply passive design strategies, it is necessary to consider the climatic conditions at the building site, including the general climate, meso-climate, and near-building climate, which can be determined based on the nearest elements or microclimate factors.

Several researchers have attempted to assess the potentials of passive design strategies using the so-called bioclimatic charts [66] [85] [86]. These studies determined the applicable ranges for respective passive techniques based on psychrometric charts [38][39][87]. The proposed

bioclimatic charts have been implemented in research as well as practices as useful design guidelines, but these charts cannot express the potentials in a plane information such as zoning maps. Moreover, the bioclimatic charts disregard some climatic variables that influence thermal behavior of buildings, such as solar radiation and wind exposure [54]. On the other hand, Lam et al. [38] developed a passive design zone, taking into account the different climates in China for the potential implementation of passive design strategies such as solar heating, natural ventilation, thermal mass with night ventilation, and evaporative cooling. Rakoto et al. [39] divided the island of Madagascar into six climate zones, in which each climate zone is assessed using a psychometric chart, to achieve indoor thermal comfort. Díaz-López [88] has studied the dynamics of climate changes and predicted changes of energy demand until 2085 in Spain. Bai and Wang [89] have defined a new thermal climate zone to determine an energy efficiency response to climate change in China. Bai et al. [90] have divided China into five main zones with 11 sub-zones with the criteria of heating/cooling degree days. Nevertheless, there are few studies that develop a comprehensive climate zoning system that is used for evaluating the potential of implementation of passive design strategies. This chapter focuses on the evaluation of passive cooling methods in each climate zone. The climatic cooling potential (CCP) formula was used to evaluate passive cooling approaches such as night ventilation, comfort ventilation, and evaporative cooling in various climate zones. The possible climatic zoning map for multiple passive cooling systems is proposed to eventually establish building laws for passive design buildings to assure Indonesia's future energy efficiency.

3.2 Methodology

3.2.1 Degree days and cooling load

Two climate-related energy consumption indicators for heating and cooling in buildings were considered, namely, the heating degree days (HDD) and cooling degree days (CDD). Degree days have been routinely used by building designers and engineers to estimate energy consumption related to indoor cooling and heating. Policymakers and researchers also use that information to forecast energy demands, consumption patterns and associated carbon emissions. CDD is an important climate indicator to estimate the climate-dependent cooling demand of each building. CCD is a simple method, and this measure provides a notable ability to represent the cooling or heating energy consumption. Indonesia is a tropical country with the relatively hot temperature throughout the year, therefore HDD information is not needed. Degree days are defined as the

monthly or annual summation of the difference between the base temperature (t_b) and the daily mean outdoor air temperature (t_0), whenever t_0 is larger than t_b (CDD). The value of t_b in this study was set at 24°C, 25°C, 26°C, and 27°C as the basis for the thermal comfort temperature of the building. CDD can be calculated using Equation 3.

$$\mathrm{CDD} = (1\ day)\sum_{days}(t_0 - t_b)^{+} \quad \text{(Eq. 3)}$$

where '+' denotes only positive values accumulated over n days during the chosen period (e.g., months, seasons, or years). t_0 and t_b in the above equation denote the daily mean of outdoor air and base (threshold) temperatures, respectively. Degree days are commonly represented as °C days, depending on the underlying units of t_0 and t_b considered in the formulation [91]. Cooling load calculations are an important part of estimating energy consumption in warm climates, especially in residential and commercial buildings. In addition, mechanical systems will still be required in most cases to support cooling loads, even after considering passive cooling strategies in the design of buildings and their facades [92]. In this study, the assumption of building temperature with various levels is 24°C, 25°C, 26°C, and 27°C. The percentage of cooling load is calculated when the air temperature in the outside environment reaches above the building temperature based on the total number of temperature observations per hour. The limits of building temperature for the calculation of the CDD and cooling load are assumed constant in this study, which in actual conditions can fluctuate [91].

3.2.2 Passive cooling techniques

Passive cooling techniques, namely, night ventilation, comfort ventilation, and evaporative cooling, were assessed in different climate zones using the climatic cooling potential (CCP) formula [93]. In this study, the cooling potential was calculated over a period of N (number of nights or days for 7 years) and then averaged into the daily potential in one year. CCP for night ventilation is defined as a summation of the differences between air temperature inside the building and outdoor air temperature, with a condition that the outdoor air temperature must be lower than the indoor air temperature. The number of cooling hours was calculated based on the temperature value by setting the base indoor air temperature (Tb) to 26°C, 27°C, and 28°C, reflecting the temperature range recommended for assessing thermal comfort. The magnitude of cooling

potential is calculated for 12 hours to assess the cooling potential of ventilation at night. The larger the temperature difference below Tb, the higher the potential for night ventilation. The building temperature is assumed to be constant with an infinite building mass [94]. CCP for night ventilation can be calculated using Equation 4.

$$CCP = \frac{1}{N}\sum_{n=1}^{N}\sum_{h=h_i}^{h_f} m_{n,h}(\mathrm{Tb} - \mathrm{T}) \qquad \text{(Eq. 4)}$$

h is the time of day {0..., 24 h}, where h_i and h_f represent the start and end times of night ventilation. In numerical analysis, it is assumed that night ventilation begins at h_i = 19.00 LT and ends at h_f = 06.00 LT. The potential for night ventilation considers that the greater the difference between the minimum outdoor temperature and the indoor air temperature, the greater the cooling capacity stored by the building structure. The CCP methods that have been developed, verified, and applied are suitable for all building types irrespective of the building-specific parameters. This is because the approach is solely based on the indoor air temperature factors within the temperature band [93]. The CCP for comfort ventilation is defined as a summation of the differences between indoor and outdoor wind speeds. The comfort ventilation potential is calculated based on the number of cooling hours, taking into account the wind speed throughout the day by setting the base indoor wind speed (WSb) to 1.8, 2, and 2.2 m/s for 24 hours. Generally, in the tropics, the wind speed is relatively low, so extreme wind speeds above 10 m/s are not considered for the application of this method. The greater the difference of outdoor wind speed over WSb, the higher the potential and the longer the duration of comfort ventilation. The CCP for evaporative cooling is defined as a summation of differences between indoor and outdoor relative humidity. The potential for evaporative cooling is determined based on the number of hours of cooling, taking into account the total relative humidity throughout the day by setting the base indoor relative humidity (RHb) to 60, 65, and 70 % for 24 hours. Generally, in the tropics, relative humidity is relatively high and rarely drops below 40%. The greater the difference of outdoor relative humidity under RHb, the higher the potential and the longer the duration of evaporative cooling. The determination of indoor environmental limits of Tb, WSb, and RHb for the calculations of potential night ventilation, evaporative cooling, and comfort ventilation in this study is considered constant, which in reality can fluctuate depending on the physical attributes of the building, including the thermal capacity of the building mass and window openings, among others [93].

3.3 Result and discussion

3.3.1 Effects of temperature and wind speed on the comfort ventilation potential

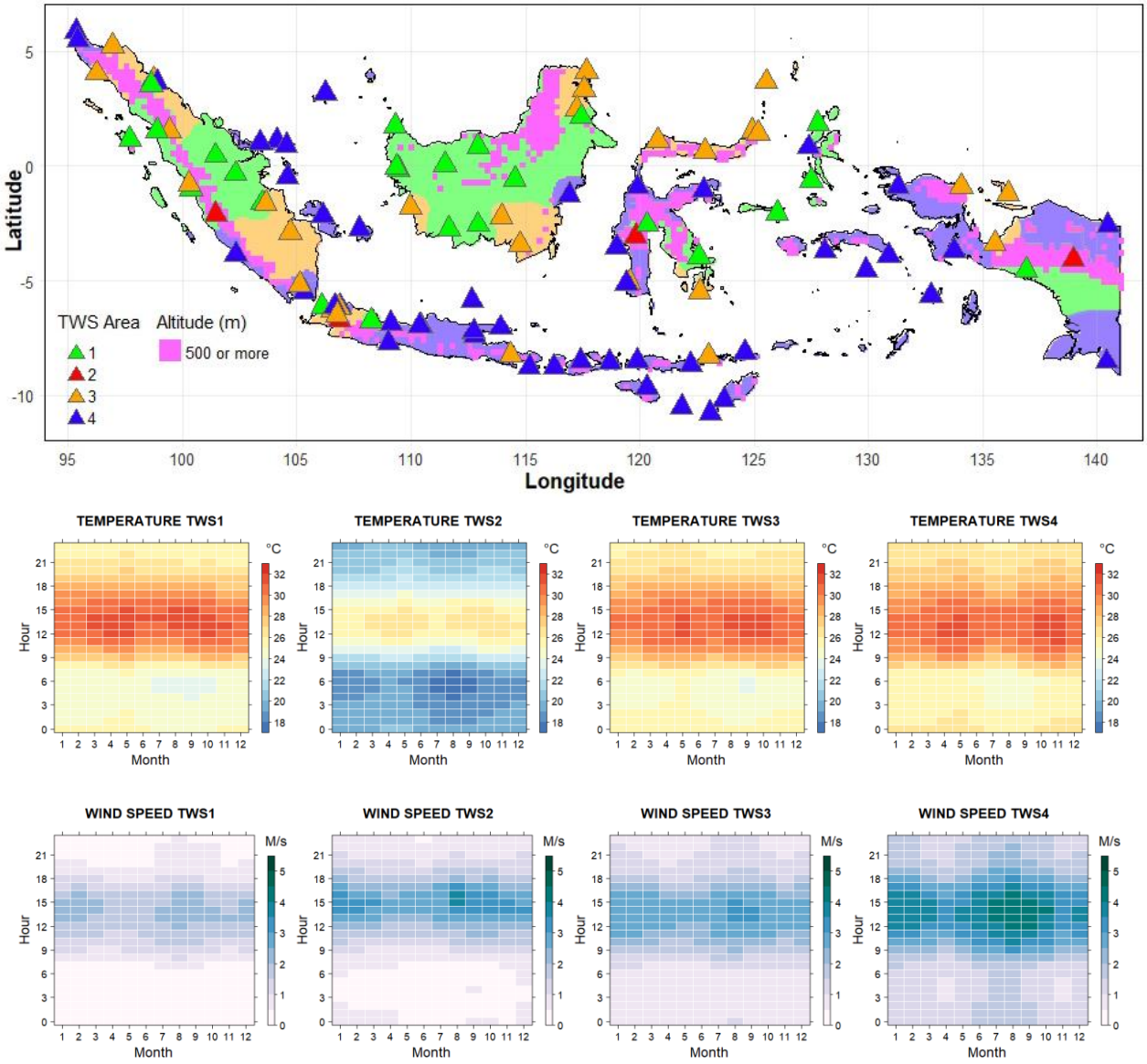

Figure 8. Temperature and wind speed (TWS) zones in Indonesia

Based on the clustering algorithm applied to the combination of air temperature and wind speed factors to divide the TWS zone and assess the cooling potential of comfort ventilation, an increase in air temperature was followed by an intensification in wind speed (Figure 8). Comfort ventilation assessment was carried out based on the combination of air temperature and wind speed.

In the heatmap analysis of the temperature, during the daytime period of 07:00 to 18:00 LT in the four TWS zones, air temperature in all parts of Indonesia remains relatively high (above 26 °C), which falls outside the limits of thermal comfort [67], except at the TWS2 zone covering the Kerinci region of Jambi Province, Citeko of West Java Province, Tana Toraja of South Sulawesi Province, and Wamena of Papua Province, where the air temperature still falls in the range of thermal comfort because their location are in high elevation. Comfort ventilation to achieve indoor thermal comfort is very effective in the TWS2 zone because the daytime temperature is relatively low, and the wind speed remains relatively high. Analysis of the heatmap of the daytime wind speed values, i.e., in the TWS4 and TWS3 zones, showed the relatively high wind speed values reaching more than 1.8 m/s in Nusa Tenggara, Java, Bangka Belitung Islands, Batam to Natuna, South Sulawesi, Maluku Islands, and southern Papua. These areas have the potential for the application of comfort ventilation to lower the air temperature and to create thermal comfort indoors based on the daytime wind speed. At night, from 19:00 to 06:00 LT, the wind speed in the four TWS zones was relatively weak, but the TWS4 zone exhibited a higher wind speed than that in the other three TWS zones, which reflects the potential for nighttime comfort ventilation at wind speed values ranging from 1 to 2 m/s along with a decrease in temperature. The TWS1 zone is predominantly located near the equator, encompassing Sumatra, Kalimantan, Sulawesi, Maluku, and Papua, with relatively high daytime temperature and weak wind conditions. Consequently, the TWS1 zone has less potential for comfort ventilation methods based on wind speed.

Figure 9 shows the number of hours when the given climate conditions meet the required values for comfort ventilation during daytime and nighttime throughout the year. The adaptive comfort assessment used in comfort ventilation adopted the adaptive comfort standards for naturally ventilated buildings, which depend on outdoor temperatures [95]. This study set the outdoor air temperature limit to be under 29°C and wind speeds surpassing 1.8 m/s, although the resultant performance of wind-driven ventilation depends mainly on the wind pressure distribution on the buildings and the type and size of openings, among other factors [71,72]. The total hours can be used to determine the operating schedule of windows and the ventilation for optimization. Thus, the total hour on comfort ventilation potentials directly affects the level of potential energy use [79]. Figure 9 shows that the TWS1 zone is an area with the potential for comfort ventilation involving the smallest number of hours, i.e., approximately 1 hour during the day and less than 1 hour at night. The TWS2 zone shows a high potential for comfort ventilation, reaching 4 to 6 hours

during the day and decreasing to 1 to 2 hours at night. The TWS3 zone represents the potential of comfort ventilation involving 1 to 2 hours during the day and 2 to 3 hours at night. The TWS4 zone provides the potential of comfort ventilation with a seasonal cycle that varies from 1 hour in May and November and peaks in August at 3.5 hours during the day. In contrast, at night, the comfort ventilation potential reaches 2 hours in May and November and reaches 6 hours in August. The detailed probability values of the comfort ventilation potential in each TWS zone are provided in Table 4. Based on the probability of comfort ventilation, the TWS1 zone is the area with the lowest total number of hours and percentage, while the TWS2 zone is the area with the highest total number of hours and percentage following the order of TWS1 zone < TWS3 zone < TWS4 zone < TWS2 zone during the daytime, nighttime, and daily.

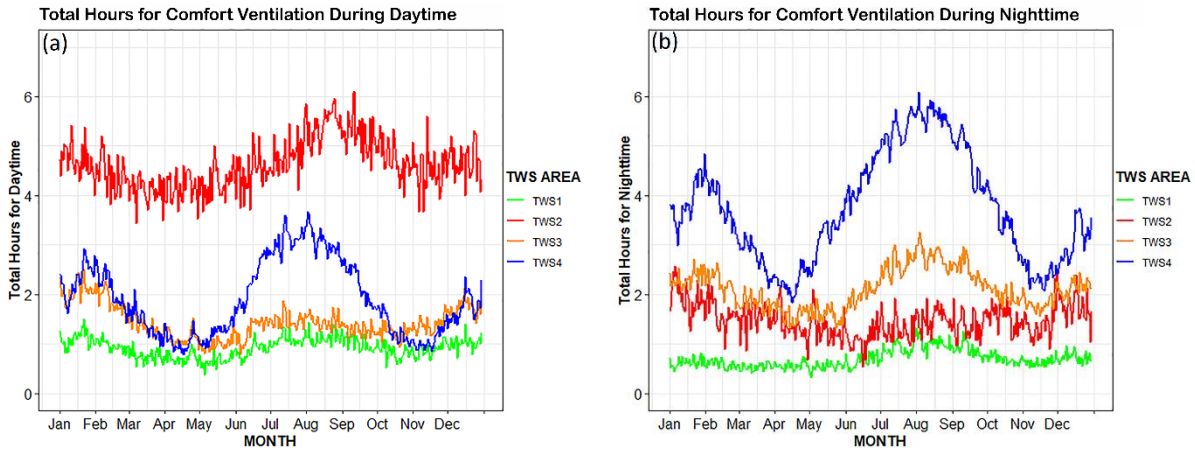

Figure 9. Number of hours regarding the comfort ventilation potential: (a) daytime; (b) nighttime

Table 4. Probabilities of the comfort ventilation based on the combination of the temperature and wind speed

TWS zone	**Comfort ventilation potential**		
	Daytime	**Nighttime**	**Daily**
1	7.7 %	5.8 %	6.8 %
2	38.6 %	12.3 %	25.5 %
3	12.0 %	17.6 %	14.8 %
4	15.9 %	31.1 %	23.5 %

3.3.2 Effects of the relative humidity and wind speed on the evaporative cooling potential

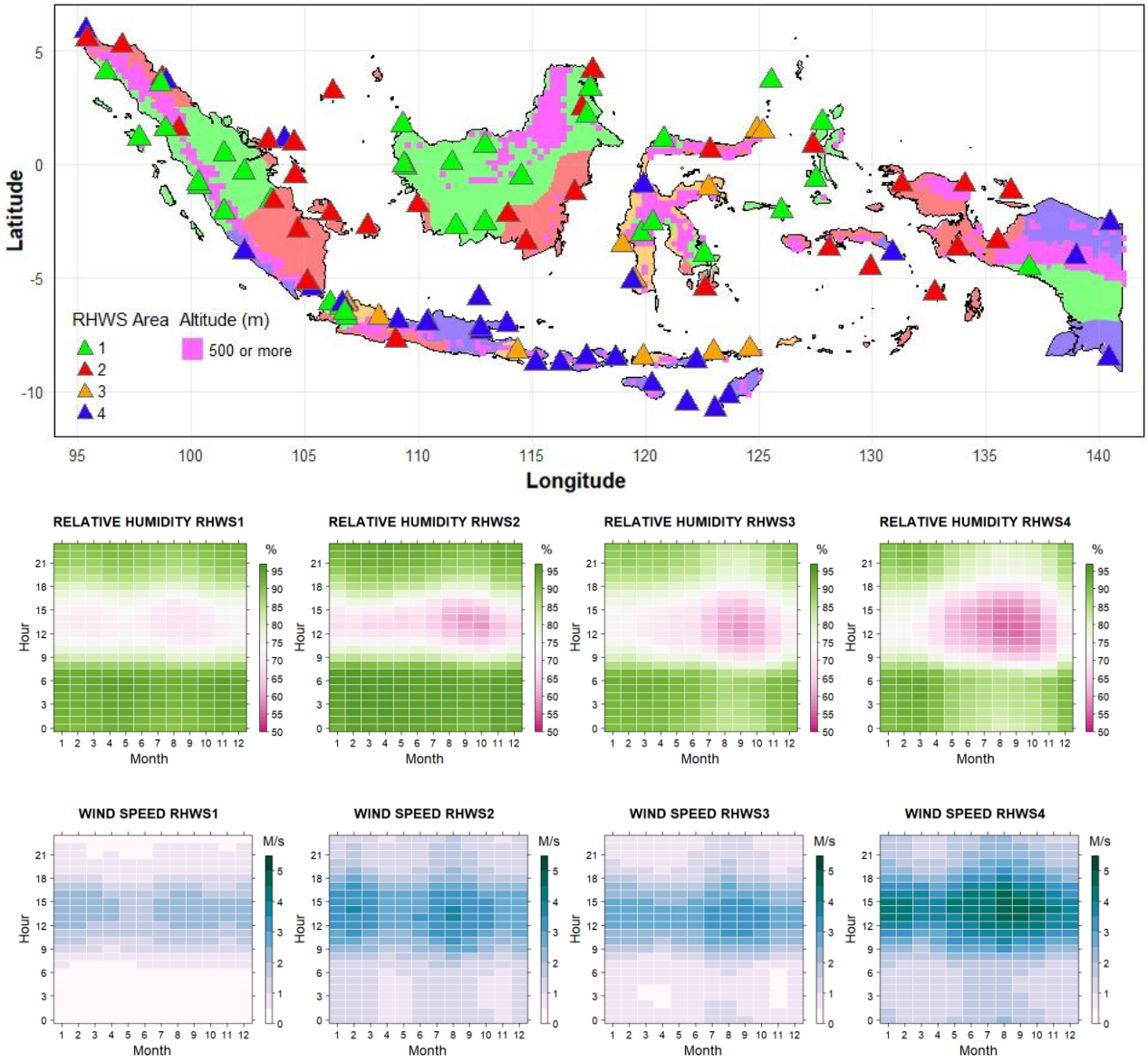

Figure 10. Relative humidity and wind speed (RHWS) zones in Indonesia

Based on the cluster algorithm applied to the combinations of relative humidity and wind speed factors, the diurnal variation in the four RHWS zones revealed an opposite relationship between the relative humidity and wind speed factors, where a decrease in relative humidity was followed by an increase in wind speed (Figure 10). In the relative humidity heatmap analysis of the previous section, during the day in the four RHWS zones, the relative humidity decreased to different extents. The lowest decrease in relative humidity occurred in the RHWS4 zone covering Nusa Tenggara, East Java, South Sumatra, South Sulawesi, the Maluku Islands, and East Papua.

RHWS3 zone covering Nusa Tenggara, Java, and Sulawesi also attained a relatively low relative humidity during the day from 08:00 to 19:00 LT, dropping below 70%, which indicates comfortable conditions based on relative humidity [67]. The RHWS4 and RHWS3 zones become potential areas for the application of evaporative cooling due to the relatively low relative humidity and the strong winds that may enhance the potential of evaporative cooling during the day in both zones. The RHWS1 zone covering Sumatra, Kalimantan, Sulawesi, North Maluku, Papua, and West Java has relatively high relative humidity conditions that were almost always above 70 %. The RHWS1 zone exhibits less potential for the application of passive methods involving evaporative cooling during the day. At night, the relative humidity increases in all RHWS zones reaching above 70%, but slight decreases were observed in the RHWS4 and RHWS3 zones in June, August, and September due to the relatively strong winds at night reaching up to 2 m/s.

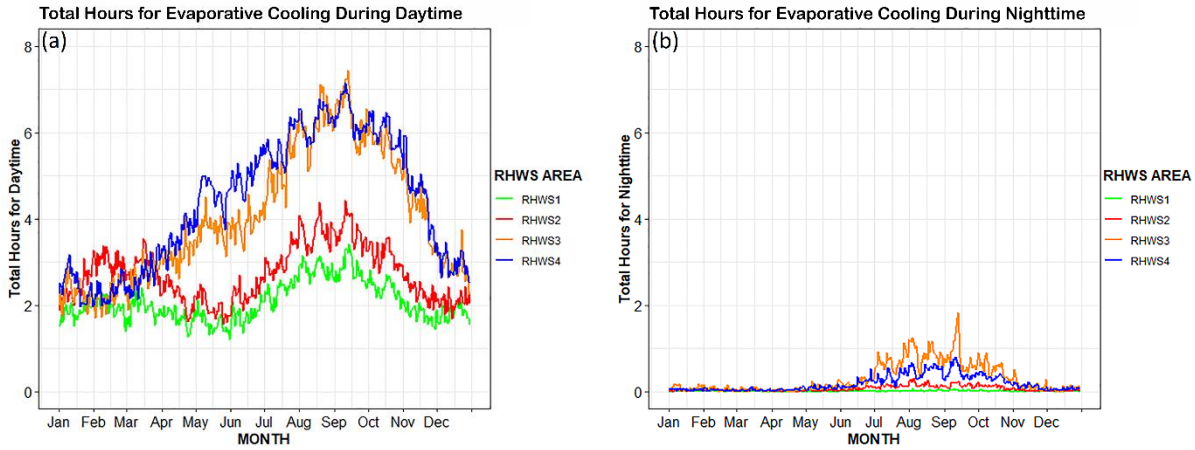

Figure 11. Number of hours regarding the evaporative cooling potential: (a) daytime; (b) nighttime

Figure 11 shows the number of hours in term of evaporative cooling potential during the day and night. In this study, a relative humidity below 70% and wind speeds exceeding 1.8 m/s were considered sufficient to provide evaporative cooling effects on human thermal comfort in tropical regions. The RHWS1 zone has the smallest number of hours for evaporative cooling potential which only ranges from approximately 2 to 3 hours during the day. The RHWS2 zone demonstrates the evaporative cooling potential ranging from 2 to 4 hours during the day. The profiles of evaporative cooling potential are almost the same between the RHWS3 and RHWS4 zones, ranging from 2 to 7 hours during the day and varying in season. On a seasonal basis, an increase in the evaporative cooling potential occurs from July to November, peaking in September and

October in all RHWS zones. The evaporative cooling potential is very low at night. The RHWS3 zone reaches an evaporative cooling potential of approximately 1 hour in August and September, while in other months the evaporative cooling potential remains below 1 hour. Apart from the RHWS3 zone, the potential of evaporative cooling is always less than 1 hour at night. The detailed probability values of the evaporative cooling potential for each RHWS zone are provided in Table 5. Based on the analysis, the day and night evaporative cooling potential decreases in the order of RHWS1 zone < RHWS2 zone < RHWS3 zone < RHWS4 zone.

Table 5. Probabilities of the evaporative cooling based on the combination of relative humidity and wind speed

RHWS zone	**Evaporative cooling potential**		
	Daytime	**Nighttime**	**Daily**
1	17.3 %	0.1 %	8.7 %
2	22.7 %	0.6 %	11.7 %
3	33.7 %	2.5 %	18.1 %
4	36.4 %	1.5 %	19.0 %

3.3.3 Passive cooling potential of each climate zone

After the classification of climate zones based on the spatial and temporal homogeneity of climate values, it is important to study diurnal climate variations of air temperature, relative humidity, and wind speed to determine the upper/lower limits for passive cooling methods. The ranges of diurnal climate factors in Indonesia vary in each climate zone, some shows clear seasonal cycles. The very highland tropical climate zone exhibited a large variation in diurnal ranges: air temperatures ranging from 9 °C to 12 °C, relative humidity ranging from 40 to 50 %, and wind speed ranging from 5 to 11 m/s. The sub-equatorial climate zone exhibited a narrow diurnal temperature range which ranged from approximately 6 °C to 7 °C, and the relative humidity ranged from approximately 25 to 30 %. The highland tropical climate zone attained the smallest diurnal range of wind speed, with an average value of approximately 3 m/s. The ranges of diurnal temperature and relative humidity increased in August, September, and October in the sub-monsoonal, monsoonal, savanna and sub-savanna climate zones. The diurnal range of wind speed increased from January to February and from September to November in all climate zones with varying wind speeds range. The patterns of the diurnal temperature, relative humidity, and wind speed in each climate zone are shown in Figure 12.

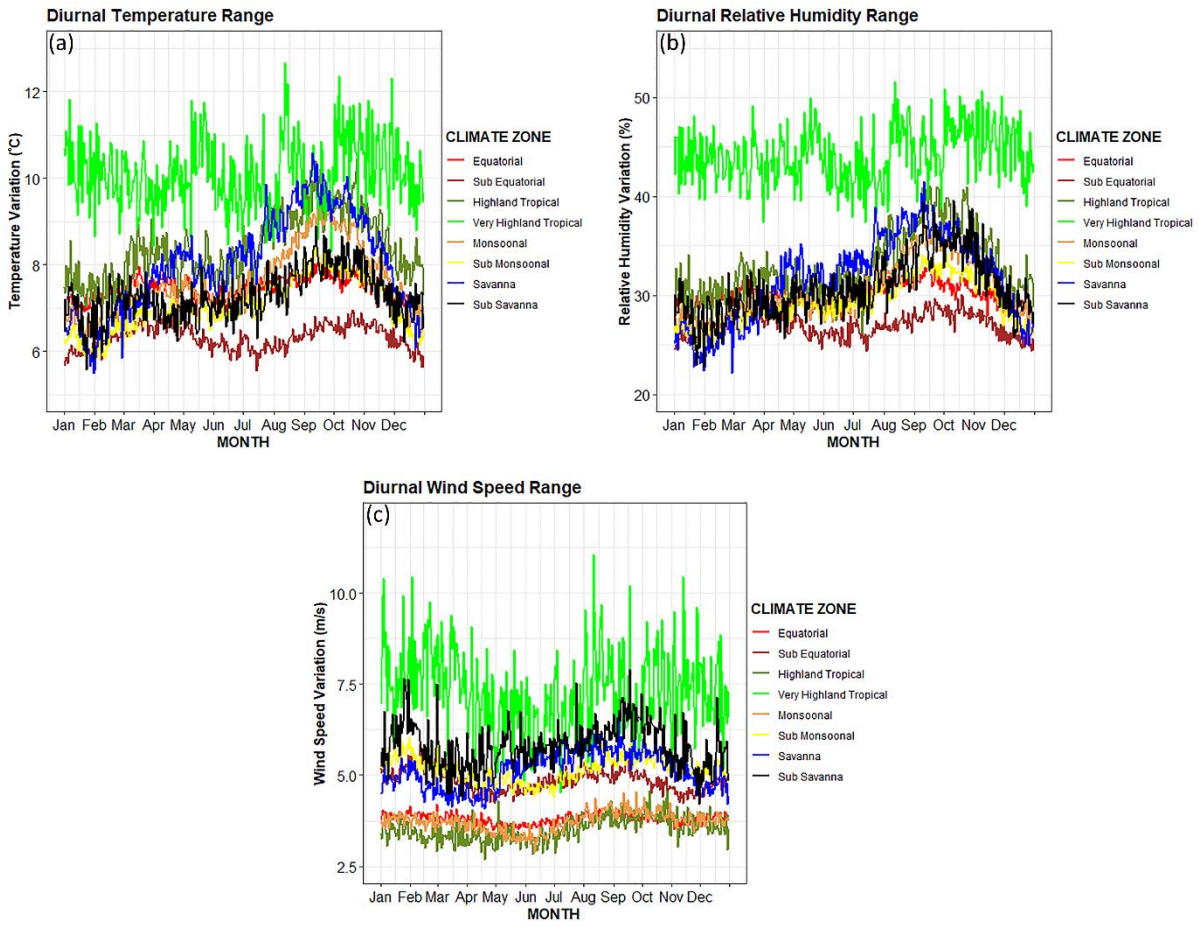

Figure 12. Diurnal range of the climate values: (a) temperature; (b) relative humidity; (c) wind speed

After identifying the diurnal range of the air temperature, relative humidity and wind speed, the next step involved analyzing of the cooling load and CDD/year. Based on the calculation results of CDD with the different air temperature base values, the highest value of CDD of 24 °C was attained over the CDD 25 °C to CDD 27 °C levels within the same climate zone. The highland tropical climate zone and very highland tropical climate zone attained a CDD value of 0/year on a temperature base value, ranging from 24 °C to 27 °C. An increase in the value of CDD was followed by a rise in the cooling load, and vice versa. The largest value of CDD of 24 °C was attained in the sub-savanna climate zone, namely, 1739.5/year, which was followed by a cooling load of 98.8% when the air temperature was above 24 °C. In contrast, the smallest value of CDD of 27 °C was observed in the very highland tropical climate zone at 0/year, which was followed by a cooling load of 1.6% when the air temperature exceeded 27 °C. The values of CDD and the percentages of cooling load for each climate zone with the different climate base values are summarized in detail in Table 6.

Table 6. Values of CDD and percentages of the cooling load

Integrated climate zone	1A	1B	2A	2B	3A	3B	4A	4B
	Equatorial	Sub-equatorial	Highland tropical	Very highland tropical	Monsoonal	Sub-monsoonal	Savanna	Sub-savanna
CDD 24°C/year	1210.1	1210.6	0	0	1203.9	1408.0	1291.9	1739.5
CDD 25°C/year	884.8	845.4	0	0	838.6	1042.7	972.1	1374.1
CDD 26°C/year	479.5	480.1	0	0	473.5	677.4	572.2	1009.1
CDD 27°C/year	131.4	135.6	0	0	140.2	319.3	267.9	648.4
Cooling load > T 24°C	90.6 %	93.6 %	27.7 %	14.1 %	87.5 %	95.0 %	88.7 %	98.8 %
Cooling load > T 25°C	74.8 %	81.1 %	20.9 %	8.6 %	73.8 %	85.6 %	77.4 %	94.6 %
Cooling load > T 26°C	58.7 %	64.1 %	14.6 %	4.4 %	59.6 %	70.7 %	63.5 %	84.1 %
Cooling load > T 27°C	46.6 %	48.4 %	9.4 %	1.6 %	47.8 %	56.2 %	51.2 %	68.7 %

Applicable passive design strategies can be chosen to achieve indoor thermal comfort based on the characteristics of climate zones in Indonesia (Figure 13). The potential of night ventilation was determined based on the temperature difference between the outdoor air and the building structure at night to achieve cooling of the building mass (Figure 13.1). In the calculation of the night ventilation potential, three values of Tb (26°C, 27°C and 28°C) based on the comfort temperature range were set assuming a constant indoor temperature with infinite building mass. The pattern of night ventilation potential remained relatively the same for all three bases according to the seasonal cycle in each zone, but differences were observed in the difference between Tb and the outdoor air temperature. Calculations using a Tb of 28°C resulted in a large amount of cooling storage capacity compared to Tb values of 27°C and 26°C for the night ventilation potential. This finding is attributed to the increase in the difference between the minimum outdoor air temperature and the indoor air temperature, which eventually increases in the cooling storage capacity of the building structure. The cooling capacity stored by the building at night will be used for effective

indoor cooling during the day.

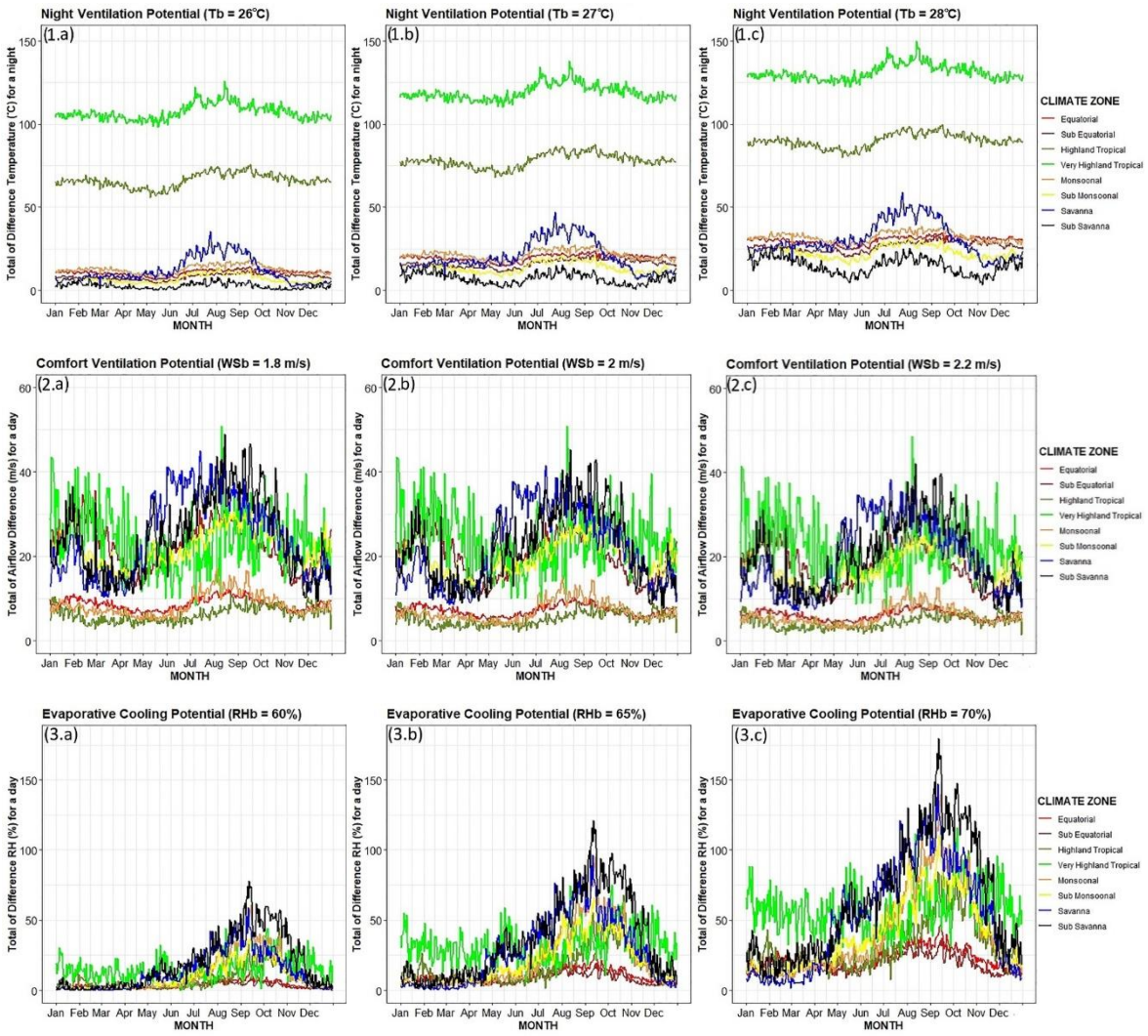

Figure 13. Daily CCP based on the differences between the outdoor climatic conditions and the assumed indoor climatic conditions: (1.a-c) night ventilation; (2.a-c) comfort ventilation; (3.a-c) evaporative cooling

Considering the calculation results of comfort ventilation potential and evaporative cooling potential using the three threshold values of WSb and RHb, a seasonal cycle pattern was produced for each passive technique as well as in each climate zone (Figure 13.2 and Figure 13.3). Regarding comfort ventilation, the potential calculation using a WSb value of 1.8 m/s resulted in an increase in the total wind speed difference, which was greater than that obtained with WSb values of 2 and 2.2 m/s. The number of differences in the outdoor wind speed above the WSb determines the duration of potential comfort ventilation in one day. The higher outdoor wind speed over WSb, the greater the difference and the longer the duration of comfort ventilation. Additionally, the

calculation of the evaporative cooling potential used an RHb value of 70%. This resulted in the rise of the total relative humidity difference greater than the RHb values of 65 and 60%. The difference number between the outdoor relative humidity and RHb affects the duration of evaporative cooling. The lower relative humidity below RHb, the higher the potential of evaporative cooling and the longer the duration of evaporative cooling.

The night ventilation potential graph (Figure 13.1) shows that the very highland tropical and highland tropical climate zones exhibited a high potential for night ventilation because these areas are located at high elevation with relatively low temperatures. Moreover, the sub-savanna climate zone is located on Madura Island which has the lowest potential for night ventilation. Months with an increased potential for night ventilation in all climate zones in Indonesia included July, August, September, and October. The comfort ventilation potential graph (Figure 13.2) shows that the sub-savanna and savanna climate zones located on the islands of East Nusa Tenggara and West Nusa Tenggara attained a high potential because these areas are influenced by strong monsoon circulation. The very highland tropical climate zone also achieved a high comfort ventilation potential. Moreover, the equatorial, highland tropical, and monsoonal climate zones, located near the equator, are areas with the lowest comfort ventilation potential. Months with an increased potential for comfort ventilation in all climate regions in Indonesia included July, August, September, and October which are influenced by the southeast monsoon, and December, January, and February which are influenced by northeast monsoons [16]. The evaporative cooling potential graph (Figure 13.3) shows that the sub-savanna, savanna, monsoonal and sub-monsoonal climate zones exhibited the potential for high evaporative cooling in July, August, September, and October with a decrease in relative humidity in these areas. In addition, the equatorial and sub-equatorial climate zones located near the equator were the areas with a low potential for evaporative cooling due to the high relative humidity levels in these areas throughout the year. The probabilities of the assessed passive cooling potential based on the different climatic base values regarding the night ventilation potential (Night VP), comfort ventilation potential (Comfort VP) and evaporative cooling potential (ECP) in each integrated climatic zone are provided in Table 7. The analysis carried out in this study should be seen as a preliminary approach to assessing the passive cooling potential based on climate zoning. To obtain more detailed results, it is necessary to conduct detailed simulations of certain types of buildings in each climate zone using a building energy simulation that considers various other factors.

Table 7. Potentials of the three passive cooling methods with the different base climatic values

Integrated climate zone	1A	1B	2A	2B	3A	3B	4A	4B
	Equatorial	Sub-equatorial	Highland tropical	Very highland tropical	Monsoonal	Sub-monsoonal	Savanna	Sub-savanna
Night VP Tb < 26°C	25.2 %	19.0 %	79.1 %	91.4 %	26.2 %	14.8 %	22.6 %	5.4 %
Night VP Tb < 27°C	41.3 %	35.9 %	85.4 %	95.6 %	40.4 %	29.3 %	36.5 %	15.9 %
Night VP Tb < 28°C	53.4 %	51.6 %	90.6 %	98.4 %	52.2 %	43.7 %	48.8 %	31.3 %
ECP RHb < 70 %	14.2 %	12.3 %	16.0 %	24.6 %	19.9 %	21.0 %	24.7 %	26.9 %
ECP RHb < 65 %	7.4 %	5.9 %	10.0 %	18.0 %	11.7 %	12.0 %	15.8 %	17.6 %
ECP RHb < 60 %	3.2 %	2.6 %	5.3 %	10.8 %	6.4 %	6.2 %	8.7 %	10.8 %
Comfort VP WSb > 1.8 m/s	32.7 %	56.0 %	23.1 %	44.5 %	32.4 %	53.2 %	55.8 %	54.2 %
Comfort VP WSb > 2 m/s	22.6 %	45.5 %	16.0 %	35.2 %	21.9 %	43.0 %	46.5 %	43.4 %
Comfort VP WSb > 2.2 m/s	22.4 %	45.2 %	15.7 %	34.8 %	21.5 %	42.9 %	46.2 %	43.3 %

Chapter 4. Study of vertical solar irradiance in Tangerang and Jembrana-Bali of Indonesia

4.1 Introduction

Humans living in buildings need comfortable thermal conditions for their activities. While excessive heat in a room has made conditions uncomfortable, active cooling systems have been used to achieve thermal comfort for the last several decades. Currently, the use of active building cooling which is sourced from fossil energy has become a problem because it contributes to global warming. The main source of heat for buildings is solar radiation [97]. Solar heat gain has contributed almost half of the total cooling load in buildings [98]. When a building gets more solar radiation it will cause more cooling needs in the room [99].

The building sector has contributed one-third of global energy consumption of which 38% comes from Heating Ventilation and Air Conditioning Systems (HVAC)[100]. Building energy conservation is required to combat climate change in accordance with the Paris Agreement 2030. Local climate conditions and solar radiation exposure affect the thermal comfort of the people living in the building [101][102]. In regions with four seasons, buildings need energy for cooling and heating. Meanwhile, in tropical areas around the equator, buildings require cooling energy throughout the year. It is important to consider local climate factors based on climate zones to design buildings with passive cooling techniques for energy efficiency in the future. Indonesia already has eight climate zones for passive cooling, namely equatorial, sub-equatorial, highland tropical, very highland tropical, monsoonal, sub-monsoonal, savanna, and sub-savanna (see Figure 6 in Chapter 2).

One of the most important climate variables for the design and simulation of energy-efficient buildings is solar radiation [103][104][105]. Studying the impact of solar radiation on the building envelope is one of the earliest judgments when starting to design a building. This relates to the indoor layout design and its relationship to the outdoors through windows and openings to determine heat gain. A widely adopted measure in many countries to improve energy-efficient building design is the Overall Thermal Transfer Value (OTTV) of solar radiation [106]. The OTTV

value is a measure of the average heat gain into the building through the building envelope which can be used to determine building insulation.

Solar radiation has several components, including global horizontal irradiance and global vertical irradiance with four orientations namely north, east, south, and west. Global Horizontal Irradiance is defined as the total amount of solar radiation received on a horizontal surface, including direct and diffuse radiation. Meanwhile, global vertical radiation refers to the total solar radiation received from all parts of the sky on a surface perpendicular to the ground. It measures the intensity of solar radiation that reaches the Earth's surface on a vertical surface. In addition to the solar radiation component, a clearness index analysis is needed to categorize sky conditions that affect the amount of radiation reaching the surface.

Several studies have been found that examine the use of solar radiation data and its effect on building design applications related to energy efficiency. For example, Sepúlveda et al. [107] developed an easy-to-use solar radiation-based prediction method for facade design of office buildings with design parameters including room size, window-to-floor ratio, and thermal/optical properties of glass located in urban canyons to balance sunlight. He et al. [108] developed a model to predict the Roof Thermal Transfer Value (RTTV) of a green roof under a tropical climate based on solar radiation. Hwang and Chen [109] analyzed the impact of solar radiation on the relative importance of passive solar design on office building facades for cooling loads and thermal comfort in hot-humid climates. Song et al. [110] analyzed the long-term effect of solar radiation on indoor thermal comfort in office buildings in different climate zones whose results showed that the effect of solar radiation on thermal comfort was more severe in cold climate zones.

Geographically, Indonesia is a country in the tropics near the equator. Many climatic factors ranging from global scale, regional scale to local scale [21] affect the condition of climate elements in Indonesia in a diurnal cycle including land-sea breeze[20], seasonal cycles including monsoons [111] and annual cycles including el nino [15]. According to the climate classification in Indonesia, the city of Tangerang is included in the monsoonal climate zone which has relatively hot temperatures throughout the year during the day and has wind directions that vary seasonally with wind speeds in the weak category. With hot conditions throughout the year this causes this area to have a high need for building cooling throughout the year. It is important to analyze solar radiation in more detail for the design of buildings with sustainable energy efficiency in different climate zones [112].

The study of solar radiation is important for making design guidelines in building energy-efficient buildings in the future. Information from solar radiation on the building envelope is important in designing solar devices for building applications [113]. Solar radiation is divided into several components, each component can be used to assess heat gain [114]. For example: Direct and diffuse radiation data are very important to determine the amount of solar heat gain entering the building [115]. Horizontal solar data can be used to study horizontal fenestrations such as skylights. Besides solar radiation, four environmental parameters determine outdoor thermal comfort, namely air temperature, relative humidity, wind speed, and solar radiation. It should be noted that, different from the indoor environment, solar radiation significantly affects outdoor thermal comfort, which needs to be comprehensively understood and analyzed [116].

Designing buildings using passive cooling techniques is one of the adaptation solutions to reduce the effects of global warming [117]. Building interior design including Windows plays an important role in establishing energy consumption and thermal comfort. Several recent studies have used passive cooling techniques to cool down the temperature in the room. Passive cooling techniques include comfort ventilation [118] and night ventilation [80]. Comfort ventilation is taking into account the flow of outdoor air that is entered into the room through the window. While the night ventilation technique is to utilize the minimum temperature storage at night in the building structure which is used to withstand the rate of heating during the day. For example, in ref [110] evaluated the effect of solar radiation on occupants in an office building under different orientations and climate zones.

We conducted analysis in two locations, namely in Tangerang and in Jembrana-Bali of Indonesia. First, this research is a preliminary study that aims to determine the pattern of solar radiation intensity in the daytime and seasonal cycles in two horizontal components and four vertical components in Tangerang. Global irradiance on horizontal surfaces and vertical surfaces is very important to determine the thermal and energy performance of buildings. Local-scale climate assessment is also carried out to see the variability and range of climate on a diurnal and seasonal basis so that the boundaries for determining the boundaries of the thermal comfort zone can be identified. The last is assessing the potential of two passive cooling technique methods, namely daytime comfort ventilation and night ventilation. Second, the study presents a preliminary study of solar radiation on the global horizontal and vertical components of irradiance in north, east, south, and west orientations under different sky conditions, through a case study in Jembrana-

Bali, Indonesia. This study focuses on evaluating solar radiation data based on annual and seasonal cycles under different sky conditions. In the final section, a sun-path analysis is performed based on the relationship between the zenith angle, azimuth angle, and each component of solar radiation intensity concerning time. By comprehensively analyzing solar radiation parameters, architects and engineers can determine the best building orientation, shading strategy, and window design to maximize natural light, minimize solar heat gain, and optimize energy supply planning. In the end, all of this information can be used to design sustainable buildings and energy planning in the future.

4.2 Methodology

First, this study uses historical solar radiation data from horizontal components including global horizontal irradiance and infrared irradiance. Meanwhile solar radiation from the vertical component includes north vertical surface irradiance, south vertical surface irradiance, west vertical surface irradiance and east vertical surface irradiance. All components of solar radiation are measured using six pyranometer sensors manufactured by Kipp and Zonen CMP21. Meanwhile, climate elements include data on water temperature, surface wind speed, relative humidity, dew point from the Automatic Weather Station which have been observed in Tangerang for 1 year starting from January 2021 to December 2021 (Figure 14). The temporal resolution of irradiation observations is every 10 seconds, while Automatic Weather Station is 1 minute away. The difference in the observation resolution interval is equated to hourly resolution with the average variable at the same hour. Analysis of filtered solar radiation from 05.00 to 19.00 local time. Analysis at nighttime was not carried out because the irradiance value at night-time was 0. Meanwhile, the analysis of climate elements used the full 24 hours (night-time and daytime).

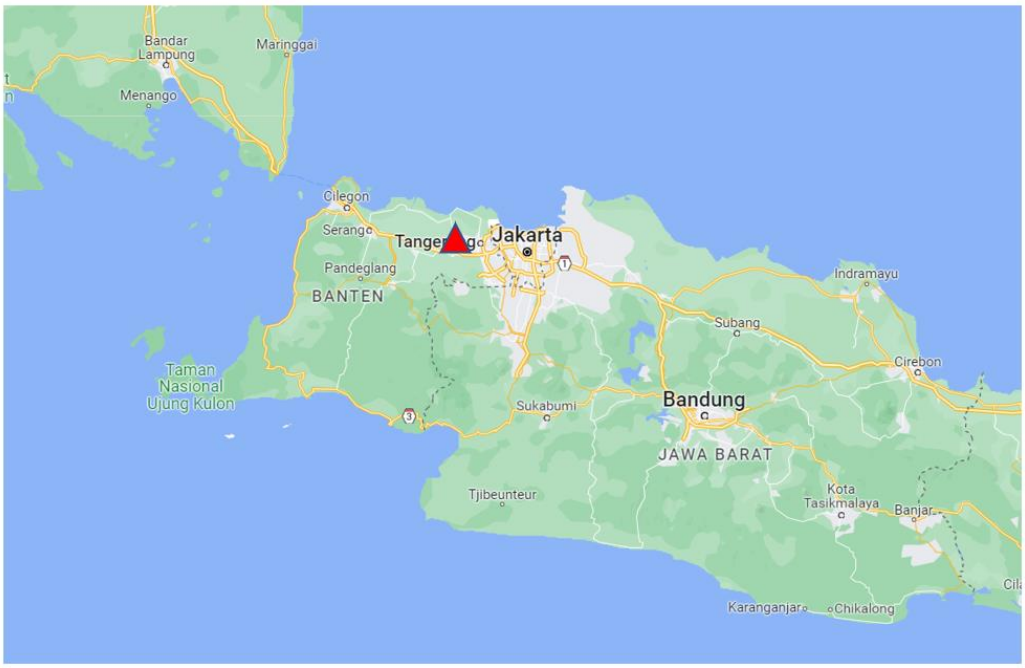

Figure 14. (Red triangle) Research locations in Tangerang of Indonesia

The flow of data processing from this research is first to compare the radiation intensity of the four vertical components, namely north, south, east, and west. The second analyzes the intensity of solar radiation by averaging the month and the same hour so that daytime and seasonal information is obtained for each component. The third is to analyze climate elements including temperature, relative humidity, dew point, and wind speed by averaging the month and the same hour so that diurnal and seasonal information is obtained for each climate element. Furthermore, an analysis of the direction frequency and wind speed in four different sub-seasons is December to February (DJF), March to May (MAM), June to August (JJA), and September to November (SON). The last is to calculate the potential of passive cooling techniques for daytime comfort ventilation and night ventilation. The calculation of the daytime comfort ventilation method is carried out to see the hourly probability starting from 06.00 – 18.00 by assuming the minimum wind speed limit is 2 m/s, so when the wind speed rises above 2 m/s it is considered the potential for the daytime comfort ventilation method. Calculation of the night ventilation method is carried out to see the minimum hourly temperature starting from 19.00 - 06.00 by assuming the minimum temperature limit is 26^{o}C, so when the minimum temperature drops below 26^{o}C it is considered the potential for night ventilation. The daytime comfort ventilation and night ventilation methods are carried out every month from January 2021 to December 2021.

Second, solar radiation observation data for this study were obtained from five pyranometer sensors installed at the Bali Climatology Station (8.34°S, 114.61°E) located in Jembrana Regency, Bali province, Indonesia. Based on climate classification updates, Jembrana-Bali is located within the monsoonal climate zone. The hourly solar radiation data set is filtered for one year from July 2022 to June 2023. The components of solar radiation measured are the elements of horizontal global irradiance, vertical global irradiance with east, west, north, and south orientations. Documentation of research equipment and locations can be seen in Figure 15. The analysis process of this research is divided into three stages. The first stage, namely the global components of horizontal and vertical solar irradiance is analyzed based on annual and sub-diurnal patterns. In the annual pattern analysis, each component of solar radiation is filtered based on the same month, so that the maximum and minimum intensity values are obtained for a certain month. In the sub-diurnal pattern analysis, each component of solar radiation is filtered based on the same hour, so that the maximum and minimum intensity values are obtained at certain hours. In the second stage, the components of solar radiation are separated based on hourly clearness index intervals based on Table 8. Specifically, hourly clearness indexes are also analyzed based on annual and sub-diurnal patterns. In the third stage, the intensity of solar radiation is analyzed based on the sun-path from the relationship between the solar zenith angle, azimuth angle and changes in the intensity of each solar radiation component over time.

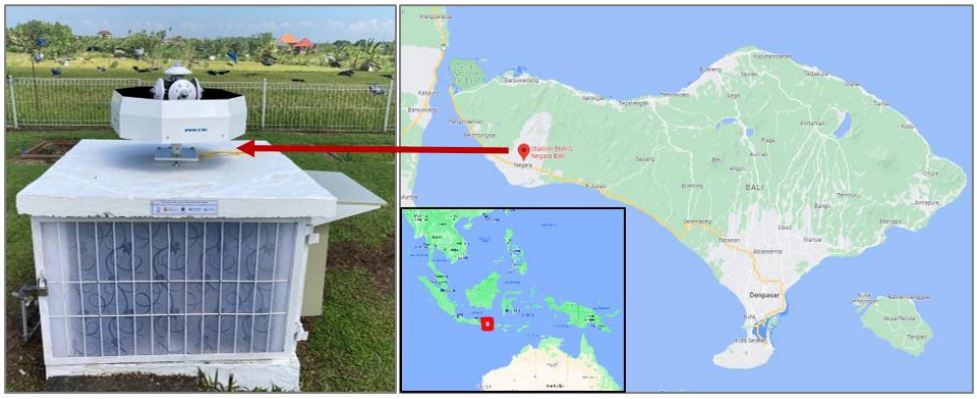

Figure 15. Research location in Jembrana-Bali, Indonesia

The clearness index is used to distinguish sky conditions. The clearness index is defined as the ratio of global solar radiation measured at ground level to extra-terrestrial radiation in the upper atmosphere. The clearness index (K_t) ranges from 0 to 1, with a value close to 1 indicating a clear

sky and a value close to 0 indicating a cloudy sky (overcast). Sky criteria based on the clearness index can be seen in Table 8.

Table 8. Clearness index intervals [119].

clearness index (K_t) intervals	**sky cover condition**
$0 \leq K_t < 0.35$	Cloudy sky
$0.35 \leq K_t < 0.55$	Partially cloudy sky
$0.55 \leq K_t < 0.65$	Partially clear sky
$0.65 \leq K_t < 1$	Clear sky

The hourly values of the clearness index (K_t) for the study can be calculated based on Eq. (1).

$$k_t = \frac{I}{I_o} \qquad \text{(Eq. 5)}$$

Where I is the measured hourly global horizontal irradiance (W/m²) and I_o is the hourly extraterrestrial solar radiation at the top of the atmosphere (W/m²). Extraterrestrial radiation is the theoretical amount of solar energy that would be available on a horizontal plane on the earth's surface if the earth were not surrounded by an atmosphere. The hourly extraterrestrial radiation (I_o) on a horizontal plane can be calculated based on Eq. (2).

$$I_o = \frac{43200}{\pi} I_{sc} 1 + 0.033 \cos\frac{360\,N}{365} \cos\varphi \cos\delta \sin\omega_2 - \sin\omega_1 \frac{\pi\omega_2 - \omega_1}{180} \sin\varphi \sin\delta \qquad \text{(Eq. 6)}$$

Where I_{sc}=1367 W/m² is the solar constant. ω_1 is the hour angle at time t = t_1 and ω_2 is the hour angle at t = t_2. N is the day number. φ is the latitude of the site and δ is the declination angle.

4.3 Results and discussion

4.3.1 Analysis of vertical solar irradiance in Tangerang

Most of the solar radiation is emitted at visible and infrared wavelengths. Incoming solar radiation is a key factor affecting architectural design because solar radiation causes an increase in temperature inside buildings due to heat transfer [99]. Global horizontal irradiance is the total amount of short wave radiation that reaches the earth by way of the horizontal surface to the surface

of the object [120]. Figure 16 shows that global horizontal irradiance measurements have a high intensity throughout the year in Tangerang. On a diurnal basis, the intensity of the sun reaches its maximum at around 11.00 LT to around 14.00 LT. seasonally, the global horizontal irradiance increases in March-April and September-October, which are the equinoxes. The intensity of solar radiation varies as a function of geographic location, calendar days, and hours of day. Therefore, measurements without a scale are needed to compare results, regardless of location, date, and time [121].

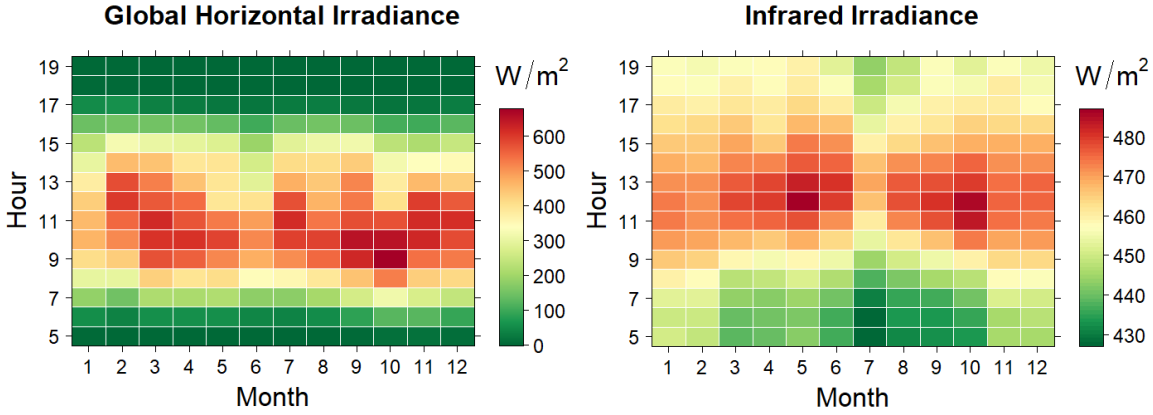

Figure 16. Heatmap for global horizontal irradiance and infrared irradiance in Tangerang

In addition to global horizontal irradiance, the study of infrared irradiance intensity is an important approach to increase the efficiency of solar energy utilization, which has practical scientific value and application significance [122]. Global infrared radiation can be obtained from several existing measurement stations or by building radiation modeling methods [123]. Based on heatmap analysis month by month from 05.00 LT to 19.00 LT, the average hourly infrared irradiance intensity ranges from 396 w/m^2 to 500 w/m^2, the infrared irradiance intensity reaches its maximum value around 12.00 LT. seasonally the lowest infrared intensity occurs in July while the maximum occurs in May and September during 2021 in Tangerang.

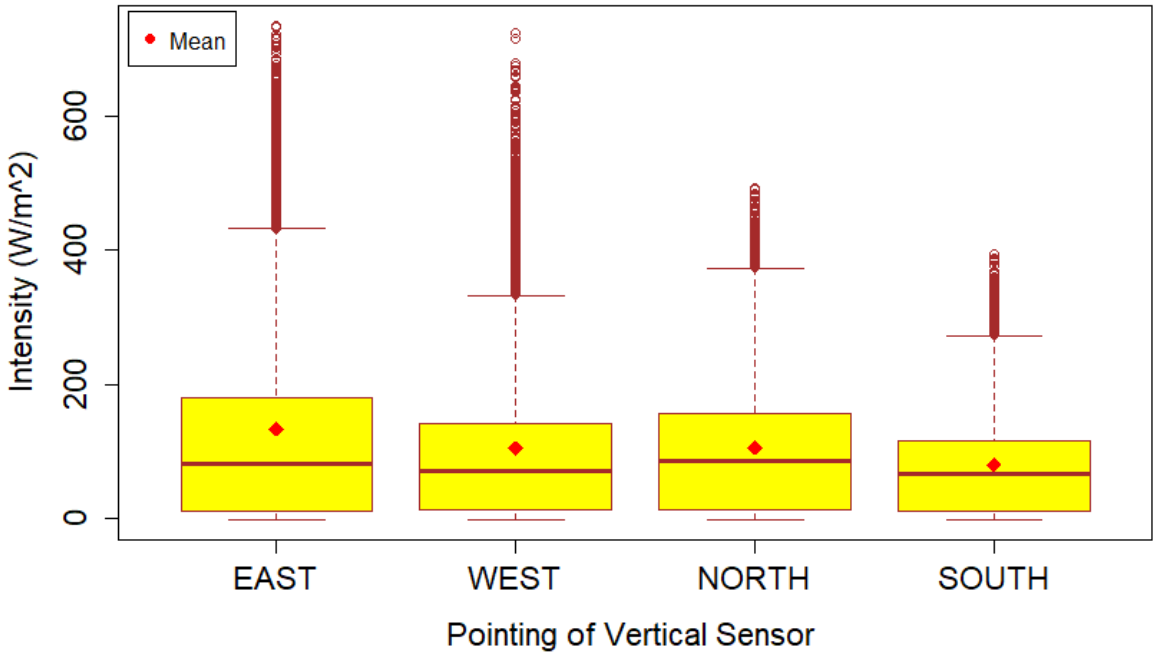

Figure 17. Comparison of the intensity of the four directions of the vertical pyranometer

Solar radiation especially on vertical surfaces from north, south, east, and west is very important for the design of energy efficient buildings and natural lighting schemes. for active solar energy applications such as building-integrated photovoltaics and passive energy-efficient building designs a vertical global component is also required. Due to several things that have been mentioned solar irradiation measurements need to be carried out for the global vertical component [124]. Figure 17 shows the boxplot of the four-way vertical surface pyranometer comparison from 05.00 LT to 19.00 LT in Tangerang. Based on the four vertical directions, it was found that the vertical radiation from the east direction showed the highest intensity, namely an average of 133.4 w/m^2 and a maximum value of 736.1 w/m^2. the vertical intensity from the west is influenced by local climate conditions, namely the condition of few clouds with clear skies in the morning. for the radiation value from the west direction the average is 104.2 w/m^2 with a maximum value of 725.3 w/m^2 this is smaller than when compared to the vertical from the east due to more cloud cover occurring during the day to night [125]. Vertical irradiance from the south direction is the lowest with a maximum value of 393.6 w/m^2 and an average of 79.0 w/m^2 compared to the north direction, the lowest vertical surface irradiance intensity from the south is due to the geographical location of Tangerang which is south of the equator [121]. for solar radiation from the north direction the maximum value is 493.4 w/m^2 with a mean value of 105.5 w/m^2.

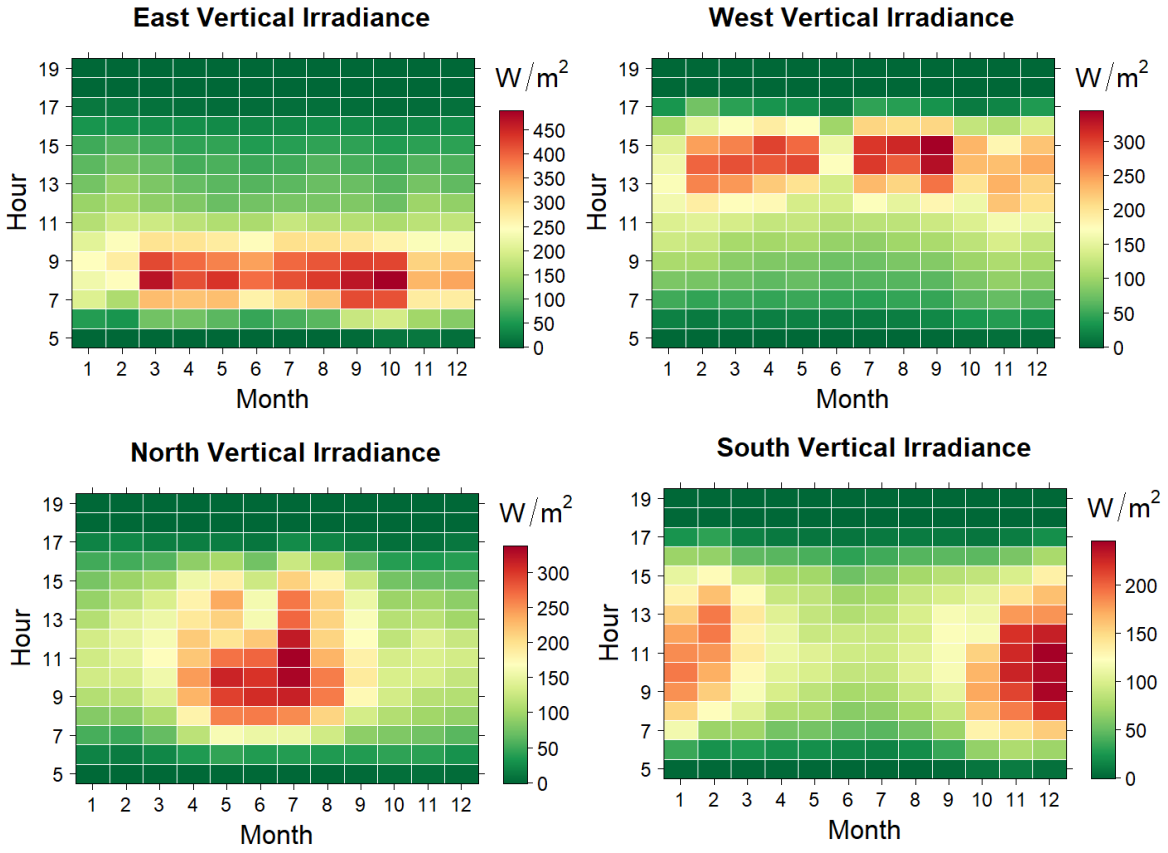

Figure 18. Heatmap comparison of four directions of vertical surface irradiance

Figure 18 shows a comparison of the daytime and seasonal patterns of vertical surface irradiance from the four directions, namely north, south, east, and west. The vertical irradiance pattern from the north and south shows that the annual movement of the sun from the equator/equinox to 23.5 north latitude and 23.5 south latitude has affected the intensity in both vertical directions [126]. The pyranometer sensor towards the north recorded an increase in radiation intensity from March to September. The pyranometer sensor towards the south recorded an increase in radiation intensity from October to March. The vertical irradiance pattern from the east and west shows that the diurnal movement of the sun has affected the intensity in both vertical directions. In general, the eastward pyranometer sensor records an increase in radiation intensity from sunrise around 06.00 LT to around 12.00 LT. while the pyranometer sensor to the west recorded an increase in radiation intensity at around 12.00 LT until sunset at around 18.00 LT. seasonally, there is a decrease in intensity on the east and west sensors from November to February due to the rainy season and the large number of clouds in this region [127]. cloud conditions can

affect global horizontal irradiance depending on the reach and position of the clouds relative to the sun [128].

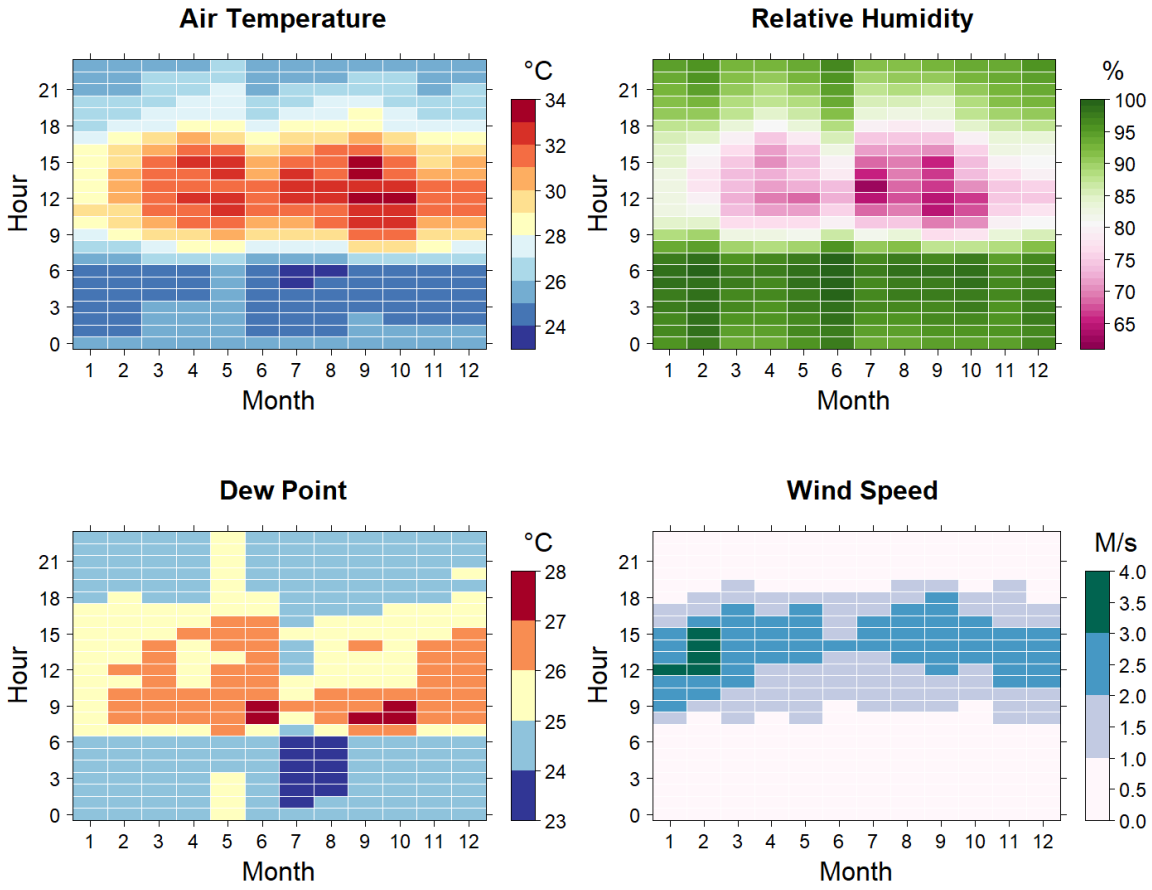

Figure 19. Heatmap of diurnal and seasonal local climate scale averages

Figure 19 shows that the Tanggerang area is a hot area during the day throughout the year with an average maximum of 33.5^{o}C and slightly decreases at night with a minimum average diurnal temperature of 23.7^{o}C. The pattern of the sun's annual movement has affected the pattern of seasonal temperature, this can be seen from the increase in temperature around March and September when at that time the position of the sun is above the equator. Relative humidity conditions decrease during the day and increase at night throughout the year. The seasons of July, August, September, and October are the seasons with the lowest RH conditions. The average minimum RH is 62.6% and the average maximum RH is 99.6%. The dew point can be defined as the temperature below which water droplets start to condense and form dew. Or it is the temperature to which air must be cooled in order to be saturated with water and water vapor [129].

When cooled further, the water vapor condenses on the water. Figure 19 shows that the Dew point condition recorded an increase during the day to reach a maximum of 27.3ºC and decreased at night to reach a minimum of 23.3ºC. in a diurnal pattern, the wind speed increases during the day, ranging from 1 m/s to a maximum average wind speed of 3.5 m/s. the wind speed tends to decrease (calm) at night throughout the year. Seasonally, the highest wind speeds occur in the seasons of December, January, and February [21].

Figure 20. Frequency of wind direction and speed; (SON) Sep-Nov, (DJF) Dec-Feb, (MAM) Mar-May, (JJA) Jul-Aug.

Figure 20 shows the frequency of wind direction and speed analysed on a sub-seasonal basis. Basically, the wind direction and wind speed can change diurnally and seasonally depending on the strength of the influence of climatic phenomena. Based on the climate zone, the city of Tangerang is in the monsoon season zone, which means that in this area there are seasonal changes in wind direction. Based on the wind rose frequency chart, it can be seen that the dominant wind from the Dec-Feb season comes from the west (WSW to N) which indicates that the air mass originates from the Asian continent [15]. While the July-August season the dominant wind comes from the east (N-SSE), which means the wind comes from Australia [16]. The Sep-Nov period is

the transition season I, showing the dominant wind comes from WSW which is the wind direction transition period I. The Mar-May period is the II transition season, showing wind directions that vary from SSW to ESE which is the wind direction transition period II. Based on information from wind speed and direction analysis to maximize air flow into the building, the window design should be made to face east, north, and west.

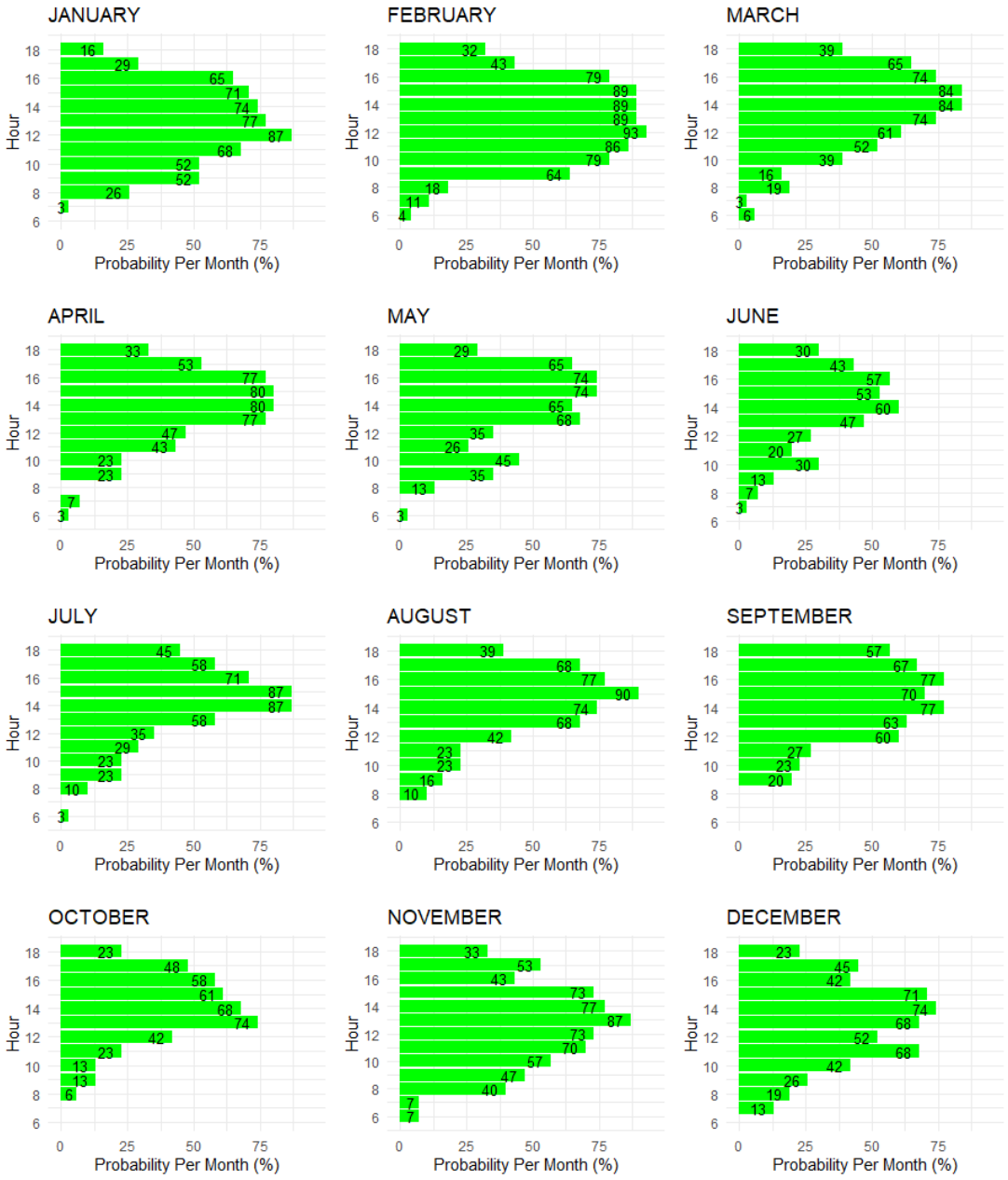

Figure 21. Daytime comfort ventilation potential

Daytime comfort ventilation is affected by wind speed conditions during the day [130]. This study assumes that the wind speed is 2 m/s as a limitation for airflow to enter and be ventilated

through the window, so that when the wind speed reaches above 2 m/s there is a potential that can flow through the window as comfort ventilation. Figure 21 shows an hourly graph of the probability of daytime comfort ventilation starting at 06.00 LT to 18.00 LT. The monthly chart shows that all months during the day there is potential and suitable for comfort ventilation techniques. If viewed every hour during daytime, there is a potential for a slow rise from 08.00 LT and the potential with the highest probability occurs between 12.00 LT to 16.00 LT. After 16.00 LT the potential for daytime comfort ventilation decreases slowly.

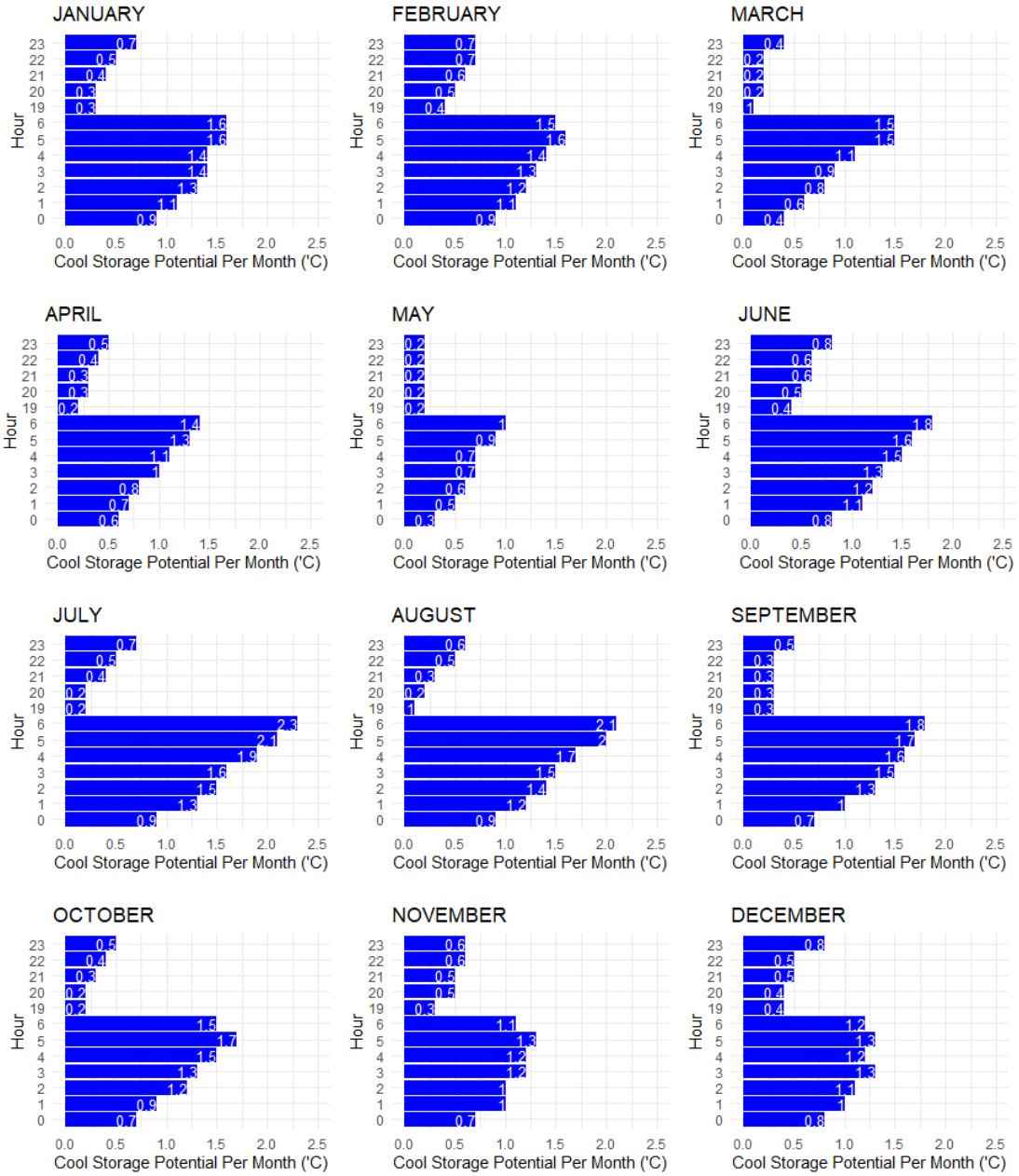

Figure 22. Night ventilation potential

Night cool storage potential is affected by the minimum temperature at night [93]. Figure 22 above shows a graph of the hourly cool storage potential starting at 19.00 until 06.00 LT with temperature (T) set at 26^{o}C. This study assumes that a temperature of 26^{o}C as a limit for building structures can store cold capacity, so when the temperature drops below 26^{o}C is the potential for cold that can be stored in building structures [80]. Based on the monthly analysis, it can be seen that throughout the year (every month from January to December) there is potential for cool storage with relatively slightly different values every hour. The monthly graph shows an increase in potential starting at 19.00 local time and reaching its peak at 06.00 local time.

4.3.2 Analysis of vertical solar irradiance in Jembrana-Bali

In general, annual (January to December) and sub-diurnal (06.00 LT to 18.00 LT) variations of global and vertical solar irradiance elements can be influenced by geographic location, climate, and typical weather at a location. Solar radiation on monthly global horizontal and vertical components on the surface at Jembrana-Bali for one year is presented in detail in Figure 23. It can be seen that within a year the global horizontal and vertical irradiance components have fluctuated in intensity and formed an annual pattern. The maximum monthly global horizontal irradiance average occurred in January of 432.4 W/m², while the minimum monthly global horizontal irradiance average occurred in July of 327.9 W/m². The average monthly minimum south vertical irradiance occurred in June at 43.1 W/m², while the maximum monthly average occurred in January at 160 W/m². The maximum average monthly north vertical irradiance has occurred in June of 266.9 W/m², while the minimum monthly average has occurred in December of 75.8 W/m². The maximum average monthly east vertical irradiance occurred in March at 202.6 W/m², while the minimum monthly average occurred in October at 141.9 W/m². The maximum average monthly west vertical irradiance has occurred in June of 152.4 W/m², while the minimum monthly average has occurred in November of 109.3 W/m².

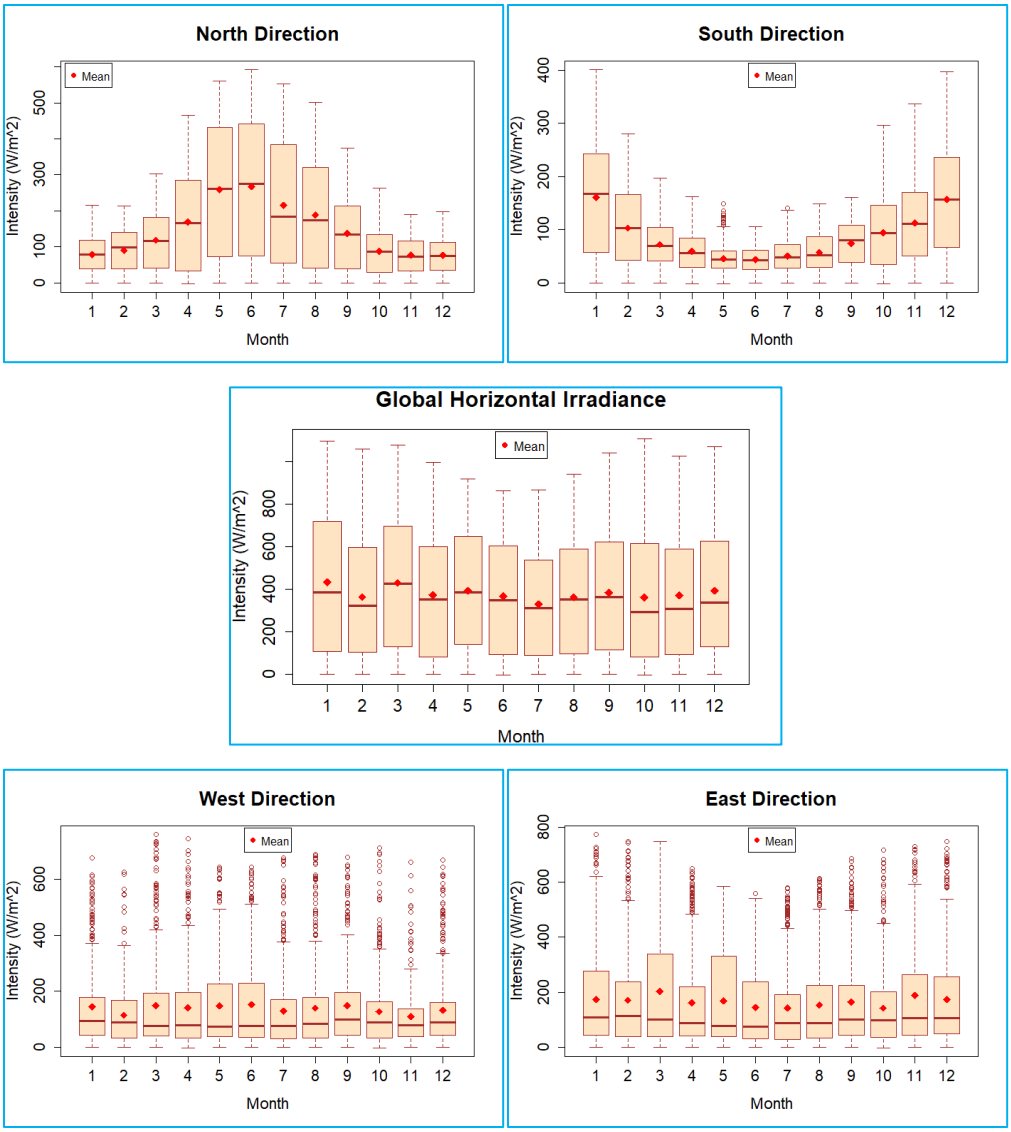

Figure 23. The annual pattern of solar radiation components

The solar radiation component for global horizontal and vertical irradiance in the semi-diurnal pattern at Jembrana Bali for one year is presented in detail in Figure 24. It can be seen that within a year the global horizontal and vertical irradiance components have fluctuated and formed a clear semi-diurnal pattern. The maximum hourly average global horizontal irradiance occurred at approximately 12.00 LT with a value of 723.4 W/m², while the minimum hourly average occurred at approximately 18.00 LT with a value of 5.2 W/m². The maximum hourly south vertical irradiance average occurred at approximately 12.00 LT with a value of 129.5 W/m², while the minimum hourly average occurred at approximately 18.00 LT with a value of 4.1 W/m². The maximum average hourly north vertical irradiance has occurred at approximately 10.00 LT with a

value of 260.3 W/m², while the minimum hourly average has occurred at approximately 18.00 LT with a value of 1.2 W/m². The maximum average hourly east vertical irradiance has occurred at approximately 08.00 LT with a value of 429.2 W/m², while the minimum hourly average has occurred at approximately 18.00 LT with a value of 1.3 W/m². The average maximum hourly west vertical irradiance has occurred at approximately 14.00 LT with a value of 304.3 W/m², while the average hourly minimum has occurred at approximately 18.00 LT with a value of 6.6 W/m².

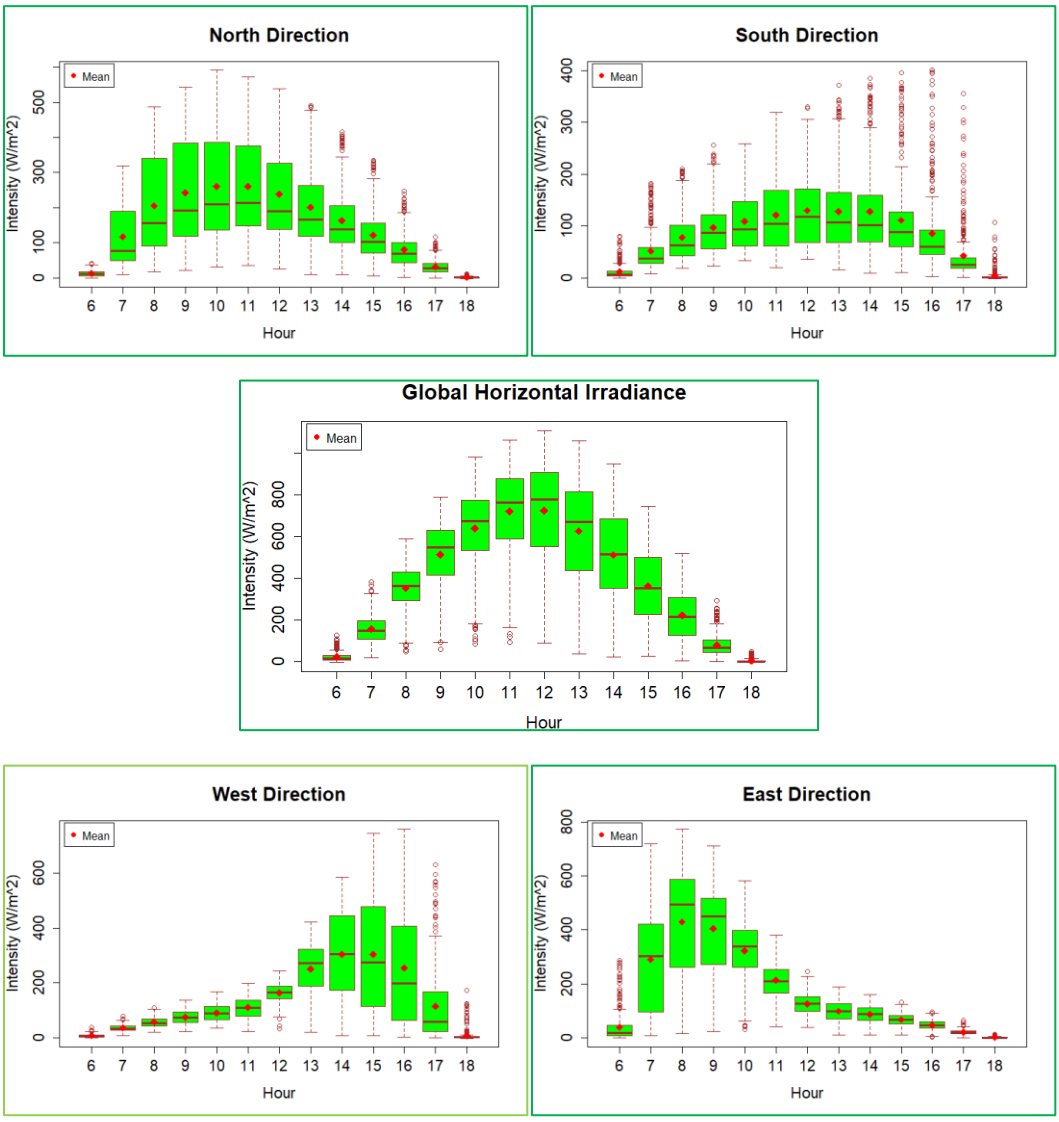

Figure 24. The sub-diurnal pattern of solar radiation components

A comparison of the sub-diurnal pattern and annual global horizontal and vertical solar irradiance patterns from four directions, namely north, south, east, and west in detail is shown in Figure 25. The pyranometer sensor orientation to the north recorded an increase in radiation

intensity from March to September and reached maximum intensity in June at approximately 10.00 LT to 12.00 LT. while the south orientation pyranometer sensor recorded an increase in radiation intensity from October to March and reached its maximum intensity in January at approximately 11.00 LT to 14.00 LT. The annual pattern of vertical irradiance intensity with north and south orientation has shown that the annual movement of the sun from the equator (March) to a maximum declination angle of 23.5 north latitudes (June), returns to the equator (September) and leads to a maximum declination angle of 23.5 south latitudes (December) has affected the intensity in both vertical directions in Jembrana-Bali. This finding is also in line with previous research conducted in Tangerang of Indonesia [10], which is geographically located south of the equator.

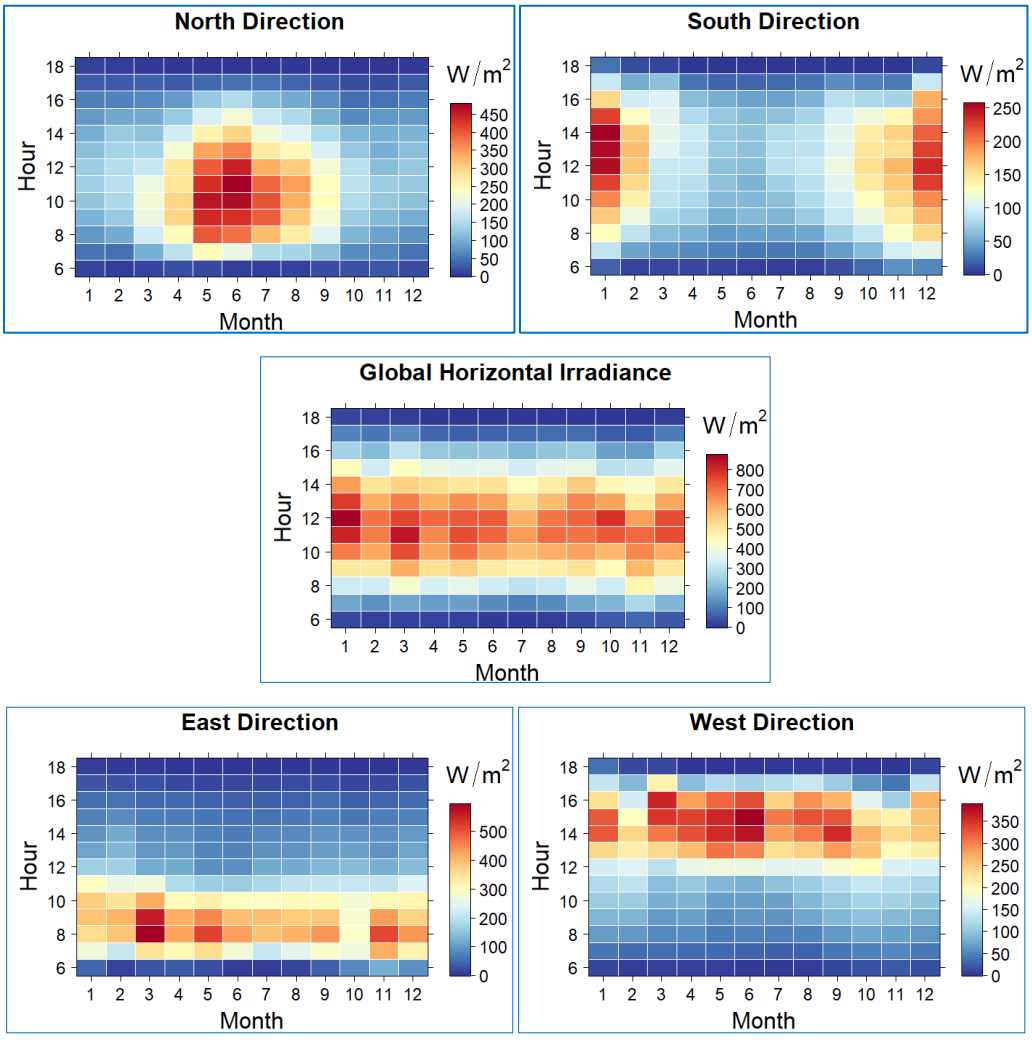

Figure 25. The patterns of daytime and annual components of solar radiation

The increase in global vertical east irradiance starts at sunrise at approximately 06.00 LT to at approximately 12.00 LT, while the increase in global vertical west irradiance starts at 12.00 LT

until sunset at approximately 18.00 LT. On an annual basis, the decrease in intensity of the global vertical west irradiance from November and December is made possible by the growth of clouds and rain that occurs in the afternoon (between 12.00 LT and 18.00 LT), while the decrease in intensity in the global vertical east irradiance from January and February is made possible by the growth of clouds and rain that occurs in the morning (between 06.00 LT to 12.00 LT).

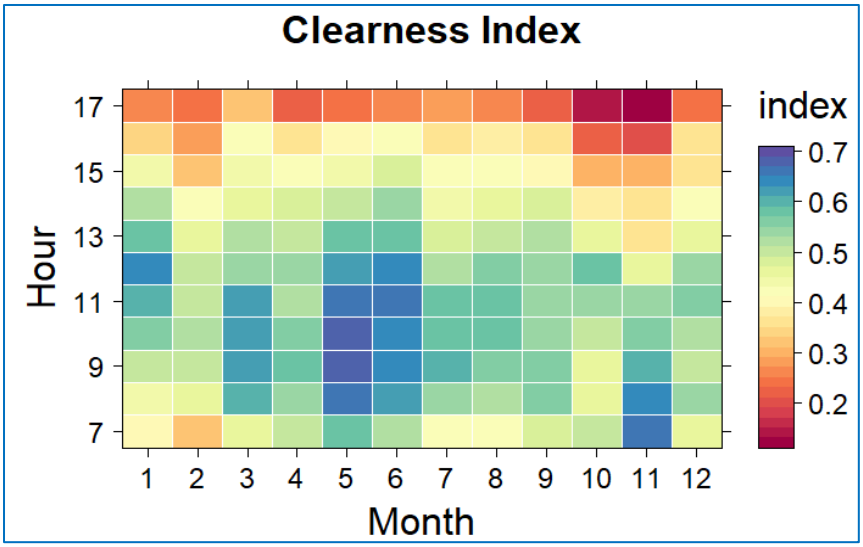

Figure 26. The patterns of daytime and annual clearness index

Sub-diurnal comparisons and the annual pattern of the clearness index in Jembrana-Bali are shown in detail in Figure 26. Analysis of the clearness index of the sky can be used to estimate the amount of direct sunlight that can penetrate windows or building openings. The greater the value of the hourly clearness index indicates clear sky conditions, while the smaller the value of the hourly clearness index indicates the condition of the sky which is covered by many clouds or pollution particles in the atmosphere thereby blocking solar radiation from reaching the surface. In statistical calculations, the hourly average clearness index ranges from 0.12 to 0.68 with an average of 0.47. The highest average clearness index occurs in May with a value of 0.55, while the lowest average clearness index occurs in February with an average value of 0.41. The average clearness index of each other month, namely January is 0.48, March is 0.51, April is 0.47, June is 0.54, July is 0.47, August is 0.47, September is 0.47, October is 0.41, November is 0.43 and December is 0.45.

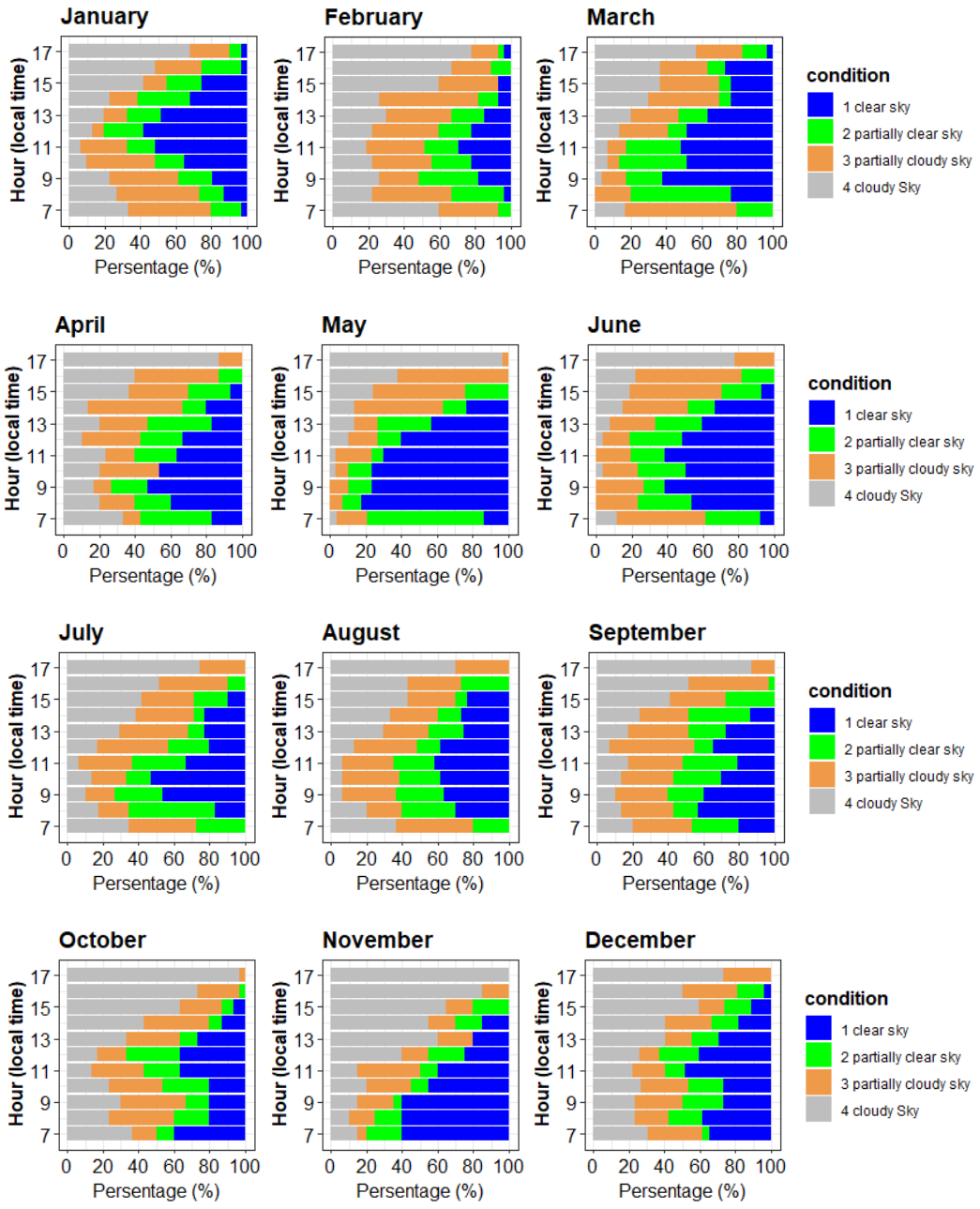

Figure 27. Hourly percentage of different sky conditions in each month

The detailed analysis of the hourly clearness index sub-diurnal which is filtered every hour in different months under different sky conditions at Jembrana-Bali can be seen in detail in Figure 27. Based on daily variations, the percentage of the sky clearness index varies throughout the day. For example, during January at 07.00 LT it was found that 33% had cloudy skies, 47% had partially cloudy skies, 17% had partially clear skies, and 3% had clear skies. Meanwhile at 12.00 LT in January it was found that 13% had cloudy sky, 6% had partially cloudy sky, 23% had partially

clear sky, and 58% had clear sky. The percentage of different sky conditions based on the index clearness filter every hour in all months in detail (see Figure 27) can be considered in the building design, because this can affect the availability of solar heat gain from solar radiation every hour in different months.

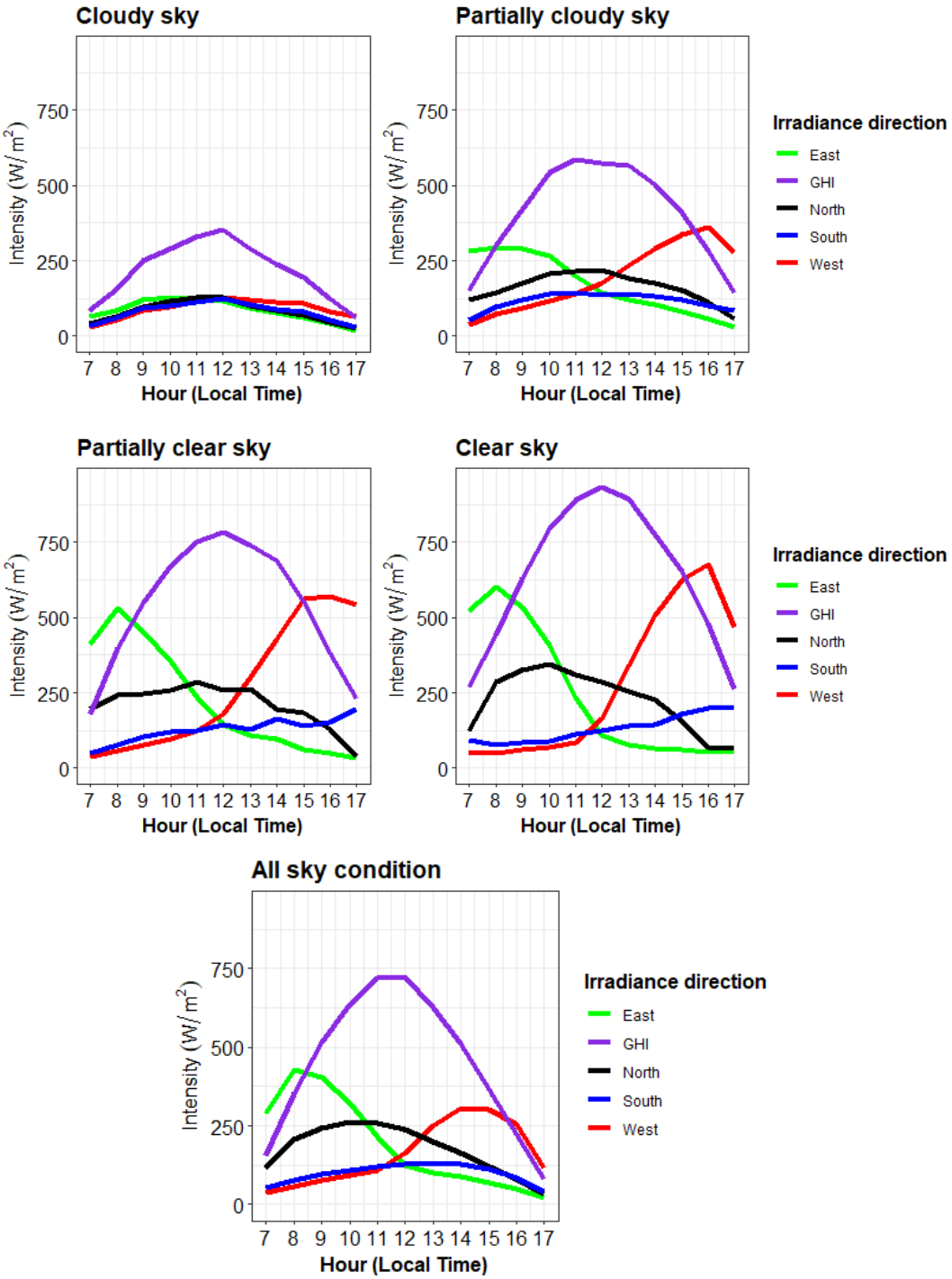

Figure 28. The pattern of solar radiation component fluctuations under different sky conditions

Figure 28. shows a graph of the sub-diurnal time series pattern of the global vertical irradiance component from four different orientations. The time series starts at 07.00 LT to 17.00 LT which is averaged at the same hour under different sky conditions. In all sky conditions it has been found that the global average vertical irradiance from the east is between 21.0 W/m² to 429.2 W/m². West orientation range 53.6 W/m² to 304.3 W/m². North orientation range 31.1 W/m² to 260.3 W/m². South orientation range 42.1 W/m² to 129 W/m². Meanwhile, global horizontal irradiance is in the range of 78.5 W/m² to 723.5 W/m².

In cloudy sky conditions it has been found that the global average vertical irradiance from the east ranges from 18.2 W/m² to 126.6 W/m². West orientation range 29.2 W/m² to 128.1 W/m². North orientation range 24.7 W/m² to 126.4 W/m². South orientation range 27.3 W/m² to 123.7 W/m². Meanwhile, global horizontal irradiance is in the range of 58.8 W/m² to 352.4 W/m². In partially cloudy sky conditions, it has been found that the global average vertical irradiance from the east is between 30.8 W/m² to 291.5 W/m². West orientation range 36.0 W/m² to 360.6 W/m². North orientation range 58.02 W/m² to 217.9 W/m². South orientation range 51.2 W/m² to 142 W/m². Meanwhile, global horizontal irradiance is in the range of 142.5 W/m² to 585.9 W/m².

In partially clear sky conditions, it has been found that the global average vertical irradiance from the east is between 34.0 W/m² to 532.2 W/m². West orientation range 35.31 W/m² to 571.9 W/m². North orientation range 35.9 W/m² to 284.0 W/m². South orientation range 46.74 W/m² to 196.5 W/m². Meanwhile, global horizontal irradiance is in the range of 180.4 W/m² to 782.5 W/m². In clear sky conditions it has been found that the global average vertical irradiance from the east is between 52.4 W/m² to 602.7 W/m². West orientation range 47.48 W/m² to 675.1 W/m². North orientation range 63.8 W/m² to 343.3 W/m². South orientation range 75.5 W/m² to 200.8 W/m². While the global horizontal irradiance is in the range of 260.6 W/m² to 933.7 W/m².

Figure 29 shows the boxplot of each value of the global vertical component range of irradiance at four orientations (combined all hours from 07.00 LT to 17.00 LT) which are filtered under different sky conditions. In cloudy sky conditions it was found that vertical radiation from the west showed the highest intensity with an average value of 84.5 W/m², while the east direction showed the lowest intensity with an average value of 62.6 W/m². In cloudy sky conditions, the average vertical irradiance for the north and south directions is 63.8 W/m² and 65.0 W/m², respectively.

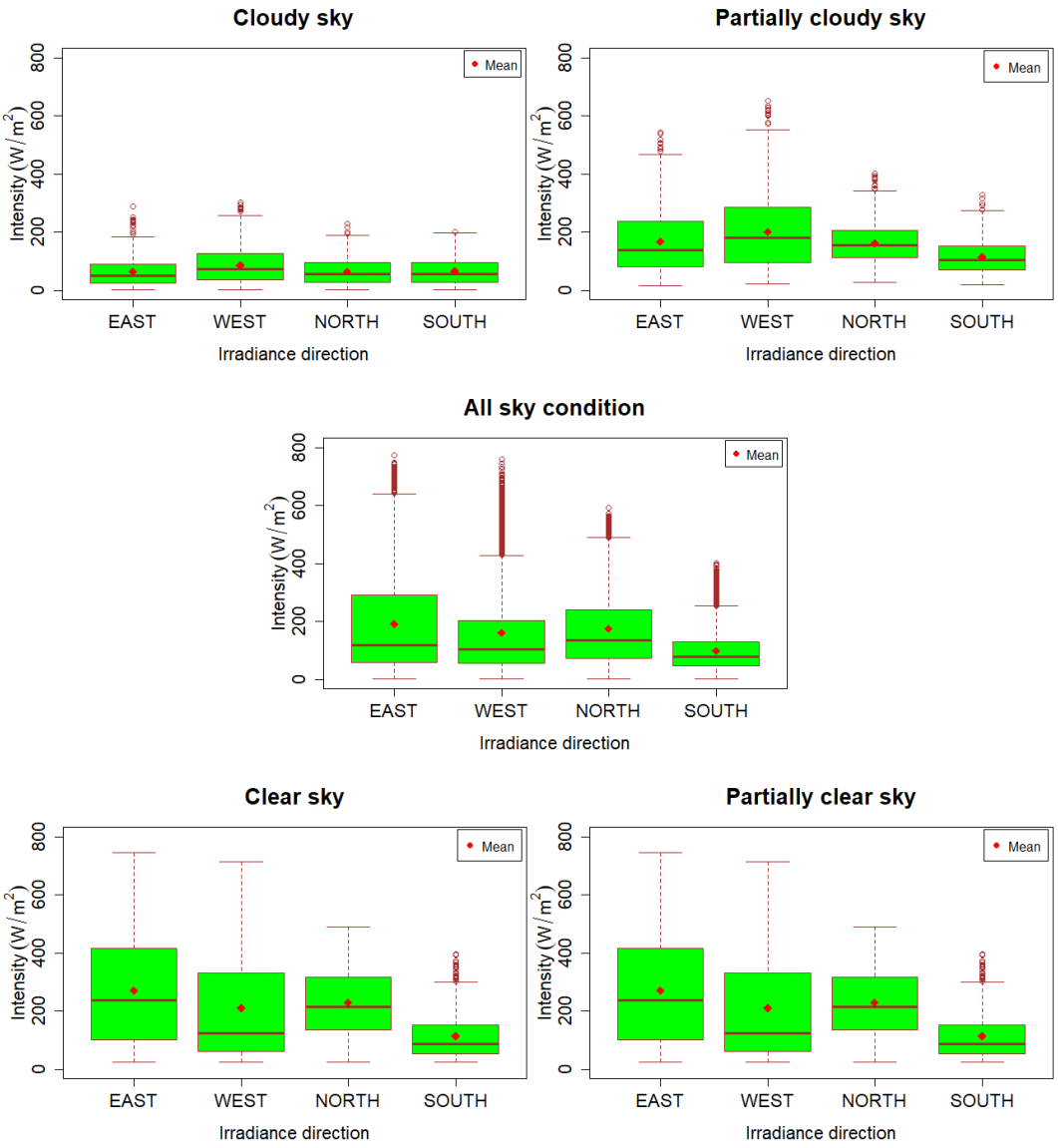

Figure 29. Comparison of the range of each solar radiation component in different sky conditions

In partially cloudy sky conditions, it was found that vertical radiation from the west showed the highest intensity with an average value of 199.9 W/m², while the south direction showed the lowest intensity with an average value of 113.4 W/m². In partially cloudy sky conditions, the average vertical irradiance for the north and east directions is 161.2 W/m² and 167.3 W/m², respectively. In partially clear sky conditions, it was found that vertical radiation from the east showed the highest intensity with an average value of 270.0 W/m², while the south direction showed the lowest intensity with an average value of 114.2 W/m². In partially clear sky conditions, the average vertical irradiance for the west and north directions is 210.6 W/m² and 228.3 W/m²,

respectively. In clear sky conditions it was found that vertical radiation from the east showed the highest intensity with an average value of 309.0 W/m² while the west direction showed the lowest intensity with an average value of 170.2 W/m². In clear sky conditions, the average vertical irradiance for the north and south directions is 279.0 W/m² and 108.9 W/m², respectively. In all sky conditions it was found that the vertical radiation from the east showed the highest intensity with an average value of 190.6 W/m² while the south direction showed the lowest intensity with an average value of 98.1 W/m². In all sky conditions the average vertical irradiance for the west and north directions are 160.1 W/m² and 174.4 W/m² respectively.

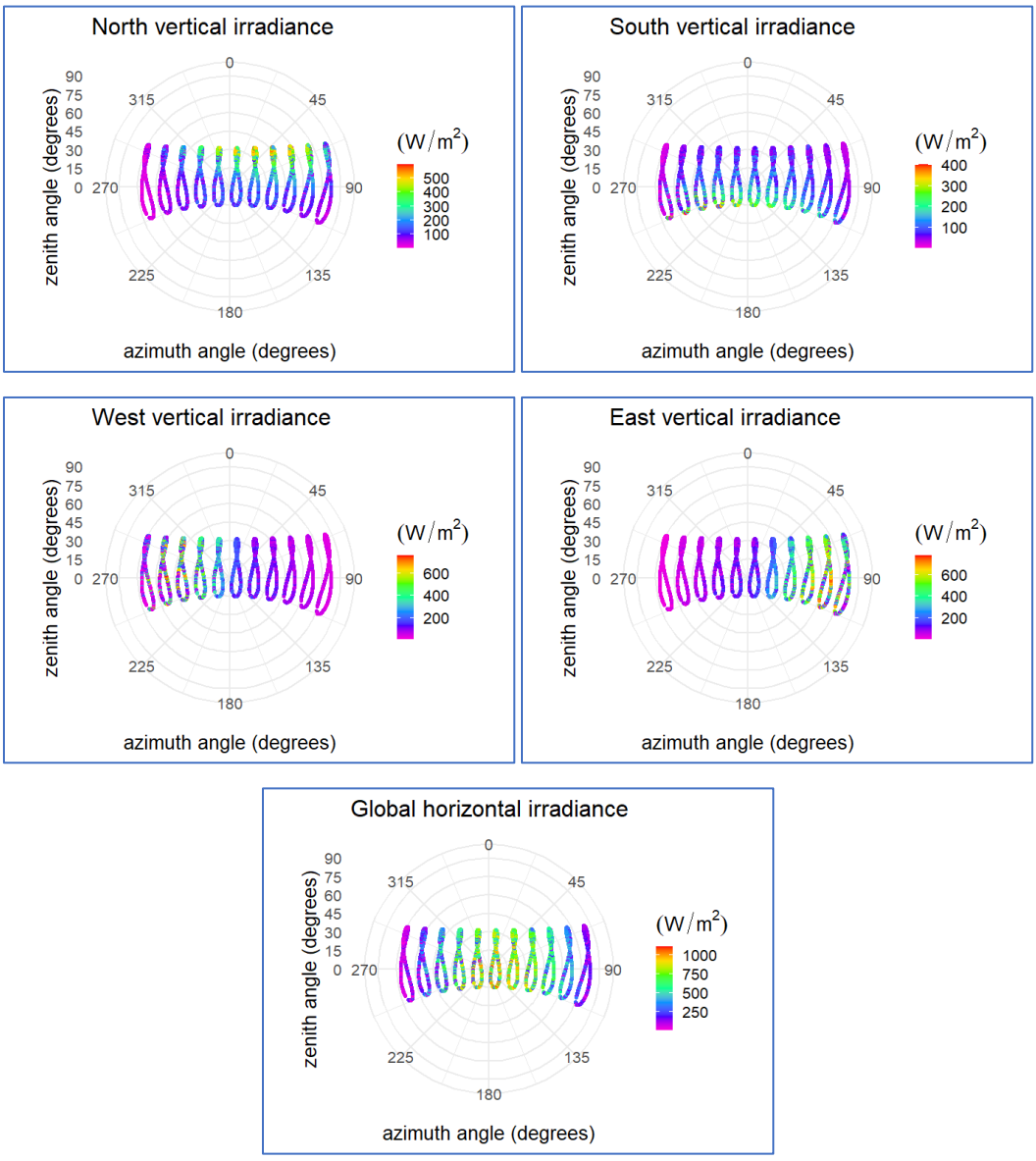

Figure 30. the solar radiation intensity of each component is based on the zenith angle and azimuth angle.

The movement of the sun's position from sunrise to sunset every time produces zenith angles and azimuth angles. The sun path can be used as a basis for determining the orientation of the building, the direction, and the opening model. Figure 30 shows the annual sun-path which is the periodic shift of the sun from south to north and back to south every year in Jembrana-Bali based on the relationship of zenith angle, azimuth angle and global horizontal irradiance, global vertical intensity in the four orientation directions north, east, south, and west. For example, on July 1, 2022, at 07.00 LT, the zenith angle is 85.2 degrees with an azimuth angle of 65.7 degrees while the global horizontal irradiance is 68.1 W/m², global vertical north irradiance is 62.9 W/m², global vertical east irradiance is 83.1 W/m², global vertical west irradiance is 26.2 W/m², global vertical south irradiance is 29.6 W/m².

The value of the intensity of solar radiation on the sun-path changes based on changes in time. Another example is, on July 1, 2022, at 12.00 LT, the zenith angle is 32.0 degrees with an azimuth angle of 11.0 degrees while the global horizontal irradiance is 444.1 W/m², global vertical north irradiance is 211.0 W/m², global vertical east irradiance is 124.1 W/m², global vertical west irradiance is 167.3 W/m², global vertical south irradiance is 124.4 W/m². On June 21, the position of the sun reaches its maximum azimuth to the north while the December 22 solstice reaches its maximum azimuth to the south. Overall based on the analysis of the sun path in Jembrana-Bali it was found that the intensity of the sun is more inclined to come from the north, east and west which can be considered as special treatment on the sides of the building to the north, east and west in the design. This can be used to create shade to minimize excessive solar heat gain.

Chapter 5. The quality control of datasets for TMY calculation input

5.1 Introduction

The building sector has been one of the largest energy consumption sectors in recent decades [131]. In particular, energy for building operations, including heating, ventilation, and air conditioning systems, has contributed to the increase in energy consumption and most likely to climate change [132]. Historical climate observational data have been used for building energy simulations and are widely used to evaluate the thermal performance of buildings. Meteorological data applied to energy simulations should fully represent the local climate to better assess the long-term average performance of buildings. Since the accuracy of building energy predictions is closely related to the reliability of meteorological data as its input, proper selection of meteorological data is a prerequisite for generating valid simulation results.

TMY studies require complete hourly time series data with a minimum 10-year period [133]. The availability of continuous long-term time series data has a significant influence on calculating a TMY. If there are missing data, proper data treatment, such as interpolation, is needed [134]. Many climate observation networks in various parts of the world contain missing data due to various factors, such as damaged observation equipment and data transmission network disruptions. The abovementioned reanalysis data have been corrected for bias to cover missing data [135][136]. For example, solar radiation is one of the major climate variables in the TMY datasets that strongly influences building performance simulations. However, most of the weather stations worldwide, particularly in developing countries, do not have solar radiation sensors due to the highly required investment and the ongoing maintenance costs [137]. Therefore, when observational data are missing, satellite data and reanalysis are usually used to cover solar radiation data. The most widely used global reanalysis datasets include CFS from NOAA [138], MERRA-2 from NASA [139], and ERA5 from ECMWF [63]. Meanwhile, ASHRAE RP-1745 (Roth 2019) studied the use of reanalysis datasets to calculate design climatic conditions and to be the input to building simulation software [140]. The above study found that when reanalysis data were used to calculate design climatic conditions, the obtained results demonstrated a strong correlation with the values derived from the real-time observations. On the other hand, several gap-filling methods for climate data have been developed; for example, Salmani-Dehaghi and Samani [135] developed

bias-correction PERSIANN-CDR models for the simulation and completion of precipitation time series. Meanwhile, Lompar et al. [136] dealt with gaps in the hourly air temperature data using a debiased ERA5 dataset.

5.2 Methodology

5.2.1 Climate data

This study used hourly historical data for eight climate elements, including global horizontal irradiance, direct normal irradiance, diffuse horizontal irradiance, air temperature, precipitation, wind speed, relative humidity, and dew point temperature. Climate observation data of temperature, relative humidity, and wind speed were acquired from the 106 meteorological stations (sites) of the Indonesian Agency for Meteorology Climatology and Geophysics (BMKG) for the period of January 2011 to December 2020. Time series of global horizontal irradiance, direct normal irradiance, and precipitation data for the corresponding 10-year period were extracted from ERA5 reanalysis data [63] after adjusting to the coordinates of 106 sites in each climate zone due to the unavailability of the observation data. The new climate zones for determining appropriate passive cooling techniques in Indonesia and classified the entire Indonesian territory into eight climate zones from chapter 2 this thesis, which were subsequently used in this study. The values of diffuse horizontal irradiance and dew point temperature were obtained through calculations that involved other climate elements. They were calculated using equations (7) [141] and (8) [142], respectively:

$$\mathrm{DHI} = \mathrm{GHI} - \mathrm{DNI} \times \cos(\theta z) \quad \text{(Eq. 7)}$$

$$\mathrm{Td} = \left(\frac{\mathrm{RH}}{100}\right)^{\frac{1}{8}} \times \left(112 + (0.9 \times \mathrm{T})\right) - 112 + (0.1 \times \mathrm{T}) \quad \text{(Eq. 8)}$$

where DHI is the diffuse horizontal irradiance (W/m^2), GHI is the global horizontal irradiance (W/m^2), DNI is the direct normal irradiance (W/m^2), θz is the solar zenith angle (°), Td is the dew point temperature (°C), RH is the relative humidity (%) and T is temperature (°C). Since the TMY calculation requires a complete time series without a single missing value, the hourly time series of temperature, relative humidity, and wind speed data were also extracted from ERA5 reanalysis data with bias correction processes to fill the gaps in the observational data, as described in the following section.

5.2.2 Filling the observational gaps

Missing observational data is a common problem in long-term datasets in many climatic

observation networks. Meanwhile, the TMY calculation requires a complete weather dataset with an hourly time series. Therefore, it is necessary to fill in the gaps and replace the missing observational data as the quality control of datasets. The gap-filling technique for the temperature parameter [136] and the other parameters [143] is based on ERA5 reanalysis data. To evaluate the distribution performance of the ERA5 reanalysis data at each site, the correlation and bias between the ERA5 reanalysis data and the observational data were calculated. Equations (9) and (10) were used to calculate the correlation coefficient (r) [144] and bias [145], respectively.

$$r = \frac{\sum_{i=1}^{n}(O_i-\bar{O})(M_i-\bar{M})}{\sqrt{\sum_{i=1}^{n}(O_i-\bar{O})^2}\sqrt{\sum_{i=1}^{n}(M_i-\bar{M})^2}} \quad \text{(Eq. 9)}$$

$$\text{bias} = \frac{1}{n}\sum_{i=1}^{n}(M_i - O_i) \quad \text{(Eq. 10)}$$

where O is the actual value (observational data), and M is the estimated value (ERA5 reanalysis data). The gap-filling technique was developed based on debiasing using the bias correction method with quantile mapping from ERA5 reanalysis data, which are calculated using equation (11) [146]:

$$\hat{x}_{m,p}(t) = F_{o,h}^{-1}\{F_{m,h}[x_{m,p}(t)]\} \quad \text{(Eq. 11)}$$

The quantile mapping equates the CDFs $F_{o,h}$ and $F_{m,h}$ of the observed data $x_{o,h}$, denoted by subscript o, and ERA5 reanalysis data $x_{m,h}$, denoted by subscript m, in a length period of observation, denoted by subscript h. For bias-correction $x_{m,p}(t)$, ERA5 reanalysis data at time t in some prediction period, are denoted by the subscript p. The quantile mapping is equivalent to a lookup table whose entries are found by interpolating between points in a quantile plot of the length period of observational data. The transfer function was constructed exclusively using information from observation length periods [146].

5.3 Result and discussion

5.3.1 Distribution of missing observation data

The distribution of hourly missing data for temperature, relative humidity, and wind speed at 106 sites across Indonesia in from January 2011 to December 2020 is shown in Figure 31. For a complete time series of 10-year data starting in January 2011 at 00:00 local time until December 2020 at 23:00 local time, the total observational data comprise 87672 data. All sites have missing data with a percentage that varies between 29.96 and 50.19 %. For example, a station in Kota Pontianak with station ID 96585 has 44.5 % missing temperature data with a total hourly missing value of 39042 data. Out of the 106 sites, the distribution of missing temperature data ranges from 29.96 % to 47.65 %, with the highest percentage being 31 % at 32 sites. The distribution of missing RH data ranges from 29.97 % to 47.65 %, with the highest percentage of 31 % at 34 sites. Finally, the distribution of missing wind speed data ranges from 29.96 % to 50.19 %, with the highest percentage of 31 % at 34 sites.

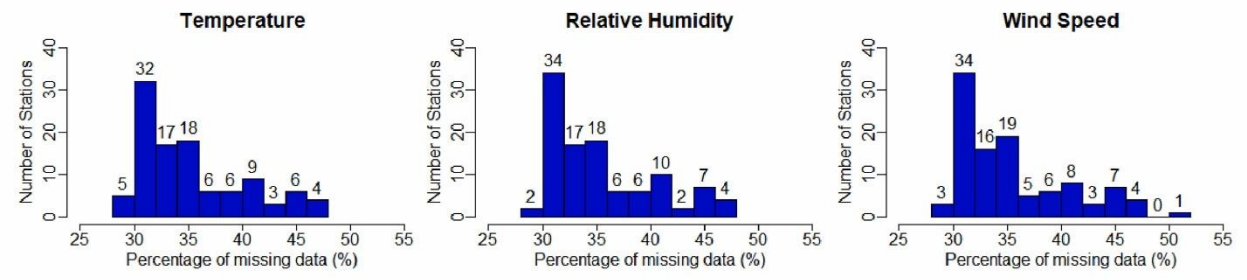

Figure 31. The distribution of missing hourly observational data

5.3.2 Correlation and bias of ERA5 reanalysis data

The correlation and bias results of the ERA5 hourly time series, derived from the number of pairs of hourly time series data obtained during 2011-2020 are shown in Figure 32. Correlation and bias values were calculated for temperature, relative humidity, and wind speed data between ERA5 reanalysis data and the observational data, which were spatially visualized by plotting them according to the respective site coordinates. Among the three climate elements observed at 106 sites throughout Indonesia, the observed temperature and temperature data from ERA5 have the greatest correlation compared to those for relative humidity and wind speed. The highest temperature correlation with an r-value of 0.7 or above is mainly observed on large islands, such

as Sumatra, Kalimantan, Jawa, Sulawesi, and Papua. Moreover, sites that are located close to coastlines, such as those in the Maluku Islands, have a relatively lower distribution of the temperature correlation. While spatially, the distribution of ERA5 temperature bias ranges from −4.5 °C to 2.7 °C. The bias for relative humidity was −6 % to 10 % and the bias for wind speed was −4 m/s to 2 m/s.

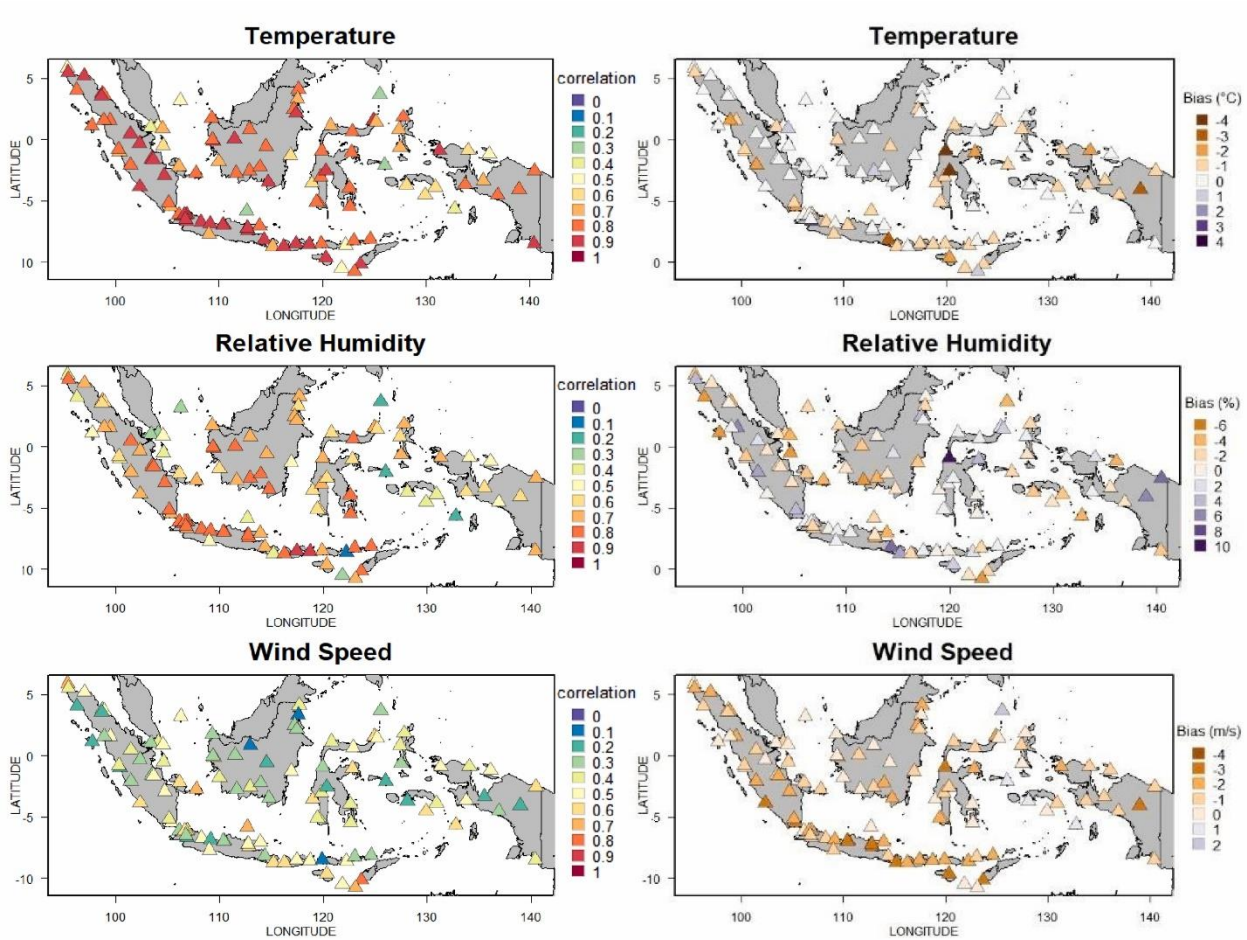

Figure 32. Spatial distribution of ERA5's correlation and bias

5.3.3 Filling observation gaps

The ERA5 reanalysis dataset for temperature, relative humidity, and wind speed was extracted at all site coordinates and then corrected by a bias-correction method using quantile mapping. In the interest of being concise, we plotted the temperature time series at one station, Pontianak Meteorological Station in Kota Pontianak with station ID 96585 (Figure 33(a-f)), to clearly illustrate the process of filling the missing temperature data using bias-corrected ERA5

reanalysis data. The blue line in Figure 33a shows the time series of observational data for 10 years, including missing observational data. Based on the comparison, Figure 33b shows that the ERA5 temperature data are always lower than the observed temperature. Figure 33c shows the distribution of the CDF of ERA5 temperature before bias correction and the bias-corrected ERA5 temperature (ERA5 temperature debias). Quantile mapping can improve the distribution of ERA5 temperature values to be close to the distribution of the observed temperature values. Figure 33d shows the mean, first quartile, median, and third quartile of ERA5 temperature, which have been corrected for bias to be close to the observed mean, first quartile, median, and third quartile temperature values. The comparison of ERA5 temperature values before and after bias correction is shown in Figure 33e. The range of diurnal ERA5-debias temperature has increased, according to the results of ERA5 temperature bias adjustment. In Figure 33f, the green line shows the results of filled-in observational data using ERA5 temperature debias. The same procedure was employed to fill in the missing observational data of temperature, relative humidity, and wind speed at 106 sites in Indonesia.

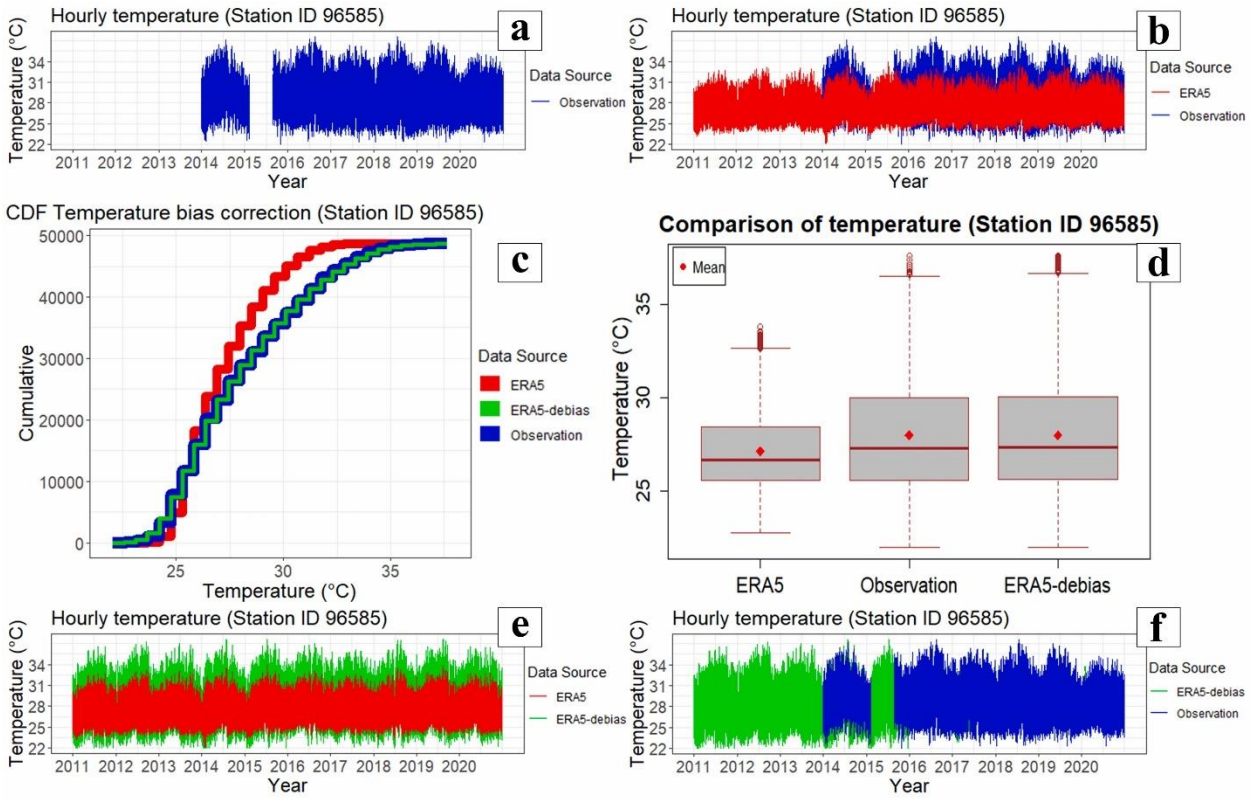

Figure 33. An example of the ERA5 bias-correction process and filled gaps in the observational data

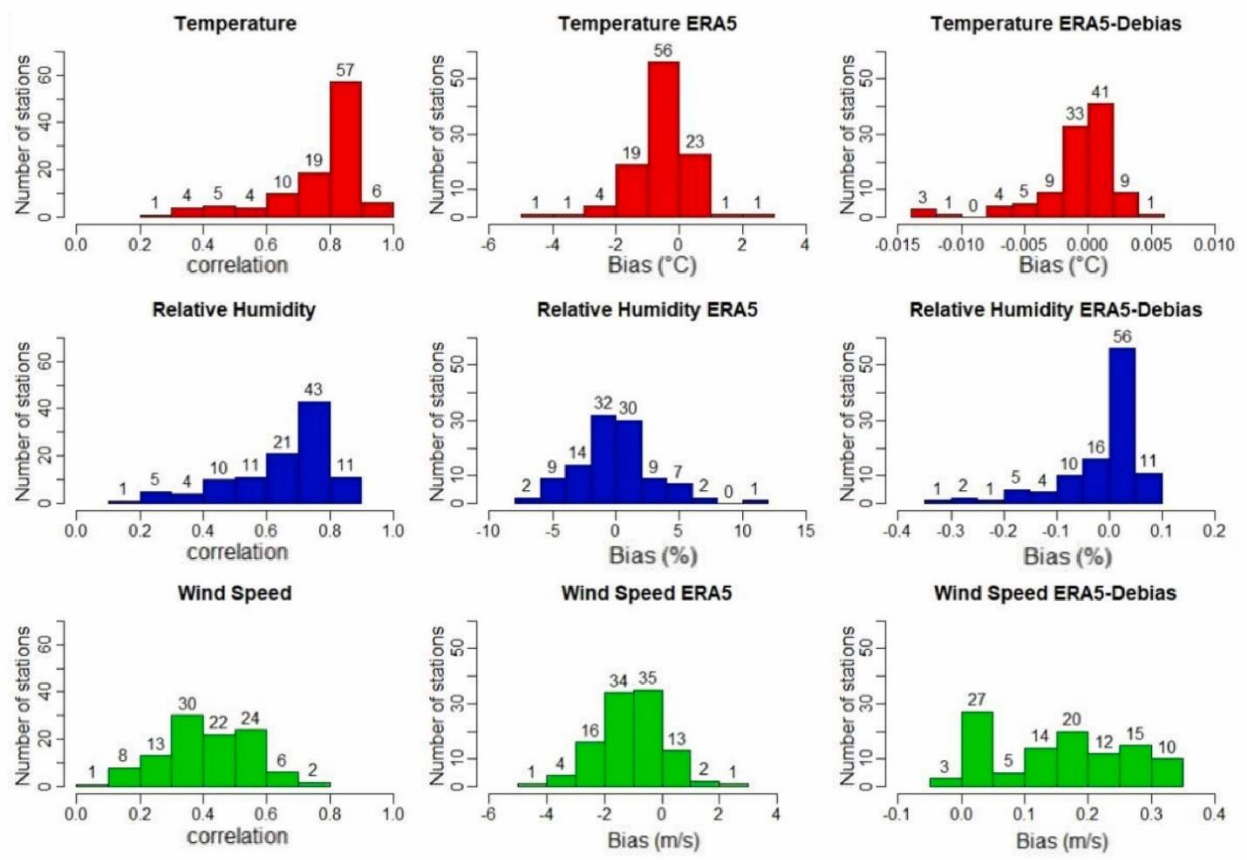

Figure 34. The distribution of ERA5 correlation, ERA5 bias, and ERA5-debias

The distributions of ERA5 correlation, ERA5 bias, and ERA5-debias across all sites is shown in Figure 34. It was found that the developed bias-correction model increased the accuracy of the ERA5 reanalysis data. The performance of the ERA5 reanalysis data was assessed based on the availability of hourly time series observational data for 2011-2020. The correlation between the observed temperature and ERA5 temperature ranges from 0.28 to 0.92, with the highest number of sites having a correlation of 0.83. The correlation between the observed RH and ERA5 RH ranges from 0.13 to 0.86, with the highest number of sites having a correlation of 0.70. The correlation between the observed wind speed and ERA5 wind speed ranges from 0.06 to 0.76, with the highest number of sites having a correlation of 0.40. After applying the bias-correction method, the bias distributions of ERA5 temperature, relative humidity, and wind speed at all sites were reduced. Initially, the temperature distribution ranged from -4.5°C to 2.7°C, with the largest distribution being -0.4°C, then it was reduced to a narrower range of -0.014°C to 0.005°C. Similarly, the initial distribution of relative humidity bias for ERA5 at all sites was -6% to 10%,

with the largest distribution of -0.2%, then it was minimized to -0.32% to 0.07%. The distribution of the wind speed bias for ERA5 at all sites, initially ranging from -4 m/s to 2 m/s with the largest distribution being -1 m/s, was also reduced to -0.02 m/s to 0.35 m/s. After filling in the missing observational data with ERA5-debias data, the hourly time series data were completed and can be used for the calculation of TMY at 106 sites in Indonesia.

Chapter 6. Development of TMYs and their verification

6.1 Introduction

Improvement of building energy efficiency is increasingly needed due to climate change concerns [147]. Evaluation and optimization of a building's energy efficiency and overall performance can be achieved using building performance simulation software (e.g., EnergyPlus, DOE2, TRNSYS) and computer programs [148][149]. Usually, information regarding construction, occupancy patterns, heating, ventilation, and air conditioning (HVAC), and boundary conditions such as climate information is included in building performance simulations [150]. One of the key factors that influences the accuracy of building performance simulation is the reliability of outdoor meteorological data as input [151][152][153]. Thus, the selection of appropriate meteorological data is a prerequisite for producing valid simulation results [154][155][156].

Generally, there are three types of hourly weather data used in building energy simulations [157], namely, multiyear weather datasets [158], typical meteorological year (TMY) [159], and representative days [160]. A comparison of multiyear weather datasets and TMYs has been studied in Poland [161] and China [162], which suggests that adopting multiyear weather datasets is sometimes uneconomical for general building energy design. Meanwhile, the representative days are often too limited and insufficiently detailed for design issues. Yang et al. [162] carried out detailed hourly energy simulations for office buildings in five major climate zones in China using multiyear weather datasets and TMY. The results suggested that the predicted monthly load and energy consumption profiles from TMY tend to follow long-term averages closely. TMY can reduce the complicated computational effort in simulating and handling weather data using a one-year dataset [163]. Additionally, a consistent weather data format can be ensured in the case of TMY so that results from different studies can be compared [164]. Therefore, TMY is the most commonly used to date for detailing building energy analysis [151][152][153].

The TMY consisted of 12 typical meteorological months (TMMs) from different years (January through December) and it was first introduced by Hall et al. from Sandia National Laboratories in 1978 [159]. Their work shows that TMY is very useful in various applications because it represents the climate condition in an area. The data were generated using an objective statistical algorithm to select the most typical month from long-term records and to represent a

typical or “median” year with respect to weather-induced energy loads on buildings. The National Renewable Energy Laboratory developed a second version (TMY2) in 1995 [165]. Habte et al. [166] developed the TMY for the US and other locations in 2014, containing solar radiation and other climate elements in grid data format. Furthermore, solar radiation data were derived from satellite observations, and environmental data were derived from MERRA2 reanalysis datasets [139] and from the large climate forecasting model NSRDB [167]. TMY third version (TMY3) [168] was also developed with a slight modification to the month-specific selection process. the ASHRAE International Weather for Energy Calculations (IWEC2) datasets [169] contain annual weather data for 3012 international locations developed via ASHRAE RP-1477, which uses the same weather data source [170], while the test reference year (TRY) was developed by ISO 15927-4 (European Committee for Standardization)[171]. Most of the other studies cited above used a modified version of Hall et al.’s work to generate TMY. The modification of Hall et al. 1978 is an empirical approach that selects individual months from different recorded years [172].

While several building energy simulation programs are equipped with weather datasets or offer access to open-source weather databases, the accuracy of the latter remains questionable. However, many countries have created and modified their own TMY. Based on several methods that have been proposed by several previous researchers, the difference lies in the choice of climate parameters used, the weighting of the climate parameters, the length of the data period, the type of data (observation, satellite, and reanalysis) and the purpose of making TMY. Determining weighting criteria to generate TMY, which is also referred to as the TRY, using the FS statistics method has been done in various cities and countries. The examples include those in Vietnam [173], Libya [174], Greece [175], Cyprus [176][177], Syria [178], Turkey [179][180], China [181][182], Hong Kong [183][184], Nigeria [185][186], Togo of West Africa [187], Argentina [188], Iran [189], Spain [190], and Saudi Arabia [191]. On the other hand, TRY has been studied in Malaysia [192], Italy [157], Finland [154], South Korea [155][156], and Portugal [193]. Most of the above studies involved comprehensive meteorological elements, but several studies constructed TMYs using specific elements. For example, a TMY with only solar radiation parameters has been created in Boston, USA [194], Egypt [195], and China [133]. Moreover, a TMY incorporating sunshine duration has been created in Turkey [196], France [197], Greece [198], and Oman [199], while a TMY utilizing the diffuse fraction model was created in Taiwan [200].

There are other methods of determining a TMY. Due to differences in the sources of meteorological data and the mathematical methods used in the selection process, various methods for generating a TMY have been proposed and reported in several countries and cities. For example, Andersen et al. [201] and Lund and Eidorff [202] converted meteorological parameters into residuals and then analyzed the residuals to create statistical indicators to select TMMs, which are the TMY components. Festa and Ratto [203] standardized variables and correlations of subsequent daily values in choosing TMMs. Zhang [204] developed the Chinese Typical Year Weather (CTYW), which is a typical meteorological database for Chinese locations. Song et al. [205] proposed a method named the Chinese Standard Weather Database (CSWD) to examine the thermal environment in China. Chan [163] generated TMYs using genetic algorithms for different energy systems. Li et al. [206] generated a new TMY based on entropy-based Technique for Order Preference by Similarity to Ideal Solution (TOPSIS) theory for different climatic zones in China. Arima et al. [207] carried out a typical and designed weather year using bias correction for building energy simulation in Japan. Fan et al. [208][152] created a TMY based on ensemble empirical mode decomposition (EEMD) for different climates in China. Yuan et al. [153] calibrated TMY weather files in the system design of zero-energy buildings for performance improvements in Hong Kong.

The methods mentioned above generally have different procedures for selecting TMMs because there is no universal procedure or criteria [183][187]. The basic principle is to select all monthly meteorological parameters that have the closest values to the long-term distributions. For example, Bilbao et al. [209] used three different methodologies measured in two cities, Madrid and Valladolid (Spain), to generate a TRY. The results show that the most appropriate method for generating a TRY depends on the characteristics of the stations, which vary from month to month. Sorrentino et al. [210] compared three statistical methods of TMY generation to approximate the energy consumption of a simple building and the energy produced by a photovoltaic system in Palermo, Italy. They found that all TMY methods were suitable for the design of photovoltaic systems. Several other researchers have also compared various methods. Fernández et al. [211] found the Argiriou method to be the best for greenhouse and outdoor conditions on the Mediterranean coast. Argiriou et al. [212] showed that the TMY, which aligned the closest to the average system performance, was the modified Festa-Ratto method for Athens, Greece. Li et al. [213] found that the TMY selected by the Sandia method exhibited the closest value with the

average simulated energy consumption from year to year in Beijing, while the CTYW method used in Harbin, Urumqi, Chengdu, Wuhan, and Guangzhou had the closest value to the simulated average energy consumption from year to year. Skeiker [214] showed that the TMY performing the closest to the average performance of the building thermal system at the Damascus and Kharabo sites was generated using the modified Sandia method. Janjai and Deeya [215] investigated the performance of the Sadia, Danish, and Festa-Ratto methods for generating TMY data at four stations in the tropical environment of Thailand. For all TMY parameters, the statistical tests showed that there was no significant difference between the 10-year mean values of the parameters and the corresponding mean values of TMY generated from each method. Due to its simplicity and the numerous widely tested studies about it, the Sandia method with modified weighting criteria of FS statistics is recommended for TMY generation [215], which is also adopted in this study.

Regardless of the method used, a TMY can be adapted for various applications [216], including building performance/energy simulation [217][218][219][220], renewable energy for photovoltaic application systems [221][222][223][224][225][187][226][227][228], strategic planning of ventilation systems [229], passive cooling/building designs/strategies [230][231][232], heating and cooling degree-hour values [233] and heating load and cooling load [188]. Sun et al. [234] selected energy simulation of buildings with daylight utilization using a TMY. Chai et al. [235] used TMY data to investigate the impact of climate change on the life-cycle performance of net-zero-energy development in China's unique climate region. Wang et al. [236] used TMY data for Hong Kong climate-based daylight calculations. In another study, Ye et al. [237] used a TMY to determine the range of phase changes to achieve optimal PCM thermal control effects.

6.2 Methodology

6.2.1 Analysis process

The development of TMYs in this study was undertaken in three sequential stages, namely, quality control of datasets, TMYs calculation, and TMYs verification (see Figure 35). In the quality control stage, the distribution of missing data was checked. Each site has different numbers of missing values for temperature, relative humidity, and wind speed, which can be filled in using the corrected ERA5 reanalysis data. This process resulted in complete hourly time series data,

which then became the input for the TMY calculation. Then, each climate element was used to select 12 TMMs based on FS statistics with a minimum weighted sum in the TMY calculation. In general, the cumulative distribution function (CDF) of the selected TMMs is expected to align with their long-term distributions. Following the generation of the TMYs, the subsequent step involves comparing the TMY data with LT data and multiple-year data. For the TMY verification stage, several statistical methods were employed, including correlation, RMSE, MAE, and MSE at each site. Finally, TMYs were plotted monthly based on average daily climate values to identify the seasonal and annual TMY patterns and to compare TMYs among the eight climate zones in Indonesia. Information obtained from this process was then used to determine the general pattern of TMYs in different climate zones, which can represent their long-term climate conditions.

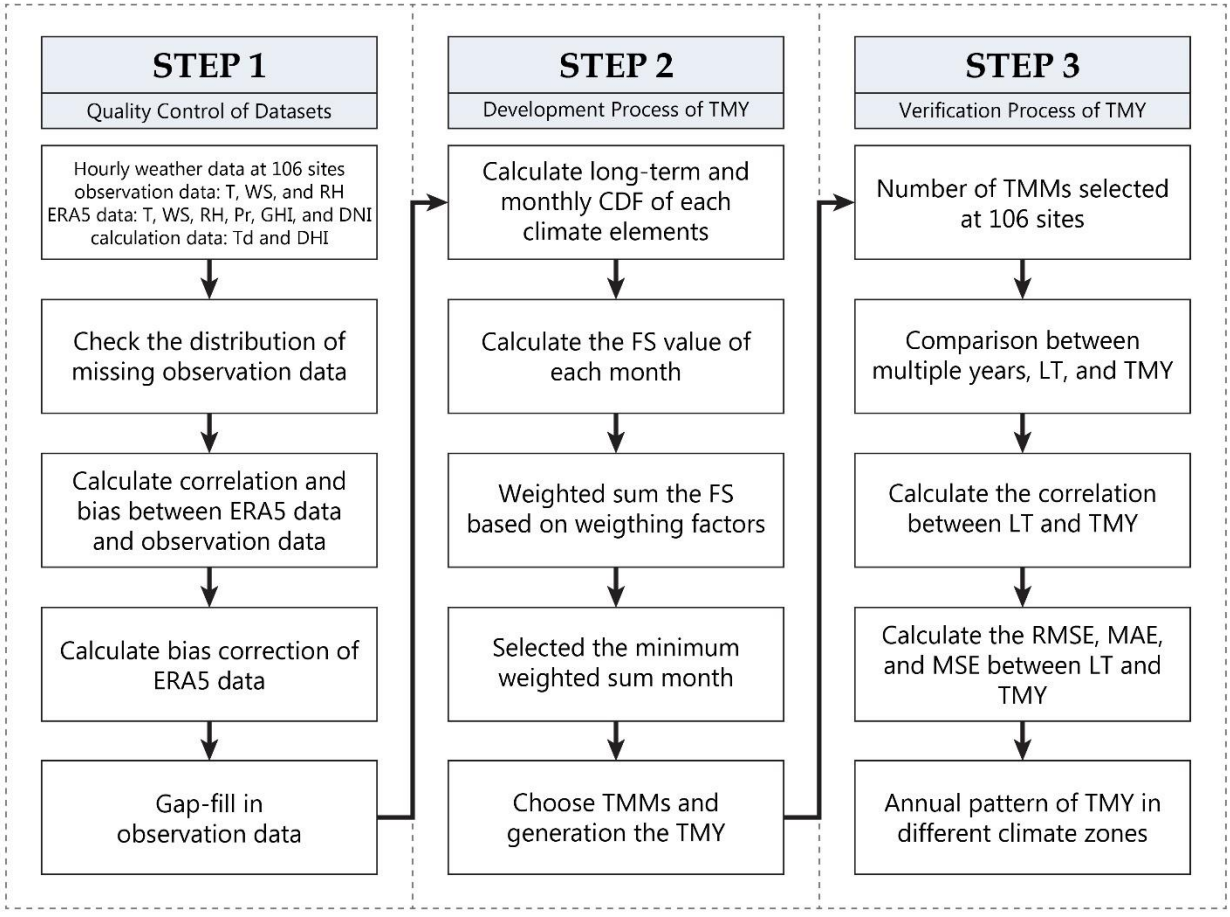

Figure 35. Analysis flow of this study

6.2.2 Calculation of the typical meteorological years

The TMYs calculation in this study used the Sandia method with modifications in the weighted factor for each climate element. The Sandia method, an empirical approach, involves selecting specific months of the year that differ from the recorded period. For instance, in a case where a time series containing 10 years of data, specifically for the same month of January (January 2011, January 2012, …, to January 2020), is examined. The most representative month is selected as January TMM. Then, this process is repeated for the other months to complete one TMM year. In selecting TMM, the monthly CDF that has the closest values to the long-term CDF is chosen. Monthly CDF candidates were compared to the long-term CDF using the following FS equation [238] for each daily climate element (see equation 12)[185].

$$FS_j = \left(\frac{1}{n}\right) \sum_{i=1}^{n} \delta_i \qquad \text{(Eq. 12)}$$

where δ_i is the absolute difference between the long-term CDF and the yearly CDF for day i in the month, n is the number of daily readings in that month, and j is the climate element considered. The weighted sum of the FS statistic was used to select the candidate months that had the lowest weighted sum (see equation 13) [185]. Because some climate elements were judged to be relatively more important than others, the weighting factor set for daily global horizontal irradiance was 0.25, for daily mean temperature was 0.15, and for daily mean dew point was 0.1, whereas daily maximum wind speed, daily mean wind speed, daily maximum temperature, daily minimum temperature, daily maximum dew point temperature, and daily minimum dew point temperature were set with the same weighting factor of 0.05. Additionally, since the other outdoor climatic variables, including temperature, were significantly influenced by solar radiation, the variation in solar radiation will influence interior air-conditioning loads, indoor passive or active heating systems, and the external thermal environment either directly (through solar radiation) or indirectly (through temperature) [185][220].

$$\text{weighted sum} = \sum_{j=1}^{n} W_j \, FS_j \qquad \text{(Eq. 13)}$$

where n is the number of climate elements considered. W_j is the weight for climate element j, and FS_j is the FS statistic for climate element j. The same months from different years were ranked in ascending order from the smallest to the highest weighted sum values. The year that has the smallest weighted sum value in the FS statistics of all daily climate elements was chosen as the TMM [163][180][188]. Then, the chosen TMM for each month from January to December (12 TMMs) were merged together to form the TMY, representing a complete year [189]. In this study, this procedure was carried out at 106 observational sites spreading across eight different climate zones. For verification purposes, the generated TMYs were compared to the long-term averages using several statistical methods, namely, correlations, RMSE, MAE, and MSE, which were calculated using equation (9) [144], and equations (14, 15, 16) [239].

$$\mathrm{RMSE} = \sqrt{\frac{1}{n}\sum_{i=1}^{n}(O_i - M_i)^2} \qquad \text{(Eq. 14)}$$

$$\mathrm{MAE} = \frac{1}{n}\sum_{i=1}^{n}|O_i - M_i| \qquad \text{(Eq. 15)}$$

$$\mathrm{MSE} = \frac{1}{n}\sum_{i=1}^{n}(O_i - M_i)^2 \qquad \text{(Eq. 16)}$$

where O is the actual value (long-term average data), M is the estimated value (TMY generation data), and n is the number of instances.

6.3 Result and discussion

6.3.1 Generation of typical meteorological years

In this section, the resulting TMYs with 12 TMMs at 106 sites are further discussed. It can be inferred that the TMMs, results of TMYs generation, vary significantly, despite the sites being in the same climate zone. It was found that local climate conditions have a major influence on the

resulting TMMs. For instance, the selected TMMs for station ID 96009 located in Kab. Aceh utara and included in climate zone 1A (equatorial) (See Table 9. No. 1) are January 2013, February 2018, March 2018, April 2018, May 2014, June 2019, July 2018, August 2015, September 2018, October 2012, November 2017, and December 2016. More TMMs were discovered in 2018, namely, February, March, April July, and September. Meanwhile, in another location, Kab. Nagan Raya (See Table 9. No. 2), whose location is different but still in the same climate zone 1A (equatorial), the resulting TMMs were different. The composition of TMY from January to December in the selected years was 2013, 2017, 2019, 2017, 2014, 2014, 2016, 2011, 2014, 2020, 2018 and 2018. Additionally, it was discovered that 2014 contributed the most to the TMY composition, specifically the months of May, June, and September.

Another example is Station ID 96973, in Kab. Sumenep, which falls under climate zone 4B (sub-savanna) (See Table 9. No. 106). The TMY generation process reveals that the selected TMMs correspond to the following years in chronological order from January to December: 2019, 2019, 2017, 2019, 2017, 2020, 2015, 2013, 2018, 2012, 2020, and 2018. It was found that 2019 gave more TMM with a total of four months, namely, January, February, and March. More detailed information about TMYs generation at 106 sites in Indonesia is provided in Table 9.

Table 9. Summary of the selected TMYs for 106 sites in Indonesia

No	Station ID	CLIMATE ZONES	REGENCY/CITY	JAN	FEB	MAR	APR	MAY	JUN	JUL	AUG	SEP	OCT	NOV	DEC
1	96009	1A	Kab. Aceh Utara	2013	2018	2018	2018	2014	2019	2018	2015	2018	2012	2017	2016
2	96015	1A	Kab. Nagan Raya	2013	2017	2019	2017	2014	2014	2016	2011	2014	2020	2018	2018
3	96033	1A	Kota Medan	2013	2018	2013	2013	2014	2015	2018	2015	2012	2011	2018	2011
4	96041	1A	Kota Medan	2012	2016	2018	2013	2017	2013	2015	2015	2012	2011	2015	2017
5	96073	1A	Kab. Tapanuli Tengah	2012	2018	2019	2020	2015	2017	2016	2019	2020	2014	2018	2020
6	96075	1A	Kab. Nias	2015	2019	2018	2013	2015	2018	2014	2017	2017	2014	2018	2018
7	96109	1A	Kota Pekanbaru	2013	2017	2012	2019	2015	2017	2016	2018	2018	2014	2014	2018
8	96161	1A	Kota Padang	2013	2015	2015	2013	2015	2012	2016	2015	2014	2014	2015	2014
9	96163	1A	Kab. Padang Pariaman	2013	2018	2019	2018	2015	2014	2016	2018	2014	2014	2018	2015
10	96171	1A	Kab. Indragiri Hulu	2018	2017	2012	2018	2017	2016	2018	2018	2011	2014	2018	2017
11	96191	1A	Kab. Muaro Jambi	2018	2017	2012	2018	2017	2016	2017	2017	2018	2018	2018	2017
12	96195	1A	Kota Jambi	2019	2017	2012	2017	2017	2017	2017	2020	2018	2020	2014	2017
13	96221	1A	Kota Palembang	2017	2020	2019	2020	2019	2017	2014	2020	2018	2018	2020	2017
14	96503	1A	Kab. Nunukan	2017	2018	2018	2017	2018	2015	2017	2015	2015	2018	2017	2017
15	96509	1A	Kota Tarakan	2019	2015	2018	2017	2017	2014	2018	2016	2015	2019	2018	2018
16	96525	1A	Kab. Bulungan	2017	2018	2018	2017	2015	2014	2017	2016	2014	2018	2018	2016
17	96529	1A	Kab. Berau	2018	2018	2018	2014	2018	2014	2014	2011	2014	2018	2015	2011

18	96535	1A	Kab. Sambas	2013	2018	2018	2019	2017	2018	2017	2015	2014	2015	2015	2016
19	96559	1A	Kab. Sintang	2018	2018	2017	2015	2015	2016	2017	2011	2011	2017	2017	2016
20	96565	1A	Kab. Kapuas Hulu	2013	2020	2014	2013	2014	2011	2016	2013	2018	2017	2011	2011
21	96581	1A	Kab. Kubu Raya	2019	2015	2014	2015	2015	2015	2017	2015	2014	2017	2018	2014
22	96585	1A	Kota Pontianak	2012	2017	2017	2018	2015	2015	2017	2012	2018	2020	2016	2016
23	96595	1A	Kab. Barito Utara	2019	2013	2015	2015	2018	2016	2018	2019	2012	2018	2014	2020
24	96615	1A	Kab. Ketapang	2018	2017	2019	2014	2015	2017	2017	2014	2018	2018	2014	2016
25	96633	1A	Kota Balikpapan	2018	2017	2019	2017	2011	2018	2019	2018	2018	2017	2020	2018
26	96645	1A	Kab. Kotawaringin Barat	2013	2015	2017	2017	2015	2015	2018	2018	2013	2012	2020	2016
27	96651	1A	Kab. Kotawaringin Timur	2015	2019	2014	2015	2014	2016	2018	2014	2018	2019	2018	2014
28	96655	1A	Kota Palangkaraya	2017	2019	2015	2014	2015	2015	2017	2018	2011	2019	2020	2014
29	96737	1A	Kota Serang	2017	2017	2018	2019	2014	2018	2014	2018	2018	2013	2020	2017
30	96739	1A	Kab. Tangerang	2017	2013	2018	2018	2018	2018	2018	2018	2018	2011	2014	2014
31	97016	1A	Kota Bitung	2019	2020	2017	2019	2017	2015	2019	2011	2013	2018	2018	2020
32	97028	1A	Kab. Toli Toli	2017	2018	2013	2017	2014	2015	2017	2011	2012	2013	2011	2016
33	97086	1A	Kab. Banggai	2017	2017	2013	2013	2019	2014	2017	2014	2013	2013	2020	2016
34	97126	1A	Kab. Luwu Utara	2015	2019	2015	2017	2018	2019	2020	2014	2014	2019	2020	2016
35	97460	1A	Kab. Halmahera Selatan	2019	2018	2018	2020	2018	2019	2019	2018	2014	2018	2015	2018
36	97530	1A	Kab. Manokwari	2015	2014	2013	2013	2013	2015	2019	2020	2018	2019	2014	2017
37	97560	1A	Kab. Biak Numfor	2018	2017	2019	2015	2014	2018	2019	2018	2014	2017	2016	2014
38	97600	1A	Kab. Kepulauan Sula	2017	2018	2017	2017	2018	2019	2019	2014	2018	2019	2015	2014
39	97682	1A	Kab. Nabire	2017	2013	2017	2018	2014	2013	2018	2018	2014	2018	2018	2011
40	97760	1A	Kab. Kaimana	2019	2019	2019	2018	2019	2014	2018	2019	2018	2018	2015	2017
41	97796	1A	Kab. Mimika	2014	2017	2014	2015	2014	2017	2018	2019	2014	2018	2018	2014
42	96001	1B	Kota Sabang	2013	2015	2020	2018	2016	2018	2011	2020	2018	2014	2020	2017
43	96011	1B	Kab. Aceh Besar	2015	2018	2018	2018	2014	2019	2012	2019	2015	2011	2015	2011
44	96035	1B	Kab. Deli Serdang	2013	2017	2015	2015	2019	2012	2017	2012	2017	2014	2018	2016
45	96071	1B	Kab. Padang Lawas Utara	2013	2016	2015	2015	2015	2014	2014	2017	2017	2011	2020	2014
46	96087	1B	Kota Batam	2013	2018	2017	2015	2019	2016	2018	2015	2011	2018	2014	2019
47	96089	1B	Kab. Karimun	2013	2017	2015	2019	2014	2017	2016	2015	2017	2017	2018	2014
48	96091	1B	Kota Tanjung Pinang	2018	2018	2017	2015	2019	2016	2018	2015	2016	2019	2014	2019
49	96145	1B	Kab. Kepulauan Anambas	2013	2018	2017	2019	2012	2018	2017	2015	2014	2017	2020	2020
50	96179	1B	Kab. Lingga	2013	2015	2017	2015	2015	2014	2017	2018	2018	2018	2017	2019
51	96237	1B	Kota Pangkal Pinang	2015	2015	2017	2014	2020	2018	2017	2018	2018	2018	2014	2020
52	96249	1B	Kab. Belitung	2018	2019	2017	2018	2014	2017	2014	2014	2011	2018	2015	2018
53	96253	1B	Kota Bengkulu	2019	2018	2015	2018	2020	2018	2014	2016	2018	2017	2020	2014
54	96805	1B	Kab. Cilacap	2019	2017	2017	2020	2019	2018	2015	2018	2014	2014	2018	2016
55	97430	1B	Kota Ternate	2018	2018	2018	2017	2014	2014	2019	2014	2012	2012	2018	2014
56	97690	1B	Kab. Jayapura	2016	2014	2019	2014	2019	2016	2016	2014	2018	2020	2014	2018
57	97724	1B	Kota Ambon	2019	2019	2020	2017	2019	2019	2019	2019	2014	2018	2014	2018
58	97748	1B	Kab. Seram Bagian Timur	2015	2011	2020	2019	2019	2019	2014	2014	2012	2012	2014	2018

59	97790	1B	Kab. Maluku Tengah	2019	2014	2020	2014	2019	2019	2015	2019	2013	2012	2015	2016
60	97810	1B	Kab. Maluku Tenggara	2015	2018	2015	2015	2017	2019	2018	2019	2018	2019	2016	2018
61	97980	1B	Kab. Merauke	2014	2017	2013	2019	2017	2017	2018	2013	2012	2012	2014	2018
62	96207	2A	Kab. Kerinci	2013	2018	2015	2019	2015	2014	2019	2015	2018	2014	2018	2014
63	96751	2A	Kab. Bogor	2019	2018	2018	2015	2017	2018	2020	2018	2018	2014	2014	2011
64	97124	2A	Kab. Tana Toraja	2013	2013	2019	2018	2014	2019	2014	2013	2013	2019	2018	2018
65	97686	2B	Kab. Jayawijaya	2018	2018	2015	2018	2017	2015	2014	2018	2018	2018	2014	2018
66	96745	3A	Kota Adm. Jakarta Pusat	2019	2013	2018	2019	2017	2017	2020	2015	2018	2018	2018	2015
67	96753	3A	Kota Bogor	2015	2013	2018	2019	2017	2017	2017	2017	2017	2018	2014	2011
68	96791	3A	Kab. Majalengka	2017	2013	2019	2019	2014	2017	2011	2013	2018	2011	2020	2016
69	96987	3A	Kab. Banyuwangi	2019	2020	2020	2020	2020	2020	2014	2014	2018	2012	2020	2015
70	97008	3A	Kab. Kepulauan Sangihe	2017	2014	2014	2017	2014	2016	2011	2012	2018	2018	2014	2014
71	97012	3A	Kab. Minahasa Utara	2019	2020	2020	2019	2018	2016	2016	2016	2018	2018	2014	2020
72	97014	3A	Kota Manado	2014	2018	2020	2019	2014	2016	2016	2018	2014	2018	2014	2020
73	97120	3A	Kab. Majene	2019	2014	2012	2017	2014	2019	2014	2014	2019	2020	2014	2017
74	97144	3A	Kota Kendari	2018	2014	2017	2013	2013	2018	2018	2019	2013	2020	2018	2016
75	97180	3A	Kab. Maros	2019	2013	2015	2014	2011	2018	2014	2019	2012	2020	2011	2017
76	97192	3A	Kota Bau Bau	2020	2019	2020	2017	2020	2020	2020	2019	2013	2020	2018	2018
77	97406	3A	Kab. Halmahera Utara	2019	2014	2013	2019	2014	2015	2016	2018	2018	2018	2015	2020
78	96293	3B	Kota Bandar Lampung	2017	2013	2017	2020	2011	2019	2019	2013	2018	2018	2014	2018
79	96295	3B	Kab. Lampung Selatan	2017	2014	2019	2019	2017	2016	2017	2015	2018	2012	2014	2016
80	96685	3B	Kota Banjarmasin	2019	2018	2019	2018	2014	2020	2014	2014	2018	2018	2016	2017
81	96741	3B	Kota Adm. Jakarta Utara	2015	2013	2018	2019	2014	2018	2014	2018	2018	2012	2018	2015
82	96749	3B	Kota Tangerang	2018	2015	2018	2018	2017	2018	2020	2015	2012	2018	2020	2017
83	96797	3B	Kab. Tegal	2015	2017	2018	2019	2017	2018	2017	2013	2018	2013	2018	2016
84	96837	3B	Kota Semarang	2017	2017	2017	2017	2017	2017	2020	2018	2018	2014	2020	2016
85	96839	3B	Kota Semarang	2019	2017	2017	2020	2017	2018	2020	2014	2018	2018	2020	2018
86	96925	3B	Kab. Gresik	2017	2018	2015	2020	2017	2019	2017	2018	2018	2013	2020	2018
87	96935	3B	Kab. Sidoarjo	2019	2017	2018	2020	2017	2017	2020	2014	2018	2011	2018	2017
88	97048	3B	Kab. Gorontalo	2019	2018	2018	2019	2017	2014	2019	2018	2014	2018	2020	2020
89	97072	3B	Kota Palu	2018	2018	2018	2018	2018	2018	2019	2018	2018	2018	2018	2017
90	97182	3B	Kota Makassar	2017	2014	2019	2014	2018	2018	2018	2014	2012	2020	2020	2018
91	97230	3B	Kab. Badung	2017	2020	2017	2020	2017	2015	2014	2015	2018	2018	2020	2018
92	97240	3B	Kota Mataram	2019	2011	2017	2019	2017	2020	2018	2014	2018	2013	2020	2014
93	97282	3B	Kab. Manggarai Barat	2017	2013	2020	2019	2017	2014	2017	2019	2017	2013	2020	2011
94	97502	3B	Kota Sorong	2017	2014	2017	2017	2014	2018	2016	2019	2014	2018	2018	2016
95	97260	4A	Kab. Sumbawa	2019	2013	2019	2014	2017	2014	2018	2014	2019	2012	2020	2014
96	97270	4A	Kota Bima	2015	2013	2017	2019	2017	2014	2020	2014	2015	2013	2020	2017
97	97300	4A	Kab. Sikka	2017	2012	2020	2020	2017	2017	2018	2015	2018	2012	2020	2018
98	97310	4A	Kab. Flores Timur	2015	2017	2013	2017	2017	2014	2014	2014	2018	2011	2016	2011
99	97320	4A	Kab. Alor	2015	2017	2013	2019	2019	2014	2014	2019	2018	2018	2020	2017
100	97340	4A	Kab. Sumba Timur	2017	2017	2018	2019	2017	2014	2018	2014	2018	2013	2012	2011
101	97372	4A	Kota Kupang	2015	2012	2013	2014	2019	2015	2014	2019	2015	2018	2020	2015

102	97378	4A	Kab. Rote Ndao	2015	2015	2013	2017	2017	2015	2014	2015	2018	2012	2016	2013
103	97380	4A	Kab. Kupang	2015	2015	2015	2020	2017	2015	2014	2019	2017	2014	2020	2018
104	96933	4B	Kota Surabaya	2017	2018	2018	2020	2017	2017	2020	2018	2018	2013	2018	2017
105	96937	4B	Kota Surabaya	2017	2017	2017	2020	2017	2017	2020	2015	2018	2013	2018	2016
106	96973	4B	Kab. Sumenep	2019	2019	2017	2019	2017	2020	2015	2013	2018	2012	2020	2018

The total sum of the selected TMMs at 106 sites in Indonesia from 2011 to 2020 is shown in Figure 36. In general, 2018 contributed the most to the composition of TMMs, while 2011 was the least significant contributor. The year 2018 contributes the most to the composition of February, March, June, August, September, October, November, and December TMMs, with a total of 28, 24, 21, 24, 50, 34, 30, and 23 months, respectively. The year 2019 had the highest contribution to January TMMs, accounting for a total of 25 months. Additionally, the most selected TMMs for April are from 2019, totaling 25 months. For May TMMs, the most selected year is 2017, with a total of 34 months. Finally, for the July TMMs, the most selected years were 2014, 2017, and 2018, each with 21 months.

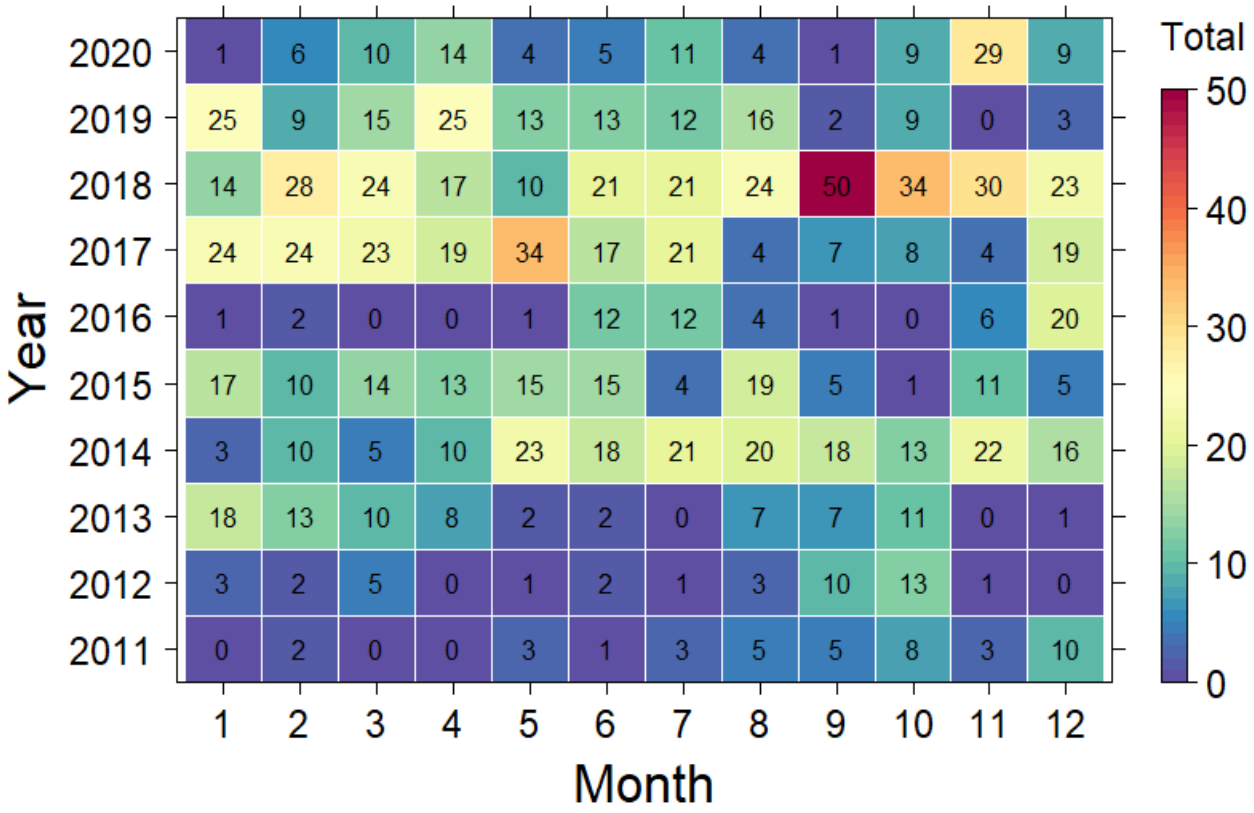

Figure 36. Total sum of the selected TMMs from 106 sites

6.3.2 Comparison among multiple years, LT, and TMY

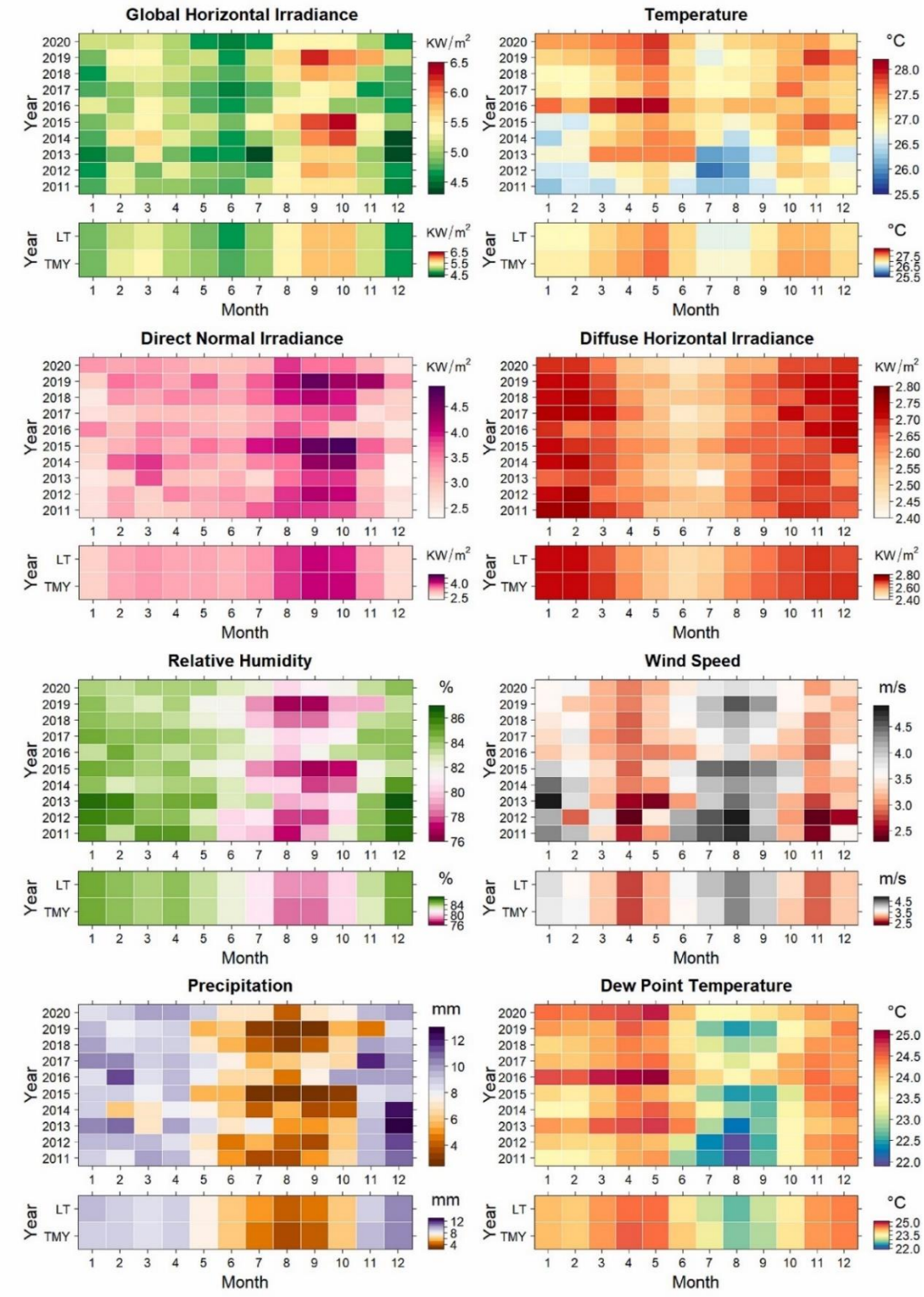

Figure 37. Comparison among multiple years, LT and TMY averages of all sites

The detailed annual comparison among the multiyear, LT and TMY values of each climate element, based on the average values across all sites in Indonesia, is depicted in Figure 37. The daily average global horizontal irradiance was the lowest in 2017, with a daily average of 4.9 kW/m^{2,} while 2019 was the year with the highest global horizontal irradiance, with a daily average of 5.4 kW/m^2. The daily averages of the global horizontal irradiance of TMY and LT were found to be 5.2 kW/m^2 and 5.1 kW/m^2, respectively. Based on multiyear temperature analysis, 2011 was the coldest year, with an average daily temperature of 26.6°C, while 2016 was the warmest year, with an average daily temperature of 27.5°C. Additionally, the daily mean temperatures of TMY and LT were found to be 27.1°C and 27.1°C, respectively.

The year 2017 had the lowest direct normal irradiance, with a daily average of 3.1 kW/m^2, while 2019 had the highest direct normal irradiance, with a daily average of 3.7 kW/m^2. The daily average direct normal irradiance of TMY and LT was found to be 3.4 kW/m^2 and 3.4 kW/m^2, respectively. 2020 was the year with the lowest diffuse horizontal irradiance, with a daily average of 2.59 kWm^2, while 2015 was the year with the highest diffuse horizontal irradiance, with a daily average of 2.64 kW/m^2. The daily average diffuse horizontal irradiance of TMY and LT was found to be 2.63 kW/m^2 and 2.63 kW/m^2, respectively.

2019 was the year with the lowest relative humidity with a daily average of 81%, while 2013 was the year with the highest relative humidity with a daily average of 84%. The TMY and LT were 82.3% and 82.3%, respectively, for the average daily relative humidity. 2016 was the year with the lowest wind speed, with an average daily wind speed of 3.2 m/s, while 2015 was the year with the highest wind speed, with an average daily wind speed of 3.7 m/s. The daily mean wind speeds of TMY and LT were found to be 3.5 m/s and 3.5 m/s, respectively.

Based on multiyear rainfall analysis, 2019 was the year with the least precipitation, with a daily average of 6.1 mm, while 2017 was the year with the highest precipitation, with a daily average of 8.4 mm. Meanwhile, the daily average precipitation for TMY and LT was found to be 7.2 mm and 7.4 mm, respectively. 2011 was the year with the lowest dew point temperature, with a daily average of 23.4°C, while 2016 was the year with the highest dew point temperature, with a daily average of 24.3°C. It was discovered that TMY and LT had daily average dew point temperatures of 23.9 and 23.8°C, respectively. Nevertheless, this analysis also found closeness between TMYs and long-term average values for each climate element. In addition, this analysis provides an illustration that there are differences at the same time in TMY and multiyear variability

in each climate element. This information needs to be accounted for when designing the building.

The selection of TMY is determined based on the ability of each climate element to follow its LT pattern on hourly, daily, monthly, seasonal, and annual scales. It is important to compare TMY with LT using the actual hourly, daily, monthly seasonal, and annual scale patterns of all climate elements, especially global solar radiation and temperature. Based on Figure 38.a, it can be seen that the TMY diffuse horizontal irradiance has the highest correlation with LT, showing that the pattern of diffuse horizontal irradiance produced in the TMY generation is the closest to the long-term average for 2011-2020 compared to other climate elements. Meanwhile, TMY precipitation has the lowest correlation with LT. Figure 38.b shows the distribution of correlation values between the TMY and LT for each climate element. The correlation of direct normal irradiance ranges from 0.78 to 0.96 with an average of 0.89. The correlation of precipitation ranges from 0.28 to 0.60 with an average of 0.44. The global horizontal irradiance correlation ranges from 0.91 to 0.99 with an average of 0.96. The diffuse horizontal irradiance correlation ranges from 0.95 to 0.99 with an average of 0.97. The temperature correlation ranges from 0.66 to 0.93 with an average of 0.86. The correlation of wind speed ranges from 0.43 to 0.81 with an average of 0.62. The correlation of relative humidity ranges from 0.51 to 0.92 with an average of 0.81. The correlation of the dew point temperature ranges from 0.42 to 0.86 with an average of 0.65.

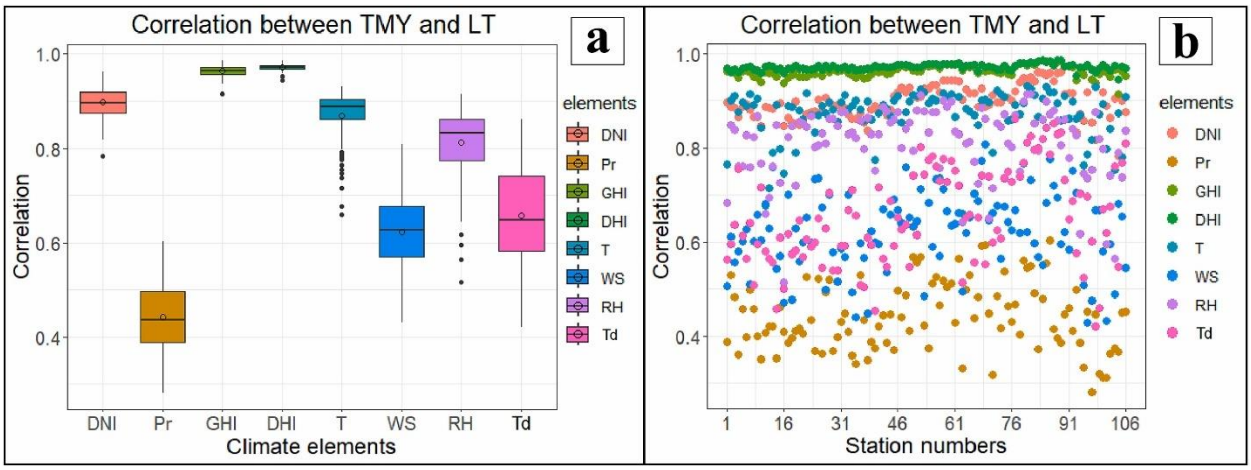

Figure 38. Correlations among eight climate elements between the TMY and LT

The hourly TMY composed of the 12 selected TMMs was verified by RMSE, MAE, and MSE to assess the accuracy of each climate element of TMY against the long-term frequency distribution, which in this case is represented by the hourly LT. The results of the RMSE

calculation conducted for each climate element between LT and TMY for 106 sites are shown in Figure 39. The results indicate that the RMSE distribution of each climatic element varies between the sites. The RMSE of the global horizontal irradiance distribution ranges from 55 to 94 W/m^2 with an average of 75 W/m^2. The RMSE of the temperature distribution ranges from 0.9 to 1.7°C with an average of 1.3°C. The RMSE of the direct normal irradiance distribution ranges from 75 to 108 W/m^2 with an average of 91 W/m^2. The RMSE of the diffuse horizontal irradiance distribution ranges from 24 to 45 W/m^2 with an average of 31 W/m^2. The RMSE of the relative humidity distribution ranges from 5 to 9% with an average of 6%. The RMSE of the wind speed distribution ranges from 1.2 to 4.4 m/s with an average of 2.4 m/s. The RMSE of the precipitation distribution ranges from 0.24 to 1.98 mm with an average of 0.69 mm. The RMSE of the dew point temperature distribution ranges from 0.7 to 1.7°C with an average of 1°C.

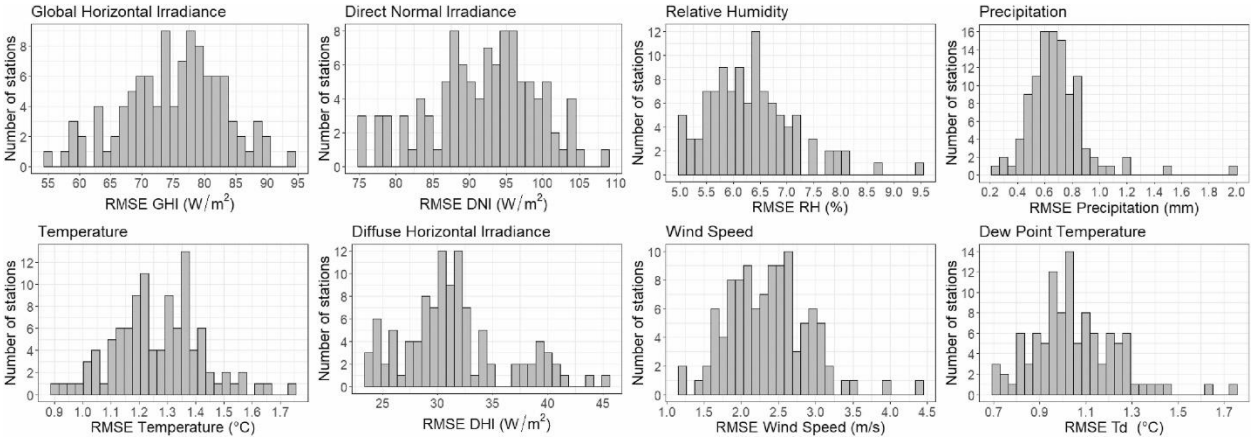

Figure 39. Distribution of RMSE

The results of the MAE calculation performed for each climate element between LT and TMY for 106 sites are shown in Figure 40. The calculation results indicate that there is a distinct MAE distribution for each climate element across various sites. The MAE of the global horizontal irradiance distribution ranges from 25 to 47 W/m^2 with an average of 37 W/m^2. The MAE of the temperature distribution ranges from 0.7 to 1.4°C with an average of 1°C. The MAE of the direct normal irradiance distribution ranges from 34 to 55 W/m^2 with an average of 46 W/m^2. The MAE of the diffuse horizontal irradiance distribution ranges from 10 to 22 W/m^2 with an average of 16 W/m^2. The MAE of the relative humidity distribution ranges from 4 to 7% with an average of 5%. The MAE of the wind speed distribution ranges from 0.9 to 3.6 m/s with an average of 1.8 m/s. The precipitation distribution ranges from 0.21 to 1.2 mm with an average of 0.3 mm. The MAE

of the dew point temperature distribution ranges from 0.6 to 1.3°C with an average of 0.8°C.

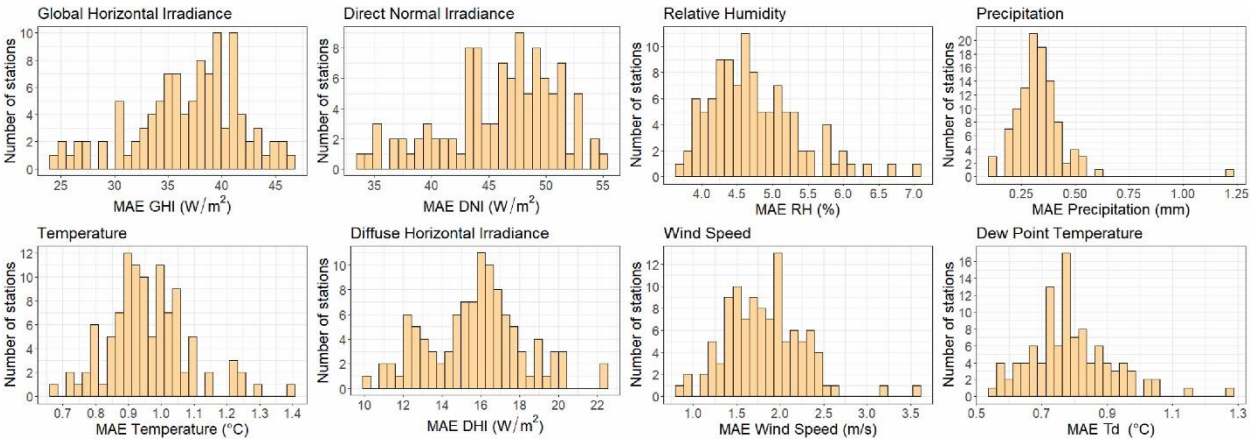

Figure 40. Distribution of MAE

The results of the MSE calculation performed for each climate element between LT and TMY for 106 sites are shown in Figure 41. The outcomes of the MSE calculation also demonstrate that the MSE distribution of each climatic element differs across sites. The MSE of the global horizontal irradiance distribution ranges from 3017 to 8805 W/m^2 with an average of 5698 W/m^2. The MSE of the temperature distribution ranges from 0.8 to 3°C with an average of 1.6°C. The MSE of the direct normal irradiance distribution ranges from 5654 to 11730 W/m^2 with an average of 8478 W/m^2. The MSE of the diffuse horizontal irradiance distribution ranges from 559.7 to 2039.4 W/m^2 with an average of 1008.5 W/m^2. The MSE of the relative humidity distribution ranges from 26 to 90% with an average of 41%. The MSE of the wind speed distribution ranges from 1.5 to 19.4 m/s with an average of 5.9 m/s. The MSE of the precipitation distribution ranges from 0.059 to 3.918 mm with an average of 0.522 mm. The MSE of the dew point temperature distribution ranges from 0.5 to 3°C with an average of 1.1°C.

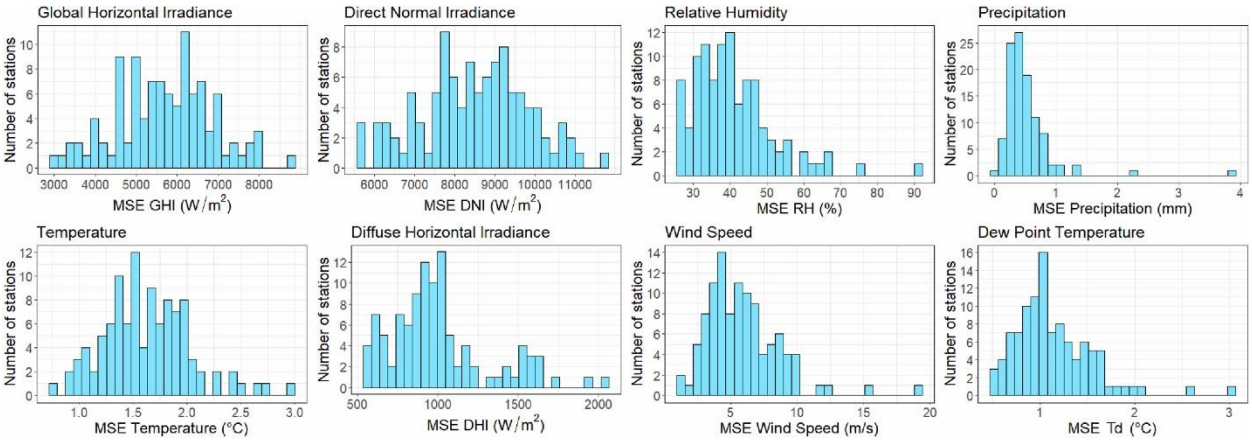

Figure 41. Distribution of MSE

6.3.3 Pattern of the TMY in each climate zone

The annual patterns of monthly climate elements based on TMYs generation in different climate zones are shown in Figure 42. To calculate the monthly patterns of TMYs, eight different climate zones were considered, with the following average site representations: 41 sites for climate zone 1A (equatorial), 20 sites for climate zone 1B (sub-equatorial), 3 sites for climate zone 2A (highland tropical), 1 site for climate zone 2B (very highland tropical), 12 sites for climate zone 3A (monsoonal), 17 sites for climate zone 3B (sub-monsoonal), 9 sites for climate zone 4A (savanna), and 3 sites for climate zone 4B (sub-savanna), which refers to the results of climate zoning in Indonesia from chapter 2 this thesis.

TMYs patterns can explain well the annual characteristics of Indonesia's climate in different climate zones. Based on TMYs, climate zones 4A and 4B receive more solar radiation than the other 6 climate zones. The global horizontal irradiance in climate zones 4A and 4B reaches its peak during September-October, with values of 7.2 kW/m^2 and 7.0 kW/m^{2,} respectively. Similarly, the direct normal irradiance also reaches its peak during this period, with values of 6.0 kW/m^2 and 5.7 kW/m^2, respectively. Based on the temperature pattern of TMYs, it was found that the air temperature in climate zones 1A and 1B does not vary much in their annual cycles, with daily averages ranging from 27.0 to 27.6°C and 26.9 to 27.8°C, respectively. Meanwhile, climate zones 2A and 2B exhibit relatively low temperatures year-round. Climate zones 3A, 3B, 4A, and 4B, which are primarily located south of the equator geographically, experience a slight decrease in temperature from June to September.

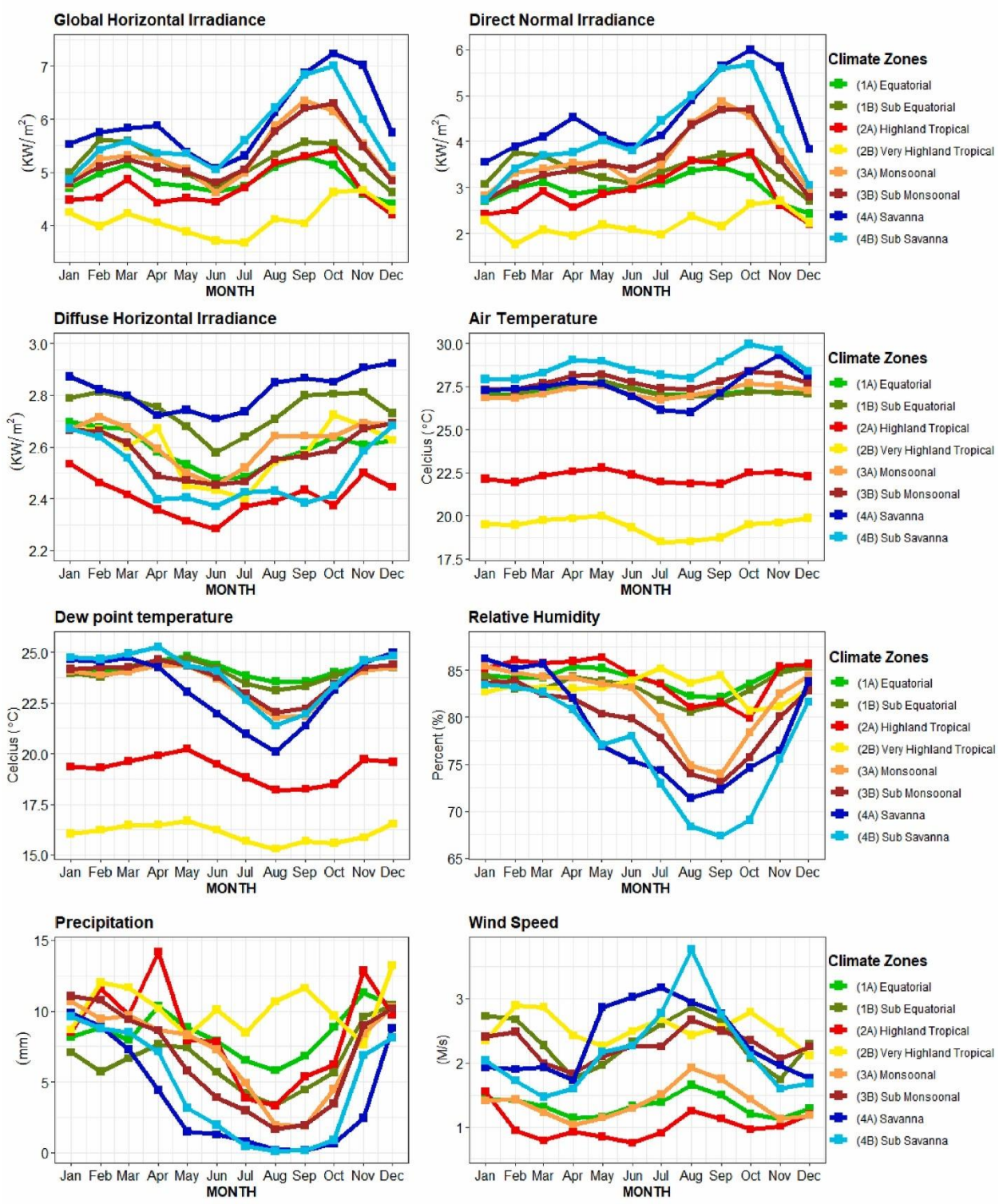

Figure 42. Annual pattern of each climate element of the TMY within various climate zones

According to TMYs generation, climate zone 1A, which is situated in the equatorial region, has weak winds and an overall humid environment, with monthly averages for RH and wind speeds

of 82.1 to 85.4% and 1.1 to 1.7 m/s, respectively. Climate zones 3B, 4A, and 4B have a yearly climatic cycle characterized by a minimum relative humidity drop below 80% from June to October. This coincides with the relatively strong wind conditions, as indicated by the monthly average wind speed of the TMYs above 2 m/s. Climate zones 1A and 1B have a rainfall pattern with two peaks occurring in October–November and in March-May. The TMYs rainfall patterns in climate zones 3A, 3B, 4A, and 4B exhibit a peak during the rainy season, typically observed from November to March. On the other hand, climate zones 4A and 4B were discovered to have a longer dry season with a short rainy season. This study has shown that the annual patterns of the generated TMYs can be well explained in different climate zones of Indonesia.

Chapter 7. Conclusion

7.1 Summary of research results

Based on the analysis carried out in each dissertation chapter, this research concludes several points as follows:

The new integrated climate zones developed in this study differed from those of the previous Koppen climate zoning and obtained more detailed and optimum results based on spatial and temporal distribution (diurnal, seasonal, and annual). This is because the integrated climate zoning in this study considered topographic data and more climate elements including air temperature, wind speed, relative humidity, atmospheric pressure, total cloud cover, mixing ratio, global solar irradiance, and precipitation with high (hourly) temporal resolution data. The availability of information on climate classification in this study was divided into eight new integrated climate zones, namely, climate zone 1A (equatorial), climate zone 1B (sub equatorial), climate zone 2A (highland tropical), climate zone 2B (very highland tropical), climate zone 3A (monsoon), climate zone 3B (sub monsoon), climate zone 4A (savanna), and climate zone 4B (sub savanna), in the territory of Indonesia. This has been different from the Koppen classification, which divides Indonesia into only three climate zones, namely, the Af, Am, and Aw.

In the passive method, by taking the lower probability limit of 50 %, the monsoon, savanna, and sub savanna climate zones are suitable for the comfort ventilation method. Meanwhile, the sub equatorial climate zone is suitable for applying passive methods by combining night ventilation and comfort ventilation. This study used an approach that assumed that the physical structure of the building includes the thermal capacity of the building mass, window openings, and the determination of the indoor environmental limits of Tb, WSb, and RHb for the calculation of various methods, including CDD, cooling load, night ventilation, evaporative cooling, and comfort ventilation, which in reality can fluctuate. Based on this assessment, the passive method implementation plan in each zone can apply a single passive method or a combination of passive methods. Engineers, architects, and designers can refer to the information obtained in this initial research to determine potential passive design strategies and basic design decisions during the initial design stage before detailed building simulation analyses are carried out for each different climatic zone. Future research is needed to establish detailed building design guidelines based on more quantitative data that consider more factors that affect the accuracy of passive cooling

methods for each zone.

Analysis of solar radiation, local scale climate, and passive cooling potential in Tangerang during 2021 can be concluded that the intensity of global horizontal irradiance has a high intensity throughout the year with the maximum diurnal intensity occurring between 12.00 and 13.00 LT. The highest vertical surface irradiance intensity was recorded from a sensor facing east and the lowest intensity from a sensor facing south. The vertical surface irradiance from the south has a maximum increase in intensity during the December, January, and February (DJF) season, while the vertical surface irradiance from the north has a maximum increase in intensity during the June, July, and August (JJA) season. In terms of local scale climate, Tangerang is a monsoonal climate zone with seasonal variations in wind direction. namely the DJF season, the dominant wind comes from the west which shows the air mass coming from the Asian continent. While the JJA season the dominant wind comes from the east, which means the wind comes from Australia. On a diurnal basis, the wind speed increases during the day and calms down at night. Daily temperature conditions have an average maximum of 33.5^{o}C with an average minimum RH of 62.6% during the day, an average minimum temperature of 23.7^{o}C and an average maximum RH of 99.6% at night. In optimizing the passive cooling building design, several things need to be considered, namely, daytime comfort ventilation has good potential throughout the year. According to the direction frequency and wind speed, windows opening will be effective if they face west, north, and east to maximize wind flow into the building through the windows during the day. Night ventilation has good potential when the building structure is set to store cold when the outdoor temperature drops below 26^{o}C.

Based on the analysis carried out on the global horizontal and vertical components in four orientation directions in Jembrana-Bali, it was concluded that under all sky conditions, the maximum monthly average global horizontal irradiance occurs in January of 432.4 W/m^{2} while the minimum average occurs in July of 327.9 W/m^{2}. On an annual and diurnal basis, the average hourly clearness index statistical calculation ranges from 0.12 to 0.68 with an average of 0.47. Based on sun-path analysis, the Jembrana-Bali area gets more sunlight from the east, west and north which can be used to optimize building orientation and window placement. The findings from this study will provide initial insights for architects, engineers and policy makers involved in sustainable building design and energy planning in the Bali region. This research is a preliminary study conducted on the five components of solar irradiance, clearness index and sun-path in

Jembrana-Bali (located in the monsoon climate zone) for one year. Further research is needed by considering a longer time series of observations and compared with different climate zones.

Based on the proposed method for developing typical meteorological years based on relatively limited observational data, it is concluded that the proposed bias correction formulation with quantile mapping for temperature, relative humidity, and wind speed elements has proven to be effective in improving the accuracy of ERA5 reanalysis datasets. The formula effectively reduced the distribution of each bias to a smaller one. The original temperature bias of −4.5 °C to 2.7 °C was reduced to a narrower range of −0.014 °C to 0.005 °C. The relative humidity bias was originally −6 % to 10 % and was narrowed to −0.32 % to 0.07 %. The distribution of wind speed bias originally ranging from −4 m/s to 2 m/s was reduced to −0.02 m/s to 0.35 m/s. The bias-corrected ERA5 reanalysis dataset was used to fill in the missing observational values varying between 29.96 % and 50.19 % from the total hourly observational data of temperature, relative humidity, and wind speed collected during the 2011–2020 period for the process of developing TMYs.

The Sandia method based on the modified FS statistical weighting for global horizontal irradiance, direct normal irradiation, diffuse horizontal irradiation, temperature, precipitation, wind speed, relative humidity, and dew point temperature, has been applied to develop TMYs across 106 sites, situated within eight different climate zones in Indonesia. The results of the TMYs selection showed that the year selection for TMMs varied significantly at each site, and the local climatic conditions had a major influence on the variation in the resulting TMMs in different climate zones. Based on statistical verification, the resulting TMYs closely captured the long-term distribution pattern, particularly for global horizontal irradiance and temperature. The above results were found based on the correlation, RMSE, MAE and MSE between TMY and LT, with averages of 0.96, 75 W/m^2, 37 W/m^2, and 5698 W/m^2 for global horizontal irradiance, and 0.86, 1.3 °C, 1 °C, and 1.6 °C for temperature. Additionally, the demonstrated TMYs generation method in this study can be applied in any other country, where the quality control procedure of the weather observational datasets is necessary. Furthermore, the generated TMYs dataset will be highly beneficial for a variety of applications, especially in building performance simulation, such as energy-efficient building designs, and climate-responsive architectural designs, in the future.

Acknowledgments

This doctoral thesis as part of the Development of Low-Carbon Affordable Apartments in the Hot-Humid Climate of Indonesia Project toward the Paris Agreement 2030, Science and Technology Research Partnership for Sustainable Development (SATREPS), collaboratively supported by the Japan Science and Technology Agency, Japan International Cooperation Agency (JICA), Hiroshima University, Kagoshima University, Ministry of Public Works and Housing (PUPR) of Indonesia, and the Indonesian Agency for Meteorology Climatology and Geophysics (BMKG).

List of publications

Parts of this doctoral thesis have been published in journals and presented at international conferences as follows:

<u>International journal publications</u>

1. Putra IDGA, Nimiya H, Sopaheluwakan A, Kubota T, Lee HS, Pradana RP, Alfata MNF, Perdana RB, Permana DS, Riama NF. (2022) Development of climate zones for passive cooling techniques in the hot and humid climate of Indonesia. Build. Environ., 226, 109698.

2. Putra IDGA, Nimiya H, Sopaheluwakan A, Kubota T, Lee HS, Pradana RP, Alfata MNF, Perdana RB, Permana DS, Riama NF, Karnawati D. (2024) Development of typical meteorological years based on quality control of datasets in Indonesia. Renew. Energy., 221, 119699.

<u>International conferences presented and publications</u>

1. Putra I.D.G.A., Nimiya H., Kubota T., Lee H.S., Iketani F., Trihamdani A.R., Sopaheluwakan A., Alfata M.N.F., Permana D.S., Pradana R.P., Study of Vertical Surfaces Solar Irradiance and Local Scale Climate for Building Design in Tangerang of Indonesia. IAQVEC 2023, May 20-23, Tokyo, Japan

2. Putra I.D.G.A., Nimiya H., Yuda I.W.A., Kubota T., Lee H.S., Permana D.S., Sorfian, Nuryanto D.E., Alfata M.N.F, Trihamdani A.R, Fajariana Y., Sopaheluwakan A., Hidayanto N., Pradana R.P., Roniri A.A., Study of global horizontal and vertical solar irradiance components under different sky conditions for sustainable building design in Bali of Indonesia. SENVAR 2023, October 20-21, Manado, Indonesia

References

[1] Marzuki, H. Hashiguchi, M. Vonnisa, Harmadi, Seasonal and Diurnal Variations of Vertical Profile of Precipitation over Indonesian Maritime Continent, Eng. Math. Top. Rainfall. (2018). https://doi.org/10.5772/intechopen.74044.

[2] C.S. RAMAGE, Role of a Tropical "Maritime Continent" in the Atmospheric Circulation 1 , Mon. Weather Rev. 96 (1968) 365–370. https://doi.org/10.1175/1520-0493(1968)096<0365:roatmc>2.0.co;2.

[3] J. Bjerknes, Monthly Weather Reyiew Atmospheric Teleconnections From the Equatorial Pacific, Mon. Weather Rev. 97 (1969) 163–172. http://journals.ametsoc.org/doi/abs/10.1175/1520-0493(1969)097%3C0163:ATFTEP%3E2.3.CO;2.

[4] H. Lee, General Rainfall Patterns in Indonesia and the Potential Impacts of Local Seas on Rainfall Intensity, Water. 7 (2015) 1751–1768. https://doi.org/10.3390/w7041751.

[5] N. Saji, B. Goswami, P. Vinayachandran, T. Yamagata, A dipole mode in the Tropical Ocean, Nature. 401 (1999) 360–363.

[6] M.N. Nur'utami, R. Hidayat, Influences of IOD and ENSO to Indonesian Rainfall Variability: Role of Atmosphere-ocean Interaction in the Indo-pacific Sector, Procedia Environ. Sci. 33 (2016) 196–203. https://doi.org/10.1016/j.proenv.2016.03.070.

[7] Y. Kosaka, Y. Matsuda, Roles of Rossby and gravity waves on circulation associated with tropical and subtropical heating, J. Meteorol. Soc. Japan. 83 (2005) 481–498. https://doi.org/10.2151/jmsj.83.481.

[8] N. Sakurai, F. Murata, M.D. Yamanaka, S. Mori, J.I. Hamada, H. Hashiguchi, Y.I. Tauhid, T. Sribimawati, B. Suhardi, Diurnal cycle of cloud system migration over Sumatera Island, J. Meteorol. Soc. Japan. 83 (2005) 835–850. https://doi.org/10.2151/jmsj.83.835.

[9] A.R. As-syakur, K. Imaoka, K. Ogawara, M.D. Yamanaka, T. Tanaka, Y. Kashino, I.W. Nuarsa, T. Osawa, Analysis of spatial and seasonal differences in the diurnal rainfall cycle over sumatera revealed by 17-year TRMM 3B42 dataset, Sci. Online Lett. Atmos. 15 (2019) 216–221. https://doi.org/10.2151/sola.2019-039.

[10] R.A. Madden, P.R. Julian, Description of Global-Scale Circulation Cells in the Tropics with a 40–50 Day Period, J. Atmos. Sci. 29 (1972) 1109–1123.

https://doi.org/10.1175/1520-0469(1972)029<1109:dogscc>2.0.co;2.

[11] A. Seiki, S. Yokoi, M. Katsumata, The impact of diurnal precipitation over sumatra island, indonesia, on synoptic disturbances and its relation to the madden-julian oscillation, J. Meteorol. Soc. Japan. 99 (2021) 113–137. https://doi.org/10.2151/jmsj.2021-007.

[12] F.R. Muhammad, S.W. Lubis, S. Setiawan, Impacts of the Madden–Julian oscillation on precipitation extremes in Indonesia, Int. J. Climatol. 41 (2021) 1970–1984. https://doi.org/10.1002/joc.6941.

[13] C. Zhang, Madden-julian oscillation: Bridging weather and climate, Bull. Am. Meteorol. Soc. 94 (2013) 1849–1870. https://doi.org/10.1175/BAMS-D-12-00026.1.

[14] C. Zhang, MADDEN-JULIAN OSCILLATION, (2005) 1–36. https://doi.org/10.1029/2004RG000158.1.INTRODUCTION.

[15] J.H. Qian, A.W. Robertson, V. Moron, Interactions among ENSO, the Monsoon, and Diurnal Cycle in Rainfall Variability over Java, Indonesia, J. Atmos. Sci. 67 (2010) 3509–3524. https://doi.org/10.1175/2010JAS3348.1.

[16] V. Moron, A.W. Robertson, R. Boer, Spatial coherence and seasonal predictability of monsoon onset over Indonesia, J. Clim. 22 (2009) 840–850. https://doi.org/10.1175/2008JCLI2435.1.

[17] Y. Ding, The variability of the Asian summer monsoon, J. Meteorol. Soc. Japan. 85 B (2007) 21–54. https://doi.org/10.2151/jmsj.85B.21.

[18] V. Moron, A.W. Robertson, J.H. Qian, Local versus regional-scale characteristics of monsoon onset and post-onset rainfall over Indonesia, Clim. Dyn. 34 (2010) 281–299. https://doi.org/10.1007/s00382-009-0547-2.

[19] R.H. JOHNSON, Diurnal Cycle of Monsoon Convection, (2011) 257–276. https://doi.org/10.1142/9789814343411_0015.

[20] J.H. Qian, Why precipitation is mostly concentrated over islands in the maritime continent, J. Atmos. Sci. 65 (2008) 1428–1441. https://doi.org/10.1175/2007JAS2422.1.

[21] M.D. Yamanaka, Physical climatology of Indonesian maritime continent: An outline to comprehend observational studies, Atmos. Res. 178–179 (2016) 231–259. https://doi.org/10.1016/j.atmosres.2016.03.017.

[22] D. Machiwal, S. Kumar, H.M. Meena, P. Santra, R.K. Singh, D. V. Singh, Clustering of rainfall stations and distinguishing influential factors using PCA and HCA techniques

over the western dry region of India, Meteorol. Appl. 26 (2019) 300–311. https://doi.org/10.1002/met.1763.

[23] L. Yang, D. Liu, Y. Mao, Z. Li, J. Liu, Using a Bioclimatic Approach to Developing Combined Pre-design Strategies for Energy-efficient Buildings in China, J. Human-Environment Syst. 10 (2007) 39–44. https://doi.org/10.1618/jhes.10.39.

[24] N. Islam, Defining Homogenous Climate zones of Bangladesh using Cluster Analysis, 6 (2019) 119–129.

[25] P. Netzel, T. Stepinski, On using a clustering approach for global climate classification, J. Clim. 29 (2016) 3387–3401. https://doi.org/10.1175/JCLI-D-15-0640.1.

[26] A.T. DeGaetano, Delineation of mesoscale climate zones in the northeastern United States using a novel approach to cluster analysis, J. Clim. 9 (1996) 1765–1782. https://doi.org/10.1175/1520-0442(1996)009<1765:DOMCZI>2.0.CO;2.

[27] E. Kahya, M.C. Demirel, O.A. Bég, Hydrologic homogeneous regions using monthly streamflow in Turkey, Earth Sci. Res. J. 12 (2008) 181–193.

[28] Y. Unal, T. Kindap, M. Karaca, Redefining the climate zones of Turkey using cluster analysis, Int. J. Climatol. 23 (2003) 1045–1055. https://doi.org/10.1002/joc.910.

[29] S. Yokoi, Y.N. Takayabu, K. Nishii, H. Nakamura, H. Endo, H. Ichikawa, T. Inoue, M. Kimoto, Y. Kosaka, T. Miyasaka, K. Oshima, N. Sato, Y. Tsushima, M. Watanabe, Application of cluster analysis to climate model performance metrics, J. Appl. Meteorol. Climatol. 50 (2011) 1666–1675. https://doi.org/10.1175/2011JAMC2643.1.

[30] L.F. Pineda-Martínez, N. Carbajal, Climatic analysis linked to land vegetation cover of Mexico by applying multivariate statistical and clustering analysis, Atmosfera. 30 (2017) 233–242. https://doi.org/10.20937/ATM.2017.30.03.04.

[31] P.M. de B. Terassi, E. Galvani, Identification of homogeneous rainfall regions in the Eastern watersheds of the state of Paraná, Brazil, Climate. 5 (2017). https://doi.org/10.3390/cli5030053.

[32] C.A.G. Santos, R.M.B. Neto, R.M. da Silva, S.G.F. Costa, Cluster analysis applied to spatiotemporal variability of monthly precipitation over Paraíba state using tropical rainfall measuring mission (TRMM) data, Remote Sens. 11 (2019). https://doi.org/10.3390/rs11060637.

[33] A.S. Rahman, A. Rahman, Application of principal component analysis and cluster

analysis in regional flood frequency analysis: A case study in new South Wales, Australia, Water (Switzerland). 12 (2020) 1–26. https://doi.org/10.3390/w12030781.

[34] S. Fiddes, A. Pepler, K. Saunders, P. Hope, Redefining southern Australia's climatic regions and seasons, J. South. Hemisph. Earth Syst. Sci. 71 (2021) 92–109. https://doi.org/10.1071/ES20003.

[35] R.E. Benestad, D. Chen, A. Mezghani, L. Fan, K. Parding, On using principal components to represent stations in empirical-statistical downscaling, Tellus, Ser. A Dyn. Meteorol. Oceanogr. 6 (2015). https://doi.org/10.3402/tellusa.v67.28326.

[36] S. Jewson, An alternative to PCA for estimating dominant patterns of climate variability and extremes, with application to U.S. and China Seasonal Rainfall, Atmosphere (Basel). 11 (2020) 1–22. https://doi.org/10.3390/atmos11040354.

[37] W.L. Cerón, J. Molina-Carpio, I. Ayes Rivera, R.V. Andreoli, M.T. Kayano, T. Canchala, A principal component analysis approach to assess CHIRPS precipitation dataset for the study of climate variability of the La Plata Basin, Southern South America, Nat. Hazards. 103 (2020) 767–783. https://doi.org/10.1007/s11069-020-04011-x.

[38] J.C. Lam, L. Yang, J. Liu, Development of passive design zones in China using bioclimatic approach, Energy Convers. Manag. 47 (2006) 746–762. https://doi.org/10.1016/j.enconman.2005.05.025.

[39] O. Rakoto Joseph, F. Garde, J.P. Randrianasolo, Development of climatic zones and passive design principles in the housing sector for the island of madagascar, ISES Sol. World Congr. 2007, ISES 2007. 1 (2007) 248–252. https://doi.org/10.1007/978-3-540-75997-3_40.

[40] Á. Arroyo, Á. Herrero, V. Tricio, E. Corchado, Analysis of meteorological conditions in Spain by means of clustering techniques, J. Appl. Log. 24 (2017) 76–89. https://doi.org/10.1016/j.jal.2016.11.026.

[41] C. Wang, Y. Li, S.W. Myint, Q. Zhao, E.A. Wentz, Impacts of spatial clustering of urban land cover on land surface temperature across Köppen climate zones in the contiguous United States, Landsc. Urban Plan. 192 (2019) 103668. https://doi.org/10.1016/j.landurbplan.2019.103668.

[42] J.P. Praene, B. Malet-Damour, M.H. Radanielina, L. Fontaine, G. Rivière, GIS-based approach to identify climatic zoning: A hierarchical clustering on principal component

analysis, Build. Environ. 164 (2019) 106330. https://doi.org/10.1016/j.buildenv.2019.106330.

[43] Z. Hao, X. Zhang, J. Xie, J. Wang, J. Liu, Building climate zones of major marine islands in China defined using two-stage zoning method and clustering analysis, Front. Archit. Res. (2020). https://doi.org/10.1016/j.foar.2020.07.004.

[44] Y. Shi, G. Wang, Changes in building climate zones over China based on high-resolution regional climate projections, Environ. Res. Lett. 15 (2020). https://doi.org/10.1088/1748-9326/abbde8.

[45] J.I. Hamada, M.D. Yamanaka, J. Matsumoto, S. Fukao, P.A. Winarso, T. Sribimawati, Spatial and temporal variations of the rainy season over Indonesia and their link to ENSO, J. Meteorol. Soc. Japan. 80 (2002) 285–310. https://doi.org/10.2151/jmsj.80.285.

[46] H.H. Hendon, Indonesian rainfall variability: Impacts of ENSO and local air-sea interaction, J. Clim. 16 (2003) 1775–1790. https://doi.org/10.1175/1520-0442(2003)016<1775:IRVIOE>2.0.CO;2.

[47] E. Aldrian, R. Dwi Susanto, Identification of three dominant rainfall regions within Indonesia and their relationship to sea surface temperature, Int. J. Climatol. 23 (2003) 1435–1452. https://doi.org/10.1002/joc.950.

[48] H. Kuswanto, D. Setiawan, A. Sopaheluwakan, Clustering of Precipitation Pattern in Indonesia Using TRMM Satellite Data, Eng. Technol. Appl. Sci. Res. 9 (2019) 4484–4489. https://doi.org/10.48084/etasr.2950.

[49] H.E. Beck, N.E. Zimmermann, T.R. McVicar, N. Vergopolan, A. Berg, E.F. Wood, Present and future köppen-geiger climate classification maps at 1-km resolution, Sci. Data. 5 (2018) 1–12. https://doi.org/10.1038/sdata.2018.214.

[50] A.K. Nanda, C.K. Panigrahi, A state-of-the-art review of solar passive building system for heating or cooling purpose, Front. Energy. 10 (2016) 347–354. https://doi.org/10.1007/s11708-016-0403-0.

[51] K.M. Al-Obaidi, M. Ismail, A.M. Abdul Rahman, A study of the impact of environmental loads that penetrate a passive skylight roofing system in Malaysian buildings, Front. Archit. Res. 3 (2014) 178–191. https://doi.org/10.1016/j.foar.2014.03.004.

[52] N. Zhu, Z. Ma, S. Wang, Dynamic characteristics and energy performance of buildings using phase change materials: A review, Energy Convers. Manag. 50 (2009) 3169–3181.

https://doi.org/10.1016/j.enconman.2009.08.019.

[53] A.S. Gardner, I.M.D. Maclean, K.J. Gaston, A new system to classify global climate zones based on plant physiology and using high temporal resolution climate data, J. Biogeogr. 47 (2020) 2091–2101. https://doi.org/10.1111/jbi.13927.

[54] A. Walsh, D. Cóstola, L.C. Labaki, Review of methods for climatic zoning for building energy efficiency programs, Build. Environ. 112 (2017) 337–350. https://doi.org/10.1016/j.buildenv.2016.11.046.

[55] F. Amirifard, S.A. Sharif, F. Nasiri, Application of passive measures for energy conservation in buildings–a review, Adv. Build. Energy Res. 13 (2019) 282–315. https://doi.org/10.1080/17512549.2018.1488617.

[56] D.K. Bhamare, M.K. Rathod, J. Banerjee, Passive cooling techniques for building and their applicability in different climatic zones—The state of art, Energy Build. 198 (2019) 467–490. https://doi.org/10.1016/j.enbuild.2019.06.023.

[57] H. Goudarzi, A. Mostafaeipour, Energy saving evaluation of passive systems for residential buildings in hot and dry regions, Renew. Sustain. Energy Rev. 68 (2017) 432–446. https://doi.org/10.1016/j.rser.2016.10.002.

[58] J. Fernandes, R. Mateus, H. Gervásio, S.M. Silva, L. Bragança, Passive strategies used in Southern Portugal vernacular rammed earth buildings and their influence in thermal performance, Renew. Energy. 142 (2019) 345–363. https://doi.org/10.1016/j.renene.2019.04.098.

[59] K. Dharmasastha, D.G.L. Samuel, S.M.S. Nagendra, M.P. Maiya, Impact of indoor heat load and natural ventilation on thermal comfort of radiant cooling system: An experimental study, Energy Built Environ. (2022). https://doi.org/10.1016/j.enbenv.2022.04.003.

[60] C. Díaz-López, A. Serrano-Jiménez, K. Verichev, Á. Barrios-Padura, Passive cooling strategies to optimise sustainability and environmental ergonomics in Mediterranean schools based on a critical review, Build. Environ. 221 (2022) 109297. https://doi.org/10.1016/j.buildenv.2022.109297.

[61] B. Widera, Comparative analysis of user comfort and thermal performance of six types of vernacular dwellings as the first step towards climate resilient, sustainable and bioclimatic architecture in western sub-Saharan Africa, Renew. Sustain. Energy Rev. 140 (2021)

110736. https://doi.org/10.1016/j.rser.2021.110736.

[62] M.M. Osman, H. Sevinc, Adaptation of climate-responsive building design strategies and resilience to climate change in the hot/arid region of Khartoum, Sudan, Sustain. Cities Soc. 47 (2019) 101429. https://doi.org/10.1016/j.scs.2019.101429.

[63] H. Hersbach, B. Bell, P. Berrisford, S. Hirahara, A. Horányi, J. Muñoz-Sabater, J. Nicolas, C. Peubey, R. Radu, D. Schepers, A. Simmons, C. Soci, S. Abdalla, X. Abellan, G. Balsamo, P. Bechtold, G. Biavati, J. Bidlot, M. Bonavita, G. De Chiara, P. Dahlgren, D. Dee, M. Diamantakis, R. Dragani, J. Flemming, R. Forbes, M. Fuentes, A. Geer, L. Haimberger, S. Healy, R.J. Hogan, E. Hólm, M. Janisková, S. Keeley, P. Laloyaux, P. Lopez, C. Lupu, G. Radnoti, P. de Rosnay, I. Rozum, F. Vamborg, S. Villaume, J.N. Thépaut, The ERA5 global reanalysis, Q. J. R. Meteorol. Soc. 146 (2020) 1999–2049. https://doi.org/10.1002/qj.3803.

[64] Y. Sianturi, Marjuki, K. Sartika, Evaluation of ERA5 and MERRA2 reanalyses to estimate solar irradiance using ground observations over Indonesia region, AIP Conf. Proc. 2223 (2020). https://doi.org/10.1063/5.0000854.

[65] B. Givoni, Indoor temperature reduction by passive cooling systems, Sol. Energy. 85 (2011) 1692–1726. https://doi.org/10.1016/j.solener.2009.10.003.

[66] B. Givoni, Comfort, climate analysis and building design guidelines, Energy Build. 18 (1992) 11–23. https://doi.org/10.1016/0378-7788(92)90047-K.

[67] F. Manzano-Agugliaro, F.G. Montoya, A. Sabio-Ortega, A. García-Cruz, Review of bioclimatic architecture strategies for achieving thermal comfort, Renew. Sustain. Energy Rev. 49 (2015) 736–755. https://doi.org/10.1016/j.rser.2015.04.095.

[68] S. Shazlyn Milleana, S. Ismail, C.M.N. Siti Mariana, A. Norhaiza, An efficient method to improve the clustering performance using hybrid robust principal component analysis-spectral biclustering in rainfall patterns identification, IAES Int. J. Artif. Intell. 8 (2019) 237–243. https://doi.org/10.11591/ijai.v8.i3.pp237-243.

[69] M.A.R. Hamed, Application of surface water quality classification models using principal components analysis and cluster analysis, Water Energy Int. 62r (2019) 54–62. https://doi.org/10.4236/gep.2019.76003.

[70] N. Sadiq, Principal Component and Clustering Analyses for Seasonal Classification of Karachi, Pakistan J. Meteorol. 7 (2002) 9–16.

[71] H.F. Kaiser, The varimax criterion for analytic rotation in factor analysis, Psychometrika. 23 (1958) 187–200. https://doi.org/10.1007/BF02289233.

[72] B.A. Malmgren, A. Winter, Climate zonation in Puerto Rico based on principal components analysis and an artificial neural network, J. Clim. 12 (1999) 977–985. https://doi.org/10.1175/1520-0442(1999)012<0977:CZIPRB>2.0.CO;2.

[73] K. Panchabikesan, K. Vellaisamy, V. Ramalingam, Passive cooling potential in buildings under various climatic conditions in India, Renew. Sustain. Energy Rev. 78 (2017) 1236–1252. https://doi.org/10.1016/j.rser.2017.05.030.

[74] O.M. Eludoyin, I.O. Adelekan, R. Webster, A.O. Eludoyin, Air temperature, relative humidity, climate regionalization and thermal comfort of Nigeria, Int. J. Climatol. 34 (2014) 2000–2018. https://doi.org/10.1002/joc.3817.

[75] A.K. Shrestha, A. Thapa, H. Gautam, Solar radiation, air temperature, relative humidity, and dew point study: Damak, jhapa, Nepal, Int. J. Photoenergy. 2019 (2019). https://doi.org/10.1155/2019/8369231.

[76] M.S. Naizghi, T.B.M.J. Ouarda, Teleconnections and analysis of long-term wind speed variability in the UAE, Int. J. Climatol. 37 (2017) 230–248. https://doi.org/10.1002/joc.4700.

[77] N.R.M. Sakiyama, J.C. Carlo, J. Frick, H. Garrecht, Perspectives of naturally ventilated buildings: A review, Renew. Sustain. Energy Rev. 130 (2020) 109933. https://doi.org/10.1016/j.rser.2020.109933.

[78] P. Shakya, G. Ng, X. Zhou, Y.W. Wong, S. Dubey, S. Qian, Thermal comfort and energy analysis of a hybrid cooling system by coupling natural ventilation with radiant and indirect evaporative cooling, Energies. 14 (2021). https://doi.org/10.3390/en14227825.

[79] K. Hiyama, Regional classification maps for engineered natural ventilation design of office buildings in Japan, Japan Archit. Rev. 4 (2021) 253–261. https://doi.org/10.1002/2475-8876.12201.

[80] T. Kubota, D.T.H. Chyee, S. Ahmad, The effects of night ventilation technique on indoor thermal environment for residential buildings in hot-humid climate of Malaysia, Energy Build. 41 (2009) 829–839. https://doi.org/10.1016/j.enbuild.2009.03.008.

[81] E. Solgi, Z. Hamedani, R. Fernando, H. Skates, N.E. Orji, A literature review of night ventilation strategies in buildings, Energy Build. 173 (2018) 337–352.

https://doi.org/10.1016/j.enbuild.2018.05.052.

[82] J.P. Bijarniya, J. Sarkar, P. Maiti, Review on passive daytime radiative cooling: Fundamentals, recent researches, challenges and opportunities, Renew. Sustain. Energy Rev. 133 (2020) 110263. https://doi.org/10.1016/j.rser.2020.110263.

[83] Suhendri, M. Hu, Y. Su, J. Darkwa, S. Riffat, Implementation of passive radiative cooling technology in buildings: A review, Buildings. 10 (2020) 1–28. https://doi.org/10.3390/buildings10120215.

[84] J.R. Camargo, C.D. Ebinuma, S. Cardoso, Three Methods To Evaluate the Use of Evaporative Cooling for Human Thermal Comfort, Rev. Eng. Térmica. 5 (2006) 09. https://doi.org/10.5380/reterm.v5i2.61846.

[85] A.H.A. Mahmoud, An analysis of bioclimatic zones and implications for design of outdoor built environments in Egypt, Build. Environ. 46 (2011) 605–620. https://doi.org/10.1016/j.buildenv.2010.09.007.

[86] M.K. Singh, S. Mahapatra, S.K. Atreya, Development of bio-climatic zones in north-east India, Energy Build. 39 (2007) 1250–1257. https://doi.org/10.1016/j.enbuild.2007.01.015.

[87] O. Rakoto-Joseph, F. Garde, M. David, L. Adelard, Z.A. Randriamanantany, Development of climatic zones and passive solar design in Madagascar, Energy Convers. Manag. 50 (2009) 1004–1010. https://doi.org/10.1016/j.enconman.2008.12.011.

[88] C. Díaz-López, J. Jódar, K. Verichev, M.L. Rodríguez, M. Carpio, M. Zamorano, Dynamics of changes in climate zones and building energy demand. A case study in spain, Appl. Sci. 11 (2021). https://doi.org/10.3390/app11094261.

[89] L. Bai, S. Wang, Definition of new thermal climate zones for building energy efficiency response to the climate change during the past decades in China, Energy. 170 (2019) 709–719. https://doi.org/10.1016/j.energy.2018.12.187.

[90] L. Bai, L. Yang, B. Song, N. Liu, A new approach to develop a climate classification for building energy efficiency addressing Chinese climate characteristics, Energy. 195 (2020) 116982. https://doi.org/10.1016/j.energy.2020.116982.

[91] M.N. Mistry, Historical global gridded degree-days: A high-spatial resolution database of CDD and HDD, Geosci. Data J. 6 (2019) 214–221. https://doi.org/10.1002/gdj3.83.

[92] A. Prieto, U. Knaack, T. Auer, T. Klein, COOLFACADE: State-of-the-art review and evaluation of solar cooling technologies on their potential for façade integration, Renew.

Sustain. Energy Rev. 101 (2019) 395–414. https://doi.org/10.1016/j.rser.2018.11.015.

[93] N. Artmann, H. Manz, P. Heiselberg, Climatic potential for passive cooling of buildings by night-time ventilation in Europe, Appl. Energy. 84 (2007) 187–201. https://doi.org/10.1016/j.apenergy.2006.05.004.

[94] J.W. Axley, S.J. Emmerich, A Method to Assess the Suitability of a Climate for Natural Ventilation of Commercial Buildings, Indoor Air 2002, 9th Int. Conf. Indoor Air Qual. Clim. 2 (2002) 854–859.

[95] A.R. Dehghani-Sanij, M. Soltani, K. Raahemifar, A new design of wind tower for passive ventilation in buildings to reduce energy consumption in windy regions, Renew. Sustain. Energy Rev. 42 (2015) 182–195. https://doi.org/10.1016/j.rser.2014.10.018.

[96] D. Etheridge, A perspective on fifty years of natural ventilation research, Build. Environ. 91 (2015) 51–60. https://doi.org/10.1016/j.buildenv.2015.02.033.

[97] C. Zeng, S. Liu, A. Shukla, A review on the air-to-air heat and mass exchanger technologies for building applications, Renew. Sustain. Energy Rev. 75 (2017) 753–774. https://doi.org/10.1016/j.rser.2016.11.052.

[98] D.H.W. Li, J.C. Lam, C.C.S. Lau, A new approach for predicting vertical global solar irradiance, Renew. Energy. 25 (2002) 591–606. https://doi.org/10.1016/S0960-1481(01)00095-7.

[99] D.S. Lee, J.H. Jo, Application of simple sky and building models for the evaluation of solar irradiance distribution at indoor locations in buildings, Build. Environ. 197 (2021) 107840. https://doi.org/10.1016/j.buildenv.2021.107840.

[100] M. González-Torres, L. Pérez-Lombard, J.F. Coronel, I.R. Maestre, D. Yan, A review on buildings energy information: Trends, end-uses, fuels and drivers, Energy Reports. 8 (2022) 626–637. https://doi.org/10.1016/j.egyr.2021.11.280.

[101] C. Marino, A. Nucara, M. Pietrafesa, Thermal comfort in indoor environment: Effect of the solar radiation on the radiant temperature asymmetry, Sol. Energy. 144 (2017) 295–309. https://doi.org/10.1016/j.solener.2017.01.014.

[102] Q. Dong, S. Li, C. Han, Numerical and experimental study of the effect of solar radiation on thermal comfort in a radiant heating system, J. Build. Eng. 32 (2020) 101497. https://doi.org/10.1016/j.jobe.2020.101497.

[103] J. Zhou, Y. Wu, G. Yan, Generation of typical solar radiation year for China, Renew.

Energy. 31 (2006) 1972–1985. https://doi.org/10.1016/j.renene.2005.09.013.

[104] D. Setiawan, M.A. Azmi, Solar Radiation Study of Office Building Shapes at a Bussiness District in South Jakarta, IOP Conf. Ser. Earth Environ. Sci. 794 (2021). https://doi.org/10.1088/1755-1315/794/1/012181.

[105] A. Hashemi, N. Khatami, Effects of Solar Shading on Thermal Comfort in Low-income Tropical Housing, Energy Procedia. 111 (2017) 235–244. https://doi.org/10.1016/j.egypro.2017.03.025.

[106] A.L.S. Chan, T.T. Chow, Evaluation of Overall Thermal Transfer Value (OTTV) for commercial buildings constructed with green roof, Appl. Energy. 107 (2013) 10–24. https://doi.org/10.1016/j.apenergy.2013.02.010.

[107] A. Sepúlveda, S.S. Seyed Salehi, F. De Luca, M. Thalfeldt, Solar radiation-based method for early design stages to balance daylight and thermal comfort in office buildings, J. Build. Eng. (2023). https://doi.org/10.1016/j.foar.2023.07.001.

[108] Y. He, E.S. Lin, C.L. Tan, Z. Yu, P.Y. Tan, N.H. Wong, Model development of Roof Thermal Transfer Value (RTTV) for green roof in tropical area: A case study in Singapore, Build. Environ. 203 (2021) 108101. https://doi.org/10.1016/j.buildenv.2021.108101.

[109] R.L. Hwang, W.A. Chen, Identifying relative importance of solar design determinants on office building façade for cooling loads and thermal comfort in hot-humid climates, Build. Environ. 226 (2022). https://doi.org/10.1016/j.buildenv.2022.109684.

[110] B. Song, L. Bai, L. Yang, Analysis of the long-term effects of solar radiation on the indoor thermal comfort in office buildings, Energy. 247 (2022) 123499. https://doi.org/10.1016/j.energy.2022.123499.

[111] V. Moron, A.W. Robertson, J.H. Qian, M. Ghil, Weather types across the Maritime Continent: From the diurnal cycle to interannual variations, Front. Environ. Sci. 2 (2015) 1–19. https://doi.org/10.3389/fenvs.2014.00065.

[112] Q. Cao, Y. Liu, K. Lyu, Y. Yu, D.H.W. Li, L. Yang, Solar radiation zoning and daily global radiation models for regions with only surface meteorological measurements in China, Energy Convers. Manag. 225 (2020) 113447. https://doi.org/10.1016/j.enconman.2020.113447.

[113] W.A. Friess, K. Rakhshan, A review of passive envelope measures for improved building

energy efficiency in the UAE, Renew. Sustain. Energy Rev. 72 (2017) 485–496. https://doi.org/10.1016/j.rser.2017.01.026.

[114] Q. Mao, L. Luo, Experimental research of solar infrared spectral radiation in Wuhan, China, Infrared Phys. Technol. 125 (2022) 104306. https://doi.org/10.1016/j.infrared.2022.104306.

[115] D. Tschopp, A.R. Jensen, J. Dragsted, P. Ohnewein, S. Furbo, Measurement and modeling of diffuse irradiance masking on tilted planes for solar engineering applications, Sol. Energy. 231 (2022) 365–378. https://doi.org/10.1016/j.solener.2021.10.083.

[116] Y. Ji, J. Song, P. Shen, A review of studies and modelling of solar radiation on human thermal comfort in outdoor environment, Build. Environ. 214 (2022) 108891. https://doi.org/10.1016/j.buildenv.2022.108891.

[117] S.B. Sadineni, S. Madala, R.F. Boehm, Passive building energy savings: A review of building envelope components, Renew. Sustain. Energy Rev. 15 (2011) 3617–3631. https://doi.org/10.1016/j.rser.2011.07.014.

[118] E.M. Saber, I. Chaer, A. Gillich, B.G. Ekpeti, Review of intelligent control systems for natural ventilation as passive cooling strategy for UK buildings and similar climatic conditions, Energies. 14 (2021). https://doi.org/10.3390/en14154388.

[119] J.F. Escobedo, E.N. Gomes, A.P. Oliveira, J. Soares, Modeling hourly and daily fractions of UV, PAR and NIR to global solar radiation under various sky conditions at Botucatu, Brazil, Appl. Energy. 86 (2009) 299–309. https://doi.org/10.1016/j.apenergy.2008.04.013.

[120] N.B. Mohamad, A.C. Lai, B.H. Lim, A case study in the tropical region to evaluate univariate imputation methods for solar irradiance data with different weather types, Sustain. Energy Technol. Assessments. 50 (2022) 101764. https://doi.org/10.1016/j.seta.2021.101764.

[121] H. Morf, A validation frame for deterministic solar irradiance forecasts, Renew. Energy. 180 (2021) 1210–1221. https://doi.org/10.1016/j.renene.2021.08.032.

[122] N. Lindsay, Q. Libois, J. Badosa, A. Migan-Dubois, V. Bourdin, Errors in PV power modelling due to the lack of spectral and angular details of solar irradiance inputs, Sol. Energy. 197 (2020) 266–278. https://doi.org/10.1016/j.solener.2019.12.042.

[123] Q. Mao, L. Luo, Experimental research of solar infrared spectral radiation in Wuhan, China, Infrared Phys. Technol. 125 (2022) 104306.

https://doi.org/10.1016/j.infrared.2022.104306.

[124] D.H.W. Li, N.T.C. Chau, K.K.W. Wan, Predicting daylight illuminance and solar irradiance on vertical surfaces based on classified standard skies, Energy. 53 (2013) 252–258. https://doi.org/10.1016/j.energy.2013.02.049.

[125] I.D. Gede, A. Pandawana, T. Tanaka, T. Osawa, A.R. As-syakur, M. Sudiana, Characteristics of Diurnal Rainfall Cycle Over Java as seen by the TRMM Precipitation Radar, 3 (2019) 17–25.

[126] S. Luo, H. Li, Y. Mao, C. Yang, Experimental research on a novel sun shading & solar energy collecting coupling device for inpatient building in hot summer and cold winter climate zone in China, Appl. Therm. Eng. 142 (2018) 89–99. https://doi.org/10.1016/j.applthermaleng.2018.06.081.

[127] S. Lestari, A. King, C. Vincent, D. Karoly, A. Protat, Seasonal dependence of rainfall extremes in and around Jakarta, Indonesia, Weather Clim. Extrem. 24 (2019) 100202. https://doi.org/10.1016/j.wace.2019.100202.

[128] C.A. Gueymard, J.M. Bright, D. Lingfors, A. Habte, M. Sengupta, A posteriori clear-sky identification methods in solar irradiance time series: Review and preliminary validation using sky imagers, Renew. Sustain. Energy Rev. 109 (2019) 412–427. https://doi.org/10.1016/j.rser.2019.04.027.

[129] N. Singh, S. Jena, C.K. Panigrahi, A novel application of Decision Tree classifier in solar irradiance prediction, Mater. Today Proc. 58 (2022) 316–323. https://doi.org/10.1016/j.matpr.2022.02.198.

[130] A.M. Omer, Renewable building energy systems and passive human comfort solutions, Renew. Sustain. Energy Rev. 12 (2008) 1562–1587. https://doi.org/10.1016/j.rser.2006.07.010.

[131] M. Santamouris, K. Vasilakopoulou, Present and future energy consumption of buildings: Challenges and opportunities towards decarbonisation, E-Prime - Adv. Electr. Eng. Electron. Energy. 1 (2021) 100002. https://doi.org/10.1016/j.prime.2021.100002.

[132] L. Pérez-Lombard, J. Ortiz, C. Pout, A review on buildings energy consumption information, Energy Build. 40 (2008) 394–398. https://doi.org/10.1016/j.enbuild.2007.03.007.

[133] H. Zang, Q. Xu, H. Bian, Generation of typical solar radiation data for different climates

of China, Energy. 38 (2012) 236–248. https://doi.org/10.1016/j.energy.2011.12.008.

[134] E. Afrifa-Yamoah, U.A. Mueller, S.M. Taylor, A.J. Fisher, Missing data imputation of high-resolution temporal climate time series data, Meteorol. Appl. 27 (2020) 1–18. https://doi.org/10.1002/met.1873.

[135] N. Salmani-Dehaghi, N. Samani, Development of bias-correction PERSIANN-CDR models for the simulation and completion of precipitation time series, Atmos. Environ. 246 (2021) 117981. https://doi.org/10.1016/j.atmosenv.2020.117981.

[136] M. Lompar, B. Lalić, L. Dekić, M. Petrić, Filling gaps in hourly air temperature data using debiased ERA5 data, Atmosphere (Basel). 10 (2019) 11–13. https://doi.org/10.3390/atmos10010013.

[137] J. Zhang, L. Zhao, S. Deng, W. Xu, Y. Zhang, A critical review of the models used to estimate solar radiation, Renew. Sustain. Energy Rev. 70 (2017) 314–329. https://doi.org/10.1016/j.rser.2016.11.124.

[138] S. Saha, S. Moorthi, X. Wu, J. Wang, S. Nadiga, P. Tripp, D. Behringer, Y.T. Hou, H.Y. Chuang, M. Iredell, M. Ek, J. Meng, R. Yang, M.P. Mendez, H. Van Den Dool, Q. Zhang, W. Wang, M. Chen, E. Becker, The NCEP climate forecast system version 2, J. Clim. 27 (2014) 2185–2208. https://doi.org/10.1175/JCLI-D-12-00823.1.

[139] R. Gelaro, W. McCarty, M.J. Suárez, R. Todling, A. Molod, L. Takacs, C.A. Randles, A. Darmenov, M.G. Bosilovich, R. Reichle, K. Wargan, L. Coy, R. Cullather, C. Draper, S. Akella, V. Buchard, A. Conaty, A.M. da Silva, W. Gu, G.K. Kim, R. Koster, R. Lucchesi, D. Merkova, J.E. Nielsen, G. Partyka, S. Pawson, W. Putman, M. Rienecker, S.D. Schubert, M. Sienkiewicz, B. Zhao, The modern-era retrospective analysis for research and applications, version 2 (MERRA-2), J. Clim. 30 (2017) 5419–5454. https://doi.org/10.1175/JCLI-D-16-0758.1.

[140] M. Roth, Evaluation of climate reanalysis data for use in ASHRAE Applications, ASHRAE Research Project RP-1745, 2019.

[141] M.C. Kotti, A.A. Argiriou, A. Kazantzidis, Estimation of direct normal irradiance from measured global and corrected diffuse horizontal irradiance, Energy. 70 (2014) 382–392. https://doi.org/10.1016/j.energy.2014.04.012.

[142] G. Brooke Anderson, M.L. Bell, R.D. Peng, Methods to calculate the heat index as an exposure metric in environmental health research, Environ. Health Perspect. 121 (2013)

1111–1119. https://doi.org/10.1289/ehp.1206273.

[143] N. Farhani, J. Carreau, Z. Kassouk, B. Mougenot, M. Le Page, Z. Lili-Chabaane, R. Zitouna-Chebbi, G. Boulet, Regional sub-daily stochastic weather generator based on reanalyses for surface water stress estimation in central Tunisia, Environ. Model. Softw. 155 (2022) 105448. https://doi.org/10.1016/j.envsoft.2022.105448.

[144] M.L. Tan, A.M. Armanuos, I. Ahmadianfar, V. Demir, S. Heddam, A.M. Al-Areeq, S.I. Abba, B. Halder, H. Cagan Kilinc, Z.M. Yaseen, Evaluation of NASA POWER and ERA5-Land for estimating tropical precipitation and temperature extremes, J. Hydrol. 624 (2023) 129940. https://doi.org/10.1016/j.jhydrol.2023.129940.

[145] R. Urraca, T. Huld, A. Gracia-Amillo, F.J. Martinez-de-Pison, F. Kaspar, A. Sanz-Garcia, Evaluation of global horizontal irradiance estimates from ERA5 and COSMO-REA6 reanalyses using ground and satellite-based data, Sol. Energy. 164 (2018) 339–354. https://doi.org/10.1016/j.solener.2018.02.059.

[146] A.J. Cannon, S.R. Sobie, T.Q. Murdock, Bias correction of GCM precipitation by quantile mapping: How well do methods preserve changes in quantiles and extremes?, J. Clim. 28 (2015) 6938–6959. https://doi.org/10.1175/JCLI-D-14-00754.1.

[147] F.S. Hafez, B. Sa'di, M. Safa-Gamal, Y.H. Taufiq-Yap, M. Alrifaey, M. Seyedmahmoudian, A. Stojcevski, B. Horan, S. Mekhilef, Energy Efficiency in Sustainable Buildings: A Systematic Review with Taxonomy, Challenges, Motivations, Methodological Aspects, Recommendations, and Pathways for Future Research, Energy Strateg. Rev. 45 (2023) 101013. https://doi.org/10.1016/j.esr.2022.101013.

[148] Y. Fang, S. Cho, Design optimization of building geometry and fenestration for daylighting and energy performance, Sol. Energy. 191 (2019) 7–18. https://doi.org/10.1016/j.solener.2019.08.039.

[149] J. Shen, B. Krietemeyer, A. Bartosh, Z. Gao, J. Zhang, Green Design Studio: A modular-based approach for high-performance building design, Build. Simul. 14 (2021) 241–268. https://doi.org/10.1007/s12273-020-0728-9.

[150] E. Cuerda, O. Guerra-Santin, J.J. Sendra, F.J. Neila, Understanding the performance gap in energy retrofitting: Measured input data for adjusting building simulation models, Energy Build. 209 (2020) 109688. https://doi.org/10.1016/j.enbuild.2019.109688.

[151] M. Hosseini, A. Bigtashi, B. Lee, A systematic approach in constructing typical

meteorological year weather files using machine learning, Energy Build. 226 (2020) 110375. https://doi.org/10.1016/j.enbuild.2020.110375.

[152] X. Fan, A method for the generation of typical meteorological year data using ensemble empirical mode decomposition for different climates of China and performance comparison analysis, Energy. 240 (2022) 122822. https://doi.org/10.1016/j.energy.2021.122822.

[153] J. Yuan, P. Huang, J. Chai, Development of a calibrated typical meteorological year weather file in system design of zero-energy building for performance improvements, Energy. 259 (2022) 125031. https://doi.org/10.1016/j.energy.2022.125031.

[154] T. Kalamees, K. Jylhä, H. Tietäväinen, J. Jokisalo, S. Ilomets, R. Hyvönen, S. Saku, Development of weighting factors for climate variables for selecting the energy reference year according to the en ISO 15927-4 standard, Energy Build. 47 (2012) 53–60. https://doi.org/10.1016/j.enbuild.2011.11.031.

[155] K. Lee, H. Yoo, G.J. Levermore, Generation of typical weather data using the ISO Test Reference Year (TRY) method for major cities of South Korea, Build. Environ. 45 (2010) 956–963. https://doi.org/10.1016/j.buildenv.2009.10.002.

[156] S. Kim, D. Zirkelbach, H.M. Künzel, J.H. Lee, J. Choi, Development of test reference year using ISO 15927-4 and the influence of climatic parameters on building energy performance, Build. Environ. 114 (2017) 374–386. https://doi.org/10.1016/j.buildenv.2016.12.037.

[157] G. Pernigotto, A. Prada, D. Cóstola, A. Gasparella, J.L.M. Hensen, Multi-year and reference year weather data for building energy labelling in north Italy climates, Energy Build. 72 (2014) 62–72. https://doi.org/10.1016/j.enbuild.2013.12.012.

[158] C.Y. Siu, Z. Liao, Is building energy simulation based on TMY representative: A comparative simulation study on doe reference buildings in Toronto with typical year and historical year type weather files, Energy Build. 211 (2020). https://doi.org/10.1016/j.enbuild.2020.109760.

[159] E.C. Hall, I J; Prairie, R R; Anderson, H E; Boes, Generation of a typical meteorological year, in: Conf. Anal. Sol. Heat. Cool. San Diego, CA, USA, 27 Jun 1978, 1978. https://www.osti.gov/biblio/7013202.

[160] M.A. Hassan, A. Khalil, M. Abubakr, Selection methodology of representative

meteorological days for assessment of renewable energy systems, Renew. Energy. 177 (2021) 34–51. https://doi.org/10.1016/j.renene.2021.05.124.

[161] K. Kulesza, Comparison of typical meteorological year and multi-year time series of solar conditions for Belsk, central Poland, Renew. Energy. 113 (2017) 1135–1140. https://doi.org/10.1016/j.renene.2017.06.087.

[162] L. Yang, J.C. Lam, J. Liu, C.L. Tsang, Building energy simulation using multi-years and typical meteorological years in different climates, Energy Convers. Manag. 49 (2008) 113–124. https://doi.org/10.1016/j.enconman.2007.05.004.

[163] A.L.S. Chan, Generation of typical meteorological years using genetic algorithm for different energy systems, Renew. Energy. 90 (2016) 1–13. https://doi.org/10.1016/j.renene.2015.12.052.

[164] L. Yang, K.K.W. Wan, D.H.W. Li, J.C. Lam, A new method to develop typical weather years in different climates for building energy use studies, Energy. 36 (2011) 6121–6129. https://doi.org/10.1016/j.energy.2011.07.053.

[165] W. Marion, K. Urban, User ' s Manual for Radiation Data Base, (1995). https://www.osti.gov/biblio/87130.

[166] A. Habte, A. Lopez, M. Sengupta, S. Wilcox, Temporal and Spatial Comparison of Gridded TMY, TDY, and TGY Data Sets, Tech. Rep. TP-5D00-60886. (2014) 1–30. http://www.osti.gov/scitech/biblio/1126297.

[167] M. Sengupta, Y. Xie, A. Lopez, A. Habte, G. Maclaurin, J. Shelby, The National Solar Radiation Data Base (NSRDB), Renew. Sustain. Energy Rev. 89 (2018) 51–60. https://doi.org/10.1016/j.rser.2018.03.003.

[168] S. Wilcox, W. Marion, Users manual for TMY3 data sets, Renew. Energy. (2008) 51. http://scholar.google.com/scholar?hl=en&btnG=Search&q=intitle:Users+Manual+for+TMY3+Data+Sets+Users+Manual+for+TMY3+Data+Sets#1%5Cnhttp://scholar.google.com/scholar?hl=en&btnG=Search&q=intitle:May.?Users+manual+for+TMY3+data+sets+users+manual+for+TMY3+dat.

[169] Y.J. Huang, F. Su, D. Seo, M. Krarti, Development of 3012 IWEC2 weather files for international locations (RP-1477), ASHRAE Trans. 120 (2014) 340–355.

[170] A. Smith, N. Lott, R. Vose, The integrated surface database: Recent developments and partnerships, Bull. Am. Meteorol. Soc. 92 (2011) 704–708.

https://doi.org/10.1175/2011BAMS3015.1.

[171] I. Standard, INTERNATIONAL STANDARD buildings — Calculation and presentation, 2009 (2009).

[172] K. Skeiker, B.A. Ghani, A software tool for the creation of a typical meteorological year, Renew. Energy. 34 (2009) 544–554. https://doi.org/10.1016/j.renene.2008.05.046.

[173] D. Schwede, Y. Wang, Reference weather datasets for building simulation in Vietnam considering thermal and hygrothermal characteristics, Build. Environ. 220 (2022) 109022. https://doi.org/10.1016/j.buildenv.2022.109022.

[174] F.S. Alargt, Y.M. Khalifa, A.H. Kharaz, Generation of a TMY for Tripoli City Using the Finkelstein-Schafer Statistical Method, IECON Proc. (Industrial Electron. Conf. 2021-Octob (2021). https://doi.org/10.1109/IECON48115.2021.9589177.

[175] M. Petrakis, S. Lykoudis, P. Kassomenos, A software tool for the creation of a typical meteorological year, Environ. Softw. 11 (1996) 221–227. https://doi.org/10.1016/S0266-9838(96)00006-8.

[176] M. Petrakis, H.D. Kambezidis, S. Lykoudis, A.D. Adamopoulos, P. Kassomenos, I.M. Michaelides, S.A. Kalogirou, G. Roditis, I. Chrysis, A. Hadjigianni, Generation of a "typical meteorological year" for Nicosia, Cyprus, Renew. Energy. 13 (1998) 381–388. https://doi.org/10.1016/S0960-1481(98)00014-7.

[177] S.A. Kalogirou, Generation of typical meteorological year (TMY-2) for Nicosia, Cyprus, Renew. Energy. 28 (2003) 2317–2334. https://doi.org/10.1016/S0960-1481(03)00131-9.

[178] K. Skeiker, Generation of a typical meteorological year for Damascus zone using the Filkenstein-Schafer statistical method, Energy Convers. Manag. 45 (2004) 99–112. https://doi.org/10.1016/S0196-8904(03)00106-7.

[179] Serpil Yilmaz, Ismail Ekmekci, The Generation of Typical Meteorological Year and Climatic Database of Turkey for the Energy Analysis of Buildings, J. Environ. Sci. Eng. A. 6 (2017) 370–376. https://doi.org/10.17265/2162-5298/2017.07.005.

[180] S. Pusat, I. Ekmekçi, M.T. Akkoyunlu, Generation of typical meteorological year for different climates of Turkey, Renew. Energy. 75 (2015) 144–151. https://doi.org/10.1016/j.renene.2014.09.039.

[181] L. Yang, J.C. Lam, J. Liu, Analysis of typical meteorological years in different climates of China, Energy Convers. Manag. 48 (2007) 654–668.

https://doi.org/10.1016/j.enconman.2006.05.016.

[182] Y. Jiang, Generation of typical meteorological year for different climates of China, Energy. 35 (2010) 1946–1953. https://doi.org/10.1016/j.energy.2010.01.009.

[183] J.C. Lam, S.C.M. Hui, A.L.S. Chan, A statistical approach to the development of a typical meteorological year for hong kong, Archit. Sci. Rev. 39 (1996) 201–209. https://doi.org/10.1080/00038628.1996.9696818.

[184] A.L.S. Chan, T.T. Chow, S.K.F. Fong, J.Z. Lin, Generation of a typical meteorological year for Hong Kong, Energy Convers. Manag. 47 (2006) 87–96. https://doi.org/10.1016/j.enconman.2005.02.010.

[185] O.S. Ohunakin, M.S. Adaramola, O.M. Oyewola, R.O. Fagbenle, Generation of a typical meteorological year for north-east, Nigeria, Appl. Energy. 112 (2013) 152–159. https://doi.org/10.1016/j.apenergy.2013.05.072.

[186] S.O. Oyedepo, J.A. Oyebanji, S.N. Ukponu, O. Kilanko, P.O. Babalola, O.S.I. Fayomi, J.O. Dirisu, C.O. Olawole, R.O. Leramo, I.S. Dunmade, U.K. Efemwenkiekie, O.O. Shopeju, Generation of Typical Meteorological Year Data for a City in South-Western Nigeria, IOP Conf. Ser. Mater. Sci. Eng. 1107 (2021) 012130. https://doi.org/10.1088/1757-899x/1107/1/012130.

[187] T.E. Patchali, O.O. Ajide, O.J. Matthew, T.A.O. Salau, O.M. Oyewola, Generation of meteorological year for the assessment of photovoltaic systems performance in Togo, West Africa, Sci. African. 16 (2022) e01171. https://doi.org/10.1016/j.sciaf.2022.e01171.

[188] F. Bre, V.D. Fachinotti, Generation of typical meteorological years for the Argentine Littoral Region, Energy Build. 129 (2016) 432–444. https://doi.org/10.1016/j.enbuild.2016.08.006.

[189] A. Ebrahimpour, M. Maerefat, A method for generation of typical meteorological year, Energy Convers. Manag. 51 (2010) 410–417. https://doi.org/10.1016/j.enconman.2009.10.002.

[190] A. Couce-Casanova, J. de Dios Rodríguez-García, M.I. Lamas, J.A. Orosa, A New Way to Obtain Climate Files in Areas with the Presence of Microclimates by Applying the Sandia Method: A Galician Case Study, Climate. 10 (2022). https://doi.org/10.3390/cli10100140.

[191] S.A.M. Said, H.M. Kadry, Generation of representative weather-Year data for Saudi Arabia, Appl. Energy. 48 (1994) 131–136. https://doi.org/10.1016/0306-2619(94)90019-1.

[192] I.A. Rahman, J. Dewsbury, Selection of typical weather data (test reference years) for Subang, Malaysia, Build. Environ. 42 (2007) 3636–3641. https://doi.org/10.1016/j.buildenv.2006.10.004.

[193] E. Barreira, M.L. Simões, J.M.P.Q. Delgado, I. Sousa, Procedures in the construction of a test reference year for Porto-Portugal and implications for hygrothermal simulation, Sustain. Cities Soc. 32 (2017) 397–410. https://doi.org/10.1016/j.scs.2017.04.013.

[194] W.R. Petrie, M. McClintock, Determining typical weather for use in solar energy simulations, Sol. Energy. 21 (1978) 55–59. https://doi.org/10.1016/0038-092X(78)90116-0.

[195] M.A. Mosalam Shaltout, M.T.Y. Tadros, Typical solar radiation year for Egypt, Renew. Energy. 4 (1994) 387–393. https://doi.org/10.1016/0960-1481(94)90045-0.

[196] A. Ecevit, B.G. Akinoglu, B. Aksoy, Generation of a typical meteorological year using sunshine duration data, Energy. 27 (2002) 947–954. https://doi.org/10.1016/S0360-5442(02)00029-4.

[197] A.M. Realpe, C. Vernay, S. Pitaval, C. Lenoir, P. Blanc, Benchmarking of Five Typical Meteorological Year Datasets Dedicated to Concentrated-PV Systems, Energy Procedia. 97 (2016) 108–115. https://doi.org/10.1016/j.egypro.2016.10.031.

[198] H.D. Kambezidis, The solar radiation climate of Greece, Climate. 9 (2021) 1–19. https://doi.org/10.3390/cli9120183.

[199] H.A. Al-Hinai, S.M. Al-Alawi, Typical solar radiation data for Oman, Appl. Energy. 52 (1995) 153–163. https://doi.org/10.1016/0306-2619(95)00035-Q.

[200] K.T. Huang, Identifying a suitable hourly solar diffuse fraction model to generate the typical meteorological year for building energy simulation application, Renew. Energy. 157 (2020) 1102–1115. https://doi.org/10.1016/j.renene.2020.05.094.

[201] B. Andersen, S. Eidorff, H. Lund, E. Pedersen, S. Rosenørn, O. Valbjørn, Meteorological Data for Design of Building and Installation: A Reference Year (extract), Rep. No 66, 2nd Ed. (1977).

[202] S.E. H. Lund, Selection methods for production of test reference years (meteorology)., (1981).

[203] R. Festa, C.F. Ratto, Proposal of a numerical procedure to select Reference Years, Sol. Energy. 50 (1993) 9–17. https://doi.org/10.1016/0038-092X(93)90003-7.

[204] Q. Zhang, Development of the typical meteorological database for Chinese locations, Energy Build. 38 (2006) 1320–1326. https://doi.org/10.1016/j.enbuild.2006.04.003.

[205] F. Song, Q. Zhu, R. Wu, Y. Jiang, A. Xiong, B. Wang, Y. Zhu, Q. Li, Meteorological data set for building thermal environment analysis of china, IBPSA 2007 - Int. Build. Perform. Simul. Assoc. 2007. (2007) 9–16.

[206] H. Li, J. Huang, Y. Hu, S. Wang, J. Liu, L. Yang, A new TMY generation method based on the entropy-based TOPSIS theory for different climatic zones in China, Energy. 231 (2021) 120723. https://doi.org/10.1016/j.energy.2021.120723.

[207] Y. Arima, R. Ooka, H. Kikumoto, Proposal of typical and design weather year for building energy simulation, Energy Build. 139 (2017) 517–524. https://doi.org/10.1016/j.enbuild.2017.01.056.

[208] X. Fan, B. Chen, S. Wang, J.R. Zhao, H.J. Sun, An improved typical meteorological year based on outdoor climate comprehensive description method, Build. Environ. 206 (2021) 108366. https://doi.org/10.1016/j.buildenv.2021.108366.

[209] J. Bilbao, A. Miguel, J.A. Franco, A. Ayuso, Test reference year generation and evaluation methods in the continental Mediterranean area, J. Appl. Meteorol. 43 (2004) 390–400. https://doi.org/10.1175/1520-0450(2004)043<0390:TRYGAE>2.0.CO;2.

[210] G. Sorrentino, G. Scaccianoce, M. Morale, V. Franzitta, The importance of reliable climatic data in the energy evaluation, Energy. 48 (2012) 74–79. https://doi.org/10.1016/j.energy.2012.04.015.

[211] M.D. Fernández, J.C. López, E. Baeza, A. Céspedes, D.E. Meca, B. Bailey, Generation and evaluation of typical meteorological year datasets for greenhouse and external conditions on the Mediterranean coast, Int. J. Biometeorol. 59 (2015) 1067–1081. https://doi.org/10.1007/s00484-014-0920-7.

[212] A. Argiriou, S. Lykoudis, S. Kontoyiannidis, C.A. Balaras, D. Asimakopoulos, M. Petrakis, P. Kassomenos, Comparison of methodologies for TMY generation using 20 years data for Athens, Greece, Sol. Energy. 66 (1999) 33–45. https://doi.org/10.1016/S0038-092X(99)00012-2.

[213] H. Li, Y. Yang, K. Lv, J. Liu, L. Yang, Compare several methods of select typical meteorological year for building energy simulation in China, Energy. 209 (2020) 118465. https://doi.org/10.1016/j.energy.2020.118465.

[214] K. Skeiker, Comparison of methodologies for TMY generation using 10 years data for Damascus, Syria, Energy Convers. Manag. 48 (2007) 2090–2102. https://doi.org/10.1016/j.enconman.2006.12.014.

[215] S. Janjai, P. Deeyai, Comparison of methods for generating typical meteorological year using meteorological data from a tropical environment, Appl. Energy. 86 (2009) 528–537. https://doi.org/10.1016/j.apenergy.2008.08.008.

[216] H.D. Kambezidis, B.E. Psiloglou, D.G. Kaskaoutis, D. Karagiannis, K. Petrinoli, A. Gavriil, K. Kavadias, Generation of typical meteorological years for 33 locations in Greece: adaptation to the needs of various applications, Theor. Appl. Climatol. 141 (2020) 1313–1330. https://doi.org/10.1007/s00704-020-03264-7.

[217] W.K. Chow, S.K. Fong, Typical meteorological year for building energy simulation in hong kong, Archit. Sci. Rev. 40 (1997) 11–15. https://doi.org/10.1080/00038628.1997.9697372.

[218] G. Murano, D. Dirutigliano, V. Corrado, Improved procedure for the construction of a Typical Meteorological Year for assessing the energy need of a residential building, J. Build. Perform. Simul. 13 (2020) 139–151. https://doi.org/10.1080/19401493.2018.1479774.

[219] F. Bre, R.M. e Silva Machado, L.K. Lawrie, D.B. Crawley, R. Lamberts, Assessment of solar radiation data quality in typical meteorological years and its influence on the building performance simulation, Energy Build. 250 (2021) 111251. https://doi.org/10.1016/j.enbuild.2021.111251.

[220] J. Sun, Z. Li, F. Xiao, J. Xiao, Generation of typical meteorological year for integrated climate based daylight modeling and building energy simulation, Renew. Energy. 160 (2020) 721–729. https://doi.org/10.1016/j.renene.2020.07.024.

[221] S. Murphy, The construction of a modified Typical Meteorological Year for photovoltaic modeling in India, Renew. Energy. 111 (2017) 447–454. https://doi.org/10.1016/j.renene.2017.04.033.

[222] S.S. Chakraborty, R. Kumar, A.K. Haldkar, S. Ranjan, Mathematical method to find best suited PV technology for different climatic zones of India, Int. J. Energy Environ. Eng. 8 (2017) 153–166. https://doi.org/10.1007/s40095-016-0227-z.

[223] J. Polo, M. Alonso-Abella, N. Martín-Chivelet, J. Alonso-Montesinos, G. López, A.

Marzo, G. Nofuentes, N. Vela-Barrionuevo, Typical Meteorological Year methodologies applied to solar spectral irradiance for PV applications, Energy. 190 (2020). https://doi.org/10.1016/j.energy.2019.116453.

[224] W. Batayneh, A. Bataineh, I. Soliman, Investigation of solar tracking performance using isotropic and anisotropic models, Adv. Build. Energy Res. 15 (2021) 390–408. https://doi.org/10.1080/17512549.2019.1625810.

[225] O.S. Ohunakin, M.S. Adaramola, O.M. Oyewola, R.O. Fagbenle, D.S. Adelekan, J. Gill, F.I. Abam, Photovoltaic performance prediction in Northern Nigeria using generated typical meteorological year dataset, African J. Sci. Technol. Innov. Dev. 10 (2018) 579–591. https://doi.org/10.1080/20421338.2018.1511280.

[226] M. Ernst, J. Gooday, Methodology for generating high time resolution typical meteorological year data for accurate photovoltaic energy yield modelling, Sol. Energy. 189 (2019) 299–306. https://doi.org/10.1016/j.solener.2019.07.069.

[227] C. Li, Economic and performance evaluation of grid-connected residential solar photovoltaic systems in Northwest China, Energy Sources, Part A Recover. Util. Environ. Eff. 44 (2022) 5473–5489. https://doi.org/10.1080/15567036.2019.1668882.

[228] S.M. Kim, M. Oh, H.D. Park, Analysis and prioritization of the floating photovoltaic system potential for reservoirs in Korea, Appl. Sci. 9 (2019). https://doi.org/10.3390/app9030395.

[229] K.N. Patil, S.C. Kaushik, Study of climatic potential for natural ventilation in buildings for typical indian cities, Int. J. Vent. 13 (2015) 369–380. https://doi.org/10.1080/14733315.2015.11684061.

[230] N.A. Al-Azri, Y.H. Zurigat, N.Z. Al-Rawahi, Development of bioclimatic chart for passive building design, Int. J. Sustain. Energy. 32 (2013) 713–723. https://doi.org/10.1080/14786451.2013.813026.

[231] N.A. Al-Azri, Development of a typical meteorological year based on dry bulb temperature and dew point for passive cooling applications, Energy Sustain. Dev. 33 (2016) 61–74. https://doi.org/10.1016/j.esd.2016.05.001.

[232] A.T. Nguyen, S. Reiter, A climate analysis tool for passive heating and cooling strategies in hot humid climate based on Typical Meteorological Year data sets, Energy Build. 68 (2014) 756–763. https://doi.org/10.1016/j.enbuild.2012.08.050.

[233] S. Pusat, I. Ekmekci, A study on degree-day regions of Turkey, Energy Effic. 9 (2016) 525–532. https://doi.org/10.1007/s12053-015-9378-7.

[234] J. Sun, Z. Li, F. Xiao, Analysis of Typical Meteorological Year selection for energy simulation of building with daylight utilization, Procedia Eng. 205 (2017) 3080–3087. https://doi.org/10.1016/j.proeng.2017.10.303.

[235] J. Chai, P. Huang, Y. Sun, Investigations of climate change impacts on net-zero energy building lifecycle performance in typical Chinese climate regions, Energy. 185 (2019) 176–189. https://doi.org/10.1016/j.energy.2019.07.055.

[236] J. Wang, M. Wei, X. Ruan, Characterization of the acceptable daylight quality in typical residential buildings in Hong Kong, Build. Environ. 182 (2020) 107094. https://doi.org/10.1016/j.buildenv.2020.107094.

[237] H. Ye, Z. Wang, L. Wang, Effects of PCM on power consumption and temperature control performance of a thermal control system subject to periodic ambient conditions, Appl. Energy. 190 (2017) 213–221. https://doi.org/10.1016/j.apenergy.2016.12.123.

[238] Y.J.M.F.A.R.E. SCHAFER, Improved goodness-of-fit tests, (1971).

[239] R. Gupta, A.K. Yadav, S.K. Jha, P.K. Pathak, Long term estimation of global horizontal irradiance using machine learning algorithms, Optik (Stuttg). 283 (2023) 170873. https://doi.org/10.1016/j.ijleo.2023.170873.